

Aus dem Departement für Physik
Universität Freiburg (Schweiz)



Laser-pumped cesium magnetometers for the PSI-nEDM experiment

Inaugural-Dissertation

zur Erlangung der Würde eines
Doctor rerum naturalium
der Mathematisch-Naturwissenschaftlichen Fakultät
der Universität Freiburg in der Schweiz

vorgelegt von

Stephan Gröger

aus München (Deutschland)

Nummer der Dissertation: 1487

Universitätsdruckerei

2005

Von der Mathematisch-Naturwissenschaftlichen Fakultät der Universität Freiburg in der Schweiz
angenommen, auf Antrag der Herren

Prof. Dr. Dionys Baeriswyl, Universität Freiburg (Präsident der Jury)
Prof. Dr. Antoine Weis, Universität Freiburg (Referent)
Prof. Dr. Jean-Claude Dousse, Universität Freiburg (Koreferent)
Dr. Manfred Daum, Paul Scherrer Institut, Villigen (Koreferent)

Freiburg, 2. September 2005

Der Leiter der Dissertation



Prof. Dr. Antoine Weis

Der Dekan



Prof. Dr. Marco Celio

Abstract

This thesis work describes the development of a high resolution magnetic field sensor for a fundamental research project of an international collaboration with participation of the Fribourg Atomic Physics Group. The goal of the collaboration is an experiment searching for an electric dipole moment of the neutron (nEDM), d , which will be performed at Paul Scherrer Institute (PSI). The possible existence and mainly the size of the dipole moment is of great scientific interest concerning a better understanding of the fundamental interactions of elementary particles. If one is able to lower the sensitivity for a nEDM to the level of $\sigma(d) \sim 10^{-27} \text{e} \cdot \text{cm}$, the experimental result will give valuable information regarding “new physics” beyond the Standard Model. Such an improvement in resolution is the purpose of the PSI-nEDM experiment, which has to be performed under ultra-stable conditions. Hereby, a crucial requirement is the control of the fluctuations of a $1 \mu\text{T}$ magnetic field (about 1/50 of the earth magnetic field) on a level of better than 100fT which corresponds to a relative (in)stability of less than 10^{-7} .

The magnetic field stability requirement can directly be understood as a specification for the magnetic field sensors. In order to reach a sub-pT resolution we have developed a specific sensor system using the technique of optically-detected magnetic resonance (ODMR) in cesium vapor. Due to their unpaired valence electron the Cs atom is paramagnetic and has a magnetic moment on the order of one Bohr magneton. This magnetic moment interacts with an external magnetic field resulting in a Larmor precession around the field direction at a frequency proportional to the magnetic field. On the other hand, the orientation of the spin, i.e., of the total angular momentum of the atoms, determines the optical properties of the Cs vapor. The detection of the Cs spin precession is thus possible via their interaction with light.

The principles of that technique have been well known for about 50 years and magnetometers are commercially available for particular applications ranging from geology to archeology. Nevertheless, depending on the requirements and specific applications very specialized realizations are needed. In the present thesis work discharge lamps, which usually serve as light sources, were replaced by a frequency-stabilized diode-laser system. It could be shown that this leads to an intrinsic sensor resolution by up to a factor of three better than the one obtained with lamp-pumped devices. The active volume of the sensor, given by the size of the cell containing the Cs vapor, was about 180cm^3 . After optimizing all parameters a resolution of $14 \text{fT}/\sqrt{\text{Hz}}$ was obtained, and the magnetic field measurements can be performed with a bandwidth of about 1 kHz.

After characterizing and optimizing the sensor in a very controlled environment in Fribourg a multi-sensor system was built in order to measure magnetic field fluctuations at real experimental sites at PSI and at Institute Laue-Langevin (ILL) in Grenoble. A major step for the realization of such a measurement system was the development of a multi-channel frequency counter based on a commercial sound card, which fulfills – in contrast to commercial frequency counters at hand – the frequency resolution requirement.

In parallel to the research and development work for the PSI-nEDM experiment, alternative optical magnetic-field-detection methods were investigated. This work concludes with a newly developed technique using linearly rather than circularly polarized light, a magnetometry technique which is only feasible with laser excitation, and which appears to be very promising for future applications.

Zusammenfassung

Die vorliegende Arbeit beschreibt die Entwicklung eines Magnetfeldsensors mit hoher Auflösung für ein Grundlagenforschungsprojekt im Rahmen einer internationalen Kollaboration unter Beteiligung der Freiburger Atomphysikgruppe. Das Ziel des Projekts ist die Durchführung eines Experiments am Paul Scherrer Institut (PSI) zur Bestimmung des elektrischen Dipolmoments des Neutrons (nEDM: *neutron electric dipole moment*), d . Die mögliche Existenz und vor allem die Größe eines solchen Dipolmoments ist von großem wissenschaftlichen Interesse hinsichtlich eines besseren Verständnisses der grundlegenden Wechselwirkungen zwischen den Grundbausteinen der Materie. Allein die Senkung der gegenwärtigen nEDM-Messungsgenauigkeit um eine Größenordnung in den Bereich von $\sigma(d) \sim 10^{-27} e \cdot \text{cm}$ erlaubt mittels des Vergleichs mit theoretischen Voraussagen wertvolle Aussagen über „neue Physik“, die über das Standardmodell hinausgeht. Das Erreichen einer solchen Auflösung ist das erklärte Ziel der PSI-nEDM-Experiments. Das Experiment muss daher unter ultra-stabilen Bedingungen durchgeführt werden, wobei ein Punkt von außerordentlicher Bedeutung die Kontrolle eines $1\mu\text{T}$ starken Magnetfeldes (etwa 1/50 des Erdmagnetfeldes) auf einem Niveau von besser als 100fT darstellt. Das entspricht einer relativen Feld(in)stabilität von weniger als 10^{-7} .

Die Anforderungen, die an das Magnetfeld gestellt werden, lassen sich direkt auf die verwendeten Magnetfeldsensoren übertragen. Um eine Auflösung im sub-pT-Bereich zu erhalten, wurde daher ein speziell auf dieses Experiment abgestimmtes Sensorsystem entwickelt, das auf der optisch detektierten Magnetresonanz (ODMR) in Cäsiumdampf beruht. Die paramagnetischen Cäsiumatome verfügen aufgrund des ungepaarten Valenzelektrons über ein assoziiertes magnetisches Moment in der Größenordnung von einem Bohrmagneton, dessen Wechselwirkung mit einem Magnetfeld die Präzession der Atome in diesem Feld bewirkt. Dabei ist die gemessene Präzessionsfrequenz proportional zur Magnetfeldstärke. Gleichzeitig bestimmt auch der Spin, d.h. der Gesamtdrehimpuls, der Atome die optischen Eigenschaften des Cäsiumdampfes. Somit ist ein Nachweis der Spinpräzession von Cäsiumatomen über ihre Wechselwirkungseigenschaften mit Licht möglich.

Obwohl die grundlegenden Prinzipien dieser Technik seit etwa 50 Jahren bekannt sind und Sensoren für spezielle Anwendungen, z.B. in der Geologie und Archäologie, kommerziell erhältlich sind, ergeben sich je nach Anwendungsanforderungen und Spezifikationen speziell angepasste Realisierungen. So wurde im Rahmen dieser Arbeit anstelle der üblicherweise verwendeten Gasentladungslampen als Lichtquelle ein frequenzstabilisiertes Diodenlasersystem verwendet. Wie gezeigt werden konnte, kann allein dadurch eine Verbesserung der intrinsischen Magnetfeldauflösung der Sensoren um das nahezu Dreifache erreicht werden. Mit optimierten Parametern wurde eine Magnetometerauflösung von bis zu $14\text{fT}/\sqrt{\text{Hz}}$ ermittelt. Das aktive Volumen des Sensors, d.h. die Größe der Glaszelle, die die Cäsiumatome enthält, war dabei etwa 180cm^3 . Die Magnetfeldmessungen können mit einer maximalen Messbandbreite von etwa 1 kHz durchgeführt werden.

Nach der erfolgreichen Charakterisierung und Optimierung des Sensors unter gut kontrollierten Bedingungen in Freiburg wurde ein Multisensor-System aufgebaut, um an „realen“ Schauplätzen für ein nEDM-Experiment am PSI und am Institut Laue-Langevin (ILL) in Grenoble Magnetfeldfluktuationen zu messen. Ein wesentlicher Bestandteil dieses Systems war die Entwicklung eines hochauflösenden Mehrkanal-Frequenzzählers auf Basis einer kommerziell erhältlichen Soundkarte, da die für uns verfügbaren kommerziellen Frequenzzählersysteme eine nur ungenügende Auflösung boten.

Parallel zur Entwicklungsarbeit für das PSI-nEDM-Experiment wurden alternative optische Magnetometertechniken untersucht. Am Ende der vorliegenden Arbeit wird eine neuartige Methode mit linear statt zirkular polarisiertem Licht vorgestellt, die sehr vielversprechend für zukünftige Anwendungen erscheint.

Contents

Preface	1
1 Introduction	3
1.1 Optically detected magnetic resonance in cesium	3
1.1.1 The cesium hyperfine and Zeeman structure	3
1.1.2 Optical pumping	4
1.1.3 Optically detected magnetic resonance	6
1.2 An experiment searching for an electric dipole moment of the neutron	9
1.2.1 The neutron electric dipole moment	9
1.2.2 The basic principle of EDM measurements	10
1.2.3 The Ramsey method of separated oscillatory fields	11
1.2.4 Statistical measurement uncertainty	16
1.2.5 Some words about the PSI-nEDM experiment	17
2 Design and performance of laser-pumped Cs magnetometers for the planned UCN EDM experiment at PSI	23
2.1 Introduction	24
2.2 The magnetometer setup	24
2.3 Performance of the magnetometer	25
2.3.1 Intrinsic magnetometric sensitivity	25
2.3.2 Application: Field fluctuations in a magnetic shield	26
2.4 Summary and conclusion	26
3 A high-sensitivity laser-pumped M_x magnetometer	29
3.1 Introduction	30
3.2 The optically-pumped M_x magnetometer	30
3.3 Magnetometer hardware	32
3.3.1 Resonance linewidth	33
3.3.2 Magnetometer mode	34
3.4 Performance of the magnetometer	34
3.4.1 Magnetometric sensitivity	34
3.4.2 Magnetometer optimization and response bandwidth	36
3.4.3 Application: Field fluctuations in a magnetic shield	37
3.4.4 Frequency noise due to light power fluctuations	38
3.5 Summary and conclusion	39
4 Comparison of discharge lamp and laser pumped cesium magnetometers	41
4.1 Introduction	42
4.2 Optically pumped magnetometers	42
4.2.1 General principle	42
4.2.2 Effects of hyperfine structure	43

4.2.3	Practical realization	44
4.2.4	Features of the LsOPM and the LpOPM	45
4.2.5	Modes of operation	46
4.3	Performance	47
4.3.1	Magnetometric sensitivity: Basics and fundamental limit	47
4.3.2	Limitations by light power fluctuations	48
4.3.3	Limitations by magnetic field fluctuations	48
4.3.4	Measurement of the intrinsic sensitivity	49
4.3.5	Discussion	50
4.4	Applications	51
4.4.1	Direct comparison of LsOPM and LpOPM	51
4.4.2	Systematic effects	52
4.4.3	Active field stabilization	52
4.5	Further applications	53
5	A sound card based multi-channel frequency measurement system	55
5.1	Introduction	56
5.2	The system	56
5.3	Performance	57
6	Laser-pumped optically detected magnetic resonance using linearly polarized light	61
6.1	Introduction	62
6.2	Theory	63
6.3	Experiment	64
6.4	Conclusion	65
	Outlook	67
	Danksagung	69
	Curriculum vitae	71

Preface

The research carried out during this thesis was done within the framework of the PSI-nEDM experiment. It was focused on developing a magnetometry system that fulfills the specifications and requirements for that particular application. Chapter 1 consists of a general introduction to optical pumping and optically detected magnetic resonance in Cs, and the main features of the nEDM experiment that are shortly described with a particular emphasis on the magnetometry issue. The introduction is followed by five chapters which consist of articles written during this thesis. Thus, each chapter can be understood as an independent text with an introduction, the main text consisting of the experimental setup, results, discussion, and the references of the article.

The articles included in this thesis are:

Chapter 2

S. Groeger, G. Bison, and A. Weis. *Design and performance of laser-pumped Cs magnetometers for the planned UCN EDM experiment at PSI*. J. Res. Natl. Inst. Stand. Technol. **110**(3), 179–183 (2005).

Chapter 3

S. Groeger, G. Bison, J.-L. Schenker, R. Wynands, and A. Weis. *A high-sensitivity laser-pumped M_x magnetometer*. (Submitted to Eur. Phys. J. D).

Chapter 4

S. Groeger, A. S. Pazgalev, and A. Weis. *Comparison of discharge lamp and laser pumped cesium magnetometers*. Appl. Phys. B **80**(6), 645–654 (2005).

Chapter 5

S. Groeger, G. Bison, P. E. Knowles, and A. Weis. *A sound card based multi-channel frequency measurement system*. (Submitted to Eur. Phys. J. AP).

Chapter 6

S. Groeger, G. Bison, A. S. Pazgalev, M. Rebetez, and A. Weis. *Laser-pumped optically detected magnetic resonance using linearly polarized light*. (To be submitted).

Chapter 2 gives an overview of the magnetometer performance, while in chapter 3 the detailed characterization and analysis of the magnetometric resolution and systematic effects is presented. In particular the treatment of the various performance-decreasing noise sources as introduced in this chapter allows a better sensor characterization compared to former literature. After the successful development of the laser-pumped Cs sensors it was of great interest to compare this technique to state-of-the-art lamp-pumped magnetometers. That comparison, as reported in chapter 4, was not been done before in such detail and it provided the scientific basis for the decision about which technique to chose for the nEDM experiment. The measurement system has to provide a sufficient resolution that complies with the high intrinsic resolution of the sensor. Chapter 5 reports about the realization and characterization of a frequency counting system that reaches the theoretical limit of resolution which is sufficient for the nEDM experiment. The topic of chapter 6 is a new method for detecting magnetic resonance in a medium pumped with linearly rather than circularly polarized light. This kind of detection was performed for the first time in our lab and it will possibly be an alternative to the used technique.

Chapter 1

Introduction

The magnetometry issues described in this work were developed in the framework of a planned experiment looking for a permanent electric dipole moment of the neutron (nEDM). This chapter first describes the basic concepts of optically detected magnetic resonance (ODMR) spectroscopy in cesium on which the used magnetometry method is based. In a second part a general overview over the scientific importance of the nEDM search is given and the experimental technique of the nEDM measurement is presented.

1.1 Optically detected magnetic resonance in cesium

The interaction of a Cs atom with an external magnetic field is governed by the magnetic moment of its unpaired electron, which is on the order of one Bohr magneton, μ_B , aligned with the electron spin. In addition, the optical properties, such as the absorption coefficient for resonant polarized light, depend strongly on the atomic spin orientation. Therefore, the spin-mediated connection between optical and magnetic properties allows the detection of magnetic interactions via the change of light-dependent properties [1, 2, 3]. Furthermore, in an atomic ensemble it is the coherent interaction of many atoms with both the light field and the magnetic field which leads to a significant amplification of the detectable effects arising from the individual interactions and finally yields a measurable effect. In the following we recall the main principles of ODMR which form the basis for all further discussions in this work.

1.1.1 The cesium hyperfine and Zeeman structure

Cesium has a hydrogen-like electron configuration, $[\text{Xe}]6s^1$, with an total electronic angular momentum $J = 1/2$ ¹. The only stable isotope, ^{133}Cs (used in all our applications), has a nuclear spin $I = 7/2$. The hyperfine interaction splits the $6S_{1/2}$ ground state into the two hyperfine levels $F = |I \pm J| = 3, 4$ as shown in Fig. 1.1a. The energy difference between the two hyperfine states corresponds to a microwave transition of (exactly) 9.192 631 770 GHz². Via the D_1 transition in the near-infrared (894.6 nm) the atom can be excited to the lowest excited state, $6P_{1/2}$, which is split into the hyperfine levels $f = 3, 4$ separated by approximately 1.2 GHz. The Doppler-width of the absorption spectrum (approximately 300 MHz at room temperature) is much smaller than the hyperfine splitting so that the hyperfine structure in both the ground and the excited states can be resolved by direct absorption spectroscopy.

Each hyperfine level F consists of $2F + 1$ degenerate magnetic sublevels, $|F, M_F\rangle$. In an external magnetic field, \vec{B}_0 , the energies of the Zeeman levels are perturbed due to the magnetic interaction described by the Hamiltonian $H = -\vec{\mu} \cdot \vec{B}_0$, where $\vec{\mu}$ is the F -dependent magnetic moment of the cesium atom. The magnetic field induced shift $\Delta E(M_F)$ of each Zeeman level M_F is described by the

¹Note that the angular momentum is defined in units of \hbar and can be written as $\vec{J}\hbar$, where \vec{J} is dimensionless. The quantity J is the maximum possible component of \vec{J} in any direction.

²Here and in the following we usually use the spectroscopist's convention of expressing energy differences by the corresponding transition frequency or wavelength (1 GHz corresponds to approximately $4 \mu\text{eV}$). Note also that at the time of writing (2005), the second is defined by the value of the Cs hyperfine splitting.

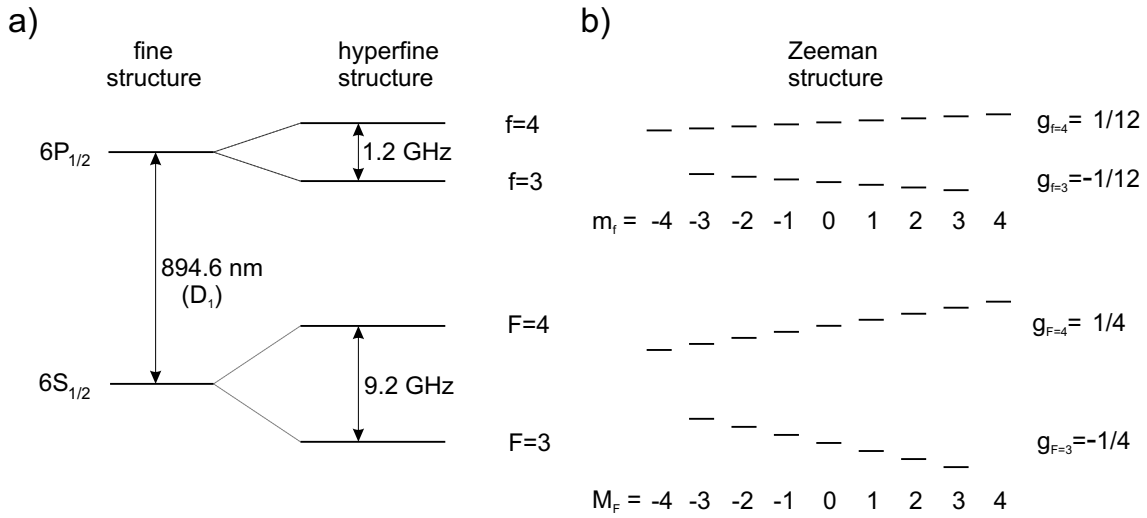


FIGURE 1.1: Energy scheme of ^{133}Cs . a) D_1 transition with hyperfine structure (not to scale). The transition $6S_{1/2}, F=4 \rightarrow 6P_{1/2}, f=3$ is relevant for the magnetometry applications. b) Linear Zeeman effect in a small magnetic field (not to scale). Due to the different signs of the g-factors $g_{F=3}$ and $g_{F=4}$ the energy shifts also have opposite sign. The gyromagnetic ratio in the ground state is about $\pm 3.50 \text{ Hz/nT}$ and in the excited state $\pm 1.16 \text{ Hz/nT}$, respectively.

well-known Breit-Rabi formula [4]. For small magnetic fields (up to a few μT) it is linear in the field magnitude $B_0 = |\vec{B}_0|$ and linear in M_F :

$$\Delta E(M_F) = g_F \mu_B B_0 M_F, \quad (1.1)$$

where μ_B is the Bohr magneton and g_F is the Landé g-factor for the hyperfine level F (Fig. 1.1b). The transition frequency, ω_L (Larmor frequency), between adjacent sublevels M_F and $M_F + 1$ is

$$\omega_L = \frac{1}{\hbar} [\Delta E(M_F + 1) - \Delta E(M_F)] = \gamma B_0, \quad (1.2)$$

with the gyromagnetic ratio $\gamma = g_F \mu_B / \hbar$. For the cesium ground state $\gamma \approx 2\pi \times 3.5 \text{ Hz/nT}$, thus the splitting in magnetic fields of a few μT is on the order of several kHz.

1.1.2 Optical pumping

At room temperature the energy difference between the two ground state hyperfine levels in Cs ($\approx 10 \text{ GHz}$) is much smaller than the thermal energy of the atoms ($\approx 10^4 \text{ GHz}$) so that all 16 sublevels are equally populated. In order to drive a magnetic resonance transition between levels in a given hyperfine state, a net polarization or magnetization is needed, i.e., a population imbalance must be created within that hyperfine multiplet. For many atoms optical pumping is a convenient method to create such an imbalance, a technique which is based on the pioneering work of Kastler and Brossel in 1949 [5]. In most realizations, Cs discharge lamps serve as pumping sources. Their emission spectrum is very broad covering not only D_1 transition lines, and a spectral filter for isolating the emission from the D_1 transition is required in order to obtain efficient optical pumping [6]. In contrast, due to the very narrow spectral width of its emission spectrum (usually a few MHz) combined with a much higher light intensity a tunable laser can be used to excite a single hyperfine transition, e.g., $6S_{1/2}, F \rightarrow 6P_{1/2}, f$.

Consider a light beam, right circularly polarized (σ^+) and resonant with the $F=4 \rightarrow f=3$ hyperfine transition of the D_1 line, irradiating a sample of Cs atoms contained in a suitable storage volume such as a glass cell.³ Each photon “carries” an angular momentum quantum of $+1\hbar$. When an atom absorbs

³At room temperature the vapor pressure of Cs yields an atomic density of a few times $10^{10}/\text{cm}^3$ [7].

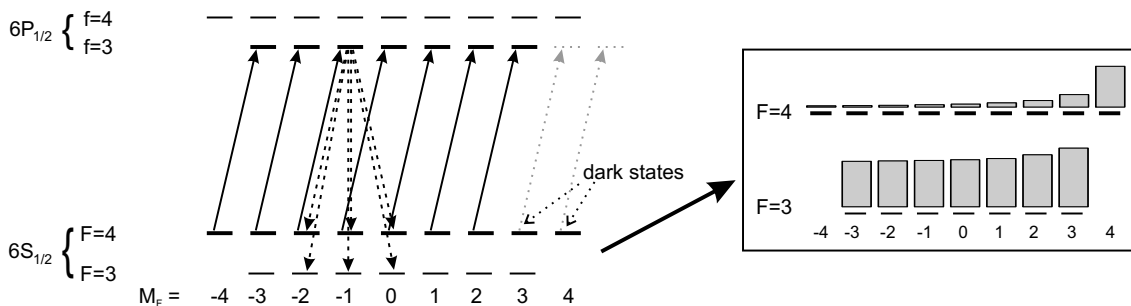


FIGURE 1.2: Transitions induced by right circularly polarized light are shown by the solid lines. The decay channels of the level $6P_{1/2}$ $|f = 3, m = -1\rangle$ are indicated by the dashed lines. The inset shows the steady-state population distribution for the two ground-state hyperfine multiplets for a normalized pumping rate $\gamma_p/\gamma = 100$.

a photon, the angular momentum of the atom increases by $+1\hbar$ (angular momentum conservation). Thus σ^+ light drives transitions $|4, M\rangle \rightarrow |3, M+1\rangle$ as shown in Fig. 1.2. If the light intensity is low enough such that stimulated emission processes can be neglected, the excited atom spontaneously decays to a ground state level M' following the selection rules $\Delta F = 0, \pm 1$ and $\Delta M = 0, \pm 1$ (excluding $\Delta F = 0, |f, m = 0\rangle \rightarrow |F, M = 0\rangle$). Due to angular momentum conservation the emitted photon is either circularly polarized ($\Delta M = \pm 1$) or linearly polarized ($\Delta M = 0$). The lifetime of the excited state $6P_{1/2}$, τ_e , (the inverse of the decay rate Γ) is about 30 ns. In Fig. 1.2 the possible decay channels for the state $6P_{1/2}$ $|f = 3, m = -1\rangle$ are shown. The emission occurs isotropically (i.e., no preferred spatial direction) so the effect of the absorption and emission process is to scatter the incoming light and decreases the transmitted light intensity.

The branching ratio between the decay channels is given by the squares of the matrix elements of the dipole operator, i.e., by the corresponding Clebsch-Gordan coefficients. Depending on the transition probabilities for the excitation from ground state levels and the decay from excited state levels, optical pumping can create significant population imbalances. One can distinguish two mechanisms, the *repopulation pumping* and the *depopulation pumping* [6]. In the case of depopulation pumping the pumping light excites the atoms from different ground state sublevels at different rates, because the transition probabilities, or in other words the absorption cross sections for the pumping light, vary for the different ground state levels. Repopulation pumping occurs due to the different probabilities of the decay channels of an excited level substate. Both mechanisms are present in the case of applying circularly polarized light to the Cs atoms.

Concerning the *effect* of the optical pumping one distinguishes Zeeman pumping, which creates a population imbalance within each of the ground state multiplets, and hyperfine pumping, which creates an imbalance between the total populations of the two hyperfine levels. The former is used in magnetometry, while the latter is applied in the case of atomic clocks. Although hyperfine pumping can significantly decrease the population in the $F = 4$ state we will not further address this kind of pumping here but just mention that if hyperfine pumping is to be avoided, then, for example, a second light field resonant with the $F = 3$ ground state can be used to effectively pump the atoms back to the $F = 4$ ground state. This technique is known as repumping.

In Zeeman pumping, there is a certain probability for the atom to decay into a Zeeman state with $|F, M'\rangle = |F, M+1\rangle$ or $|F, M'\rangle = |F, M+2\rangle$ after one absorption-emission pumping cycle. Thus, applying σ^+ light on the $F = 4 \rightarrow f = 3$ transition will transfer the $F = 4$ Zeeman level population towards the $M = 3, 4$ states which cannot absorb σ^+ photons, and are therefore called dark states. If all atoms are pumped into the dark states, the Cs sample is completely polarized, and becomes transparent for σ^+ light. The optical properties of the atomic sample thus strongly depend on the population distribution and the polarization. In general, the hyperfine multiplet polarization, P_0 , with respect to a given quantization

axis⁴ is defined as

$$P_0 = \langle F_z \rangle = \frac{1}{F} \sum_{M_F} M_F p(M_F), \quad (1.3)$$

where $p(M_F)$ is the population of the Zeeman level M_F .

Due to relaxation processes, such as depolarizing binary collisions between two atoms (spin-exchange collisions) or atom-wall collisions, the atomic spins are redistributed towards the thermal equilibrium population and the balance of population creating and population destroying processes leads to a steady-state polarization $P_0 < 1$. Neglecting the relaxation rate initiated by spin-exchange collisions, the rate of atom-wall collisions can be approximated by the mean free path between two wall collisions, λ_w , and the mean velocity of the atoms, \bar{v} . Assuming a spherical cell with 70 mm diameter and using $\lambda_w = 4V/S$, where V and S are the cell volume and surface, respectively, one obtains a collision rate of $r_c = 4600 \text{ s}^{-1}$, which corresponds to a spin-relaxation time of about 0.2 ms. If atom-wall collisions are considered to be totally depolarizing, the polarization relaxation rate, γ , is given by $\gamma = r_c$, demanding a very high pumping rate. However, the probability of spin depolarization processes due to wall collisions is strongly reduced by a thin layer of paraffin or silane applied to the inner cell walls [8]. The coating can significantly lengthen the spin-relaxation time up to a second [9]. All cells used in the experiments described in this work had walls coated with paraffin and were purchased from MAGTECH Ltd. (St. Petersburg, Russia).

The steady-state polarization is determined by two parameters: i) the pumping rate, γ_p , which is itself a function of various parameters such as the light spectrum, its intensity, its polarization, its beam profile, its propagation direction, the lineshape of the absorption spectrum, and the atomic density (the latter two depending on the sample temperature); and ii) the relaxation rate, γ , which depends on the temperature of the atomic density and on cell properties such as geometry and wall coating. In the case $\gamma_p \ll \Gamma$ (recall that Γ is the inverse lifetime of the excited state) the rate of stimulated emission processes is negligible and the effect of optical pumping can be calculated by solving rate equations for the 16 ground state populations and the populations of the excited state levels [10]. In Fig. 1.2 the inset shows the calculated steady-state (equilibrium) population distribution obtained for a normalized pumping rate $\gamma_p/\gamma = 100$. The light direction was set at an angle of 45° with respect to the quantization axis. In this particular case the total population remaining in the $F = 4$ ground state is only 18%, and following Eq. 1.3, the obtained polarization in the level is nearly 70%. Note that as a side effect of the optical pumping in the $F = 4$ level there is a polarization of about 7% in the $F = 3$ level.

1.1.3 Optically detected magnetic resonance

In the previous section we saw that an atomic ensemble can be spin polarized by the absorption of circularly polarized light. After a sufficient number of pumping cycles the sample reaches a constant maximum in the transmitted light intensity indicating a maximized equilibrium polarization P_0 . If we assume a non-degenerate Zeeman structure due to the presence of a weak magnetic field \vec{B}_0 , magnetic transitions between neighboring Zeeman levels can be driven by the absorption of photons from an additionally applied resonant radio-frequency (r.f.) field. From Eq. 1.2 we see that the energy of the r.f. quanta has to be $\hbar\omega_L$. If the transitions occur in such a way that the sample polarization is lowered, meaning that the spins are redistributed towards their thermal equilibrium, the absorption coefficient of the ensemble will increase and the transmitted light intensity will decrease. The Zeeman splitting can be determined by tuning the energy of the applied r.f. quanta so that a maximum change in the transmitted light intensity is observed.

The choice of the light propagation direction \vec{k} with respect to the magnetic field leads to different technical realizations. To discuss different schemes, we treat ODMR in a classical picture. The sample can be described as a macroscopic object with a polarization $\vec{P} = \langle \vec{F} \rangle$, where \vec{F} is the atomic spin, and a magnetic moment $\vec{M} = \langle \vec{\mu} \rangle$, with $\vec{\mu}$ the magnetic moment associated to \vec{F} . According to the Ehrenfest's

⁴In magnetic resonance experiments the direction of the static magnetic field \vec{B}_0 is quite often a convenient choice for the quantization axis, therefore the choice of the index of P_0 .

theorem the expectation values of quantum mechanical operators obey classical equations of motion. The relation $\vec{\mu} = \gamma\vec{F}$, where γ is the gyromagnetic ratio, translates to $\vec{M} = \langle\vec{\mu}\rangle = \gamma\langle\vec{F}\rangle = \gamma\vec{P}$.

The polarization precesses with the Larmor frequency ω_L in an applied magnetic field \vec{B}_0 (which defines the z -axis) due to the torque $\vec{M} \times \vec{B}_0$. We thus obtain for the ensemble polarization

$$\frac{d\vec{P}}{dt} = \vec{M} \times \vec{B}_0 = \vec{P} \times \vec{\omega}_L, \quad (1.4)$$

where we have used $\vec{\omega}_L = \gamma\vec{B}_0$. If the polarization is tilted by an angle ϑ with respect to \vec{B}_0 , the vector \vec{P} will rotate around \vec{B}_0 on a cone with a half opening angle ϑ . The polarization \vec{P} has a static longitudinal component, \vec{P}_0 , parallel to \vec{B}_0 and a rotating transverse component, \vec{P}_t , perpendicular to \vec{B}_0 . If, after the polarization has built up, the ensemble is allowed to evolve freely without optical pumping, the polarization will decay to its equilibrium value $P = 0$. The relaxation rates for the longitudinal and the transverse components are called T_1 and T_2 , respectively, and obey $T_2 \leq T_1$ ⁵. Furthermore, if the Larmor precession is much faster than the relaxation and pumping rates, individual spins will be rapidly distributed over the whole precession cone and thus optical pumping will only establish a static steady-state polarization P_0 along \vec{B}_0 .

In order to detect the Larmor precession, an additional small magnetic field $\vec{B}_1(t)$, $|\vec{B}_1| \ll |\vec{B}_0|$, co-rotating with the spins in the xy -plane at frequency ω is applied. In a frame co-rotating with \vec{B}_1 , defined by the coordinates $(x', y', z' = z)$ with \vec{B}_1 pointing along x' , the spin precession occurs at the frequency $\delta\omega = \omega_L - \omega$ ⁶. The evolution of the polarization in the rotating frame, neglecting relaxation, can be written as

$$\left(\frac{d\vec{P}}{dt}\right)_{rot} = \left(\frac{d\vec{P}}{dt}\right)_{lab} - \vec{\omega} \times \vec{P} = \vec{M} \times \left(\vec{B} + \frac{\vec{\omega}}{\gamma}\right), \quad (1.5)$$

where $\left(\frac{d\vec{P}}{dt}\right)_{lab}$ is given by Eq. 1.4, and \vec{B} is the total magnetic field including static and rotating components. Equation 1.5 yields, after adding the relaxation rates Γ_1, Γ_2 ($= 1/T_1, 1/T_2$) for the transverse and longitudinal components, the Bloch equations for the magnetization components $P_{x'}$, $P_{y'}$, and $P_{z'}$ in the rotating frame:

$$\frac{dP_{x'}}{dt} = P_{y'}\delta\omega - \Gamma_2 P_{x'}, \quad (1.6)$$

$$\frac{dP_{y'}}{dt} = -P_{x'}\delta\omega + P_{z'}\Omega_R - \Gamma_2 P_{y'}, \quad (1.7)$$

$$\frac{dP_{z'}}{dt} = -P_{y'}\Omega_R - \Gamma_1(P_{z'} - P_0). \quad (1.8)$$

Here we used $\delta\omega = \omega - \omega_L$, $\omega_L = \gamma B_0$, and the Rabi frequency $\Omega_R = \gamma B_1$. If the relaxation rates are set to zero, one can easily verify that in the rotating frame the solutions of this set of differential equations yields – on resonance (i.e., $\delta\omega = 0$) and with the initial condition $\vec{P}(t=0) = (0, 0, P_0)$ – a rotation of the polarization around \vec{B}_1 with the frequency Ω_R :

$$P_{x'}(t) = 0, \quad (1.9)$$

$$P_{y'}(t) = P_0 \sin \Omega_R t, \quad (1.10)$$

$$P_{z'}(t) = P_0 \cos \Omega_R t. \quad (1.11)$$

⁵Due to the transverse relaxation the individual spin directions will be distributed over the whole cone that the spins describe during their precession. In the case of an isotropical distribution over the cone $P_t = 0$, whereas $P_0 > 0$ is still possible.

⁶Technically it is often more convenient to apply a linearly oscillating field perpendicular to B_0 . It can be expressed as a superposition of two rotating fields with opposite sense of rotation. In the rotating frame the counter-rotating field turns at 2ω and has only very little effect on the spins. It is therefore neglected, an approximation known as rotating wave approximation (r.w.a.). The effect of the neglected component is a small shift of the resonance frequency (Bloch–Siegert shift) which is on the order of $B_1^2/16B_0^2$ [11].

Thus, in the laboratory frame the tip of the polarization vector describes a sphere with a fast rotation (at ω_L) around the z -axis while it slowly nutates (at Ω_R) between $P_z = +P_0$ and $P_z = -P_0$.

If we include the relaxation we obtain a stationary solution in the rotating frame. This can be seen by setting the left-hand sides of Eqs. 1.6, 1.7, and 1.8 to zero and solving the remaining set of linear equations for the three components of \vec{P} . One obtains the steady-state polarization components in the rotating frame

$$P_{x'} = P_0 \frac{\Omega_R \delta\omega}{\delta\omega^2 + \Gamma_2^2(1+S)}, \quad (1.12)$$

$$P_{y'} = P_0 \frac{\Omega_R \Gamma_2}{\delta\omega^2 + \Gamma_2^2(1+S)}, \quad (1.13)$$

$$P_{z'} = P_0 \frac{\delta\omega^2 + \gamma_2^2}{\delta\omega^2 + \Gamma_2^2(1+S)}, \quad (1.14)$$

with the saturation parameter $S = \frac{\Omega_R^2}{\Gamma_1 \Gamma_2}$. We can easily verify that for the resonance condition $\delta\omega = 0$ we get $P_{x'} = 0$ and the steady-state magnetization is in the $y'z'$ -plane at an angle $\vartheta = \arctan(\Omega_R/\Gamma_2)$ with respect to the z' -axis. For $S = 1$, i.e., $\Omega_R = \sqrt{\Gamma_1 \Gamma_2}$, the component $P_{y'}$ reaches maximum. With $\Gamma_1 = \Gamma_2$ we obtain $P_{y'} = P_{z'}$ and $\vartheta = 45^\circ$.

Equations 1.12, 1.13, and 1.14 are valid for any direction of the pump light with respect to \vec{B}_0 . Going back to the laboratory frame the polarization, and thus the magnetization \vec{M} , will precess around the $z(=z')$ -axis. We distinguish between three major cases:

1. The M_z geometry: if the light direction \vec{k} is along the z -axis, there is no transverse component of \vec{P} and the polarization P_0 is largest. On resonance the polarization (in rotating frame) is rotated by an angle ϑ with respect to the z' -axis (cf. Eqs. 1.13 and 1.14) so that optical pumping can occur, resulting in a lower transmission of the pumping light. Note that there is only a static signal and the Larmor frequency can be obtained by determining the transmission as a function of the frequency ω of B_1 .
2. The M_x or 45° geometry: if the pumping direction is at an angle of 45° with respect to the z -axis, the resulting longitudinal polarization P_0 is only $1/\sqrt{2}$ of the magnetization obtained in the M_z magnetometer. Near resonance the polarization is tilted by the angle ϑ . In the laboratory frame the polarization will rotate with ω and therefore periodically change its projection on \vec{k} . This leads to a modulated transmission of the pumping light so that ω can be measured directly. The amplitude of the polarization projected on \vec{k} , and therefore the transmission modulation, is maximum for $\delta\omega = 0$, as can be easily verified using Eqs. 1.12, 1.13, and 1.14. Thus the transmission modulation is a direct measure of the Larmor frequency. Note that on resonance $P_{x'} = 0$ and thus the magnetization is perpendicular to B_1 leading to a phase shift of $\pi/2$ between the applied r.f. field and the transmission modulation.
3. The light propagation direction is perpendicular to \vec{B}_0 . According to our preliminary assumptions $P_0 = 0$, so in this case no magnetization is produced. Nevertheless, if the magnetic field is very small, i.e., if ω_L is on the order of the pumping rate, there is also a possibility of finding a resonance signal in this geometry [12].

Considering the different effects described above, ODMR can be modeled by a three-step process [13] which consists of preparing a spin state by optical pumping, free evolution of the spin in the magnetic fields, and probing the final spin state. This is an additional way to understand the interaction of each single atom. We assume that the cell dimensions are larger than the transverse extension of the light beam which pumps and probes the atoms in the direction \vec{k} . In the first step the atom enters the light beam where we consider the light intensity to be high enough so that the atom is optically pumped into a dark state. After having left the beam the atom freely precesses at the Larmor frequency for a time T ,

sampling the magnetic field as the atom traverses the cell. The phase, $\omega_L T$, accumulated by the atom during this time (step two) carries all information about the magnetic field. The longer the precession time the higher the accuracy in the magnetic field determination since more information is collected about the field. Here we see again the importance of an anti-relaxation coating of the cell walls, which avoids dephasing cell-wall collisions during the time T during which the atom has to maintain its phase information for a good field measurement. The third step occurs after the time T when the atom reenters the light beam and its interaction with the optical field constitutes the probe process. Depending on the spin direction with respect to \vec{k} the absorption will change, indicating the desired information. After probing, the atom is again in a dark state, so the third step is again the first step of a new cycle. This three-step cycle happens for all atoms continuously, but in order to get for example an oscillating signal in the M_x configuration many atoms have to precess coherently. Therefore the r.f. field is needed to synchronize the atomic precession.

1.2 An experiment searching for an electric dipole moment of the neutron

The three discrete symmetry operations P (mirror symmetry, parity), C (matter-antimatter exchange symmetry), and T (time reversal symmetry) play an important role in the description of elementary particle interactions. The observation of parity violation had a great impact in the formulation of the present Standard Model of electroweak interactions. Experiments investigating the weak decay of ^{60}Co nuclei, pions, and muons [14, 15, 16] were first manifestations of P-violating, T-conserving processes in weak interactions. Later on, a violation of the combined symmetry CP was observed, first in the decay of neutral kaons [17], and more recently also in the decay of neutral B-mesons [18]. Assuming that the physical processes are invariant under the combined symmetry CPT, a property of quantum field theories with local Lorentz invariance [19], the observation of CP violation consequently implies T violation. Therefore it seems natural to seek systems that directly violate T symmetry⁷. As shown in the following the existence of a permanent electric dipole moment in elementary particles would directly demonstrate T violation. Although we restrict the discussion mainly to the neutron it is valid also for other elementary particles (e.g., the electron).

1.2.1 The neutron electric dipole moment

A quantum mechanical system or particle such as the neutron is characterized, among others, by its angular momentum \vec{J} . As a consequence of the Wigner–Eckart theorem, the observables, i.e., the matrix elements of any vector property, \vec{V} , of the system must be proportional to the matrix elements of \vec{J} . Thus, \vec{V} has to be (anti)parallel to \vec{J} , and in the case of the neutron, \vec{J} is just the spin, \vec{S} . The magnetic dipole moment $\vec{\mu}$ is a vector property and can be expressed as

$$\vec{\mu} = \mu \frac{\vec{S}}{S}, \quad (1.15)$$

with the neutron magnetic moment $\mu/h = -14.58 \text{ Hz}/\mu\text{T}$.

A neutron electric dipole moment (nEDM) \vec{d} can be understood as a finite displacement of the center of mass with respect to the center of charge:

$$\vec{d} = \int \vec{r} \cdot \rho(\vec{r}) d\vec{r}, \quad (1.16)$$

where \vec{r} is the position vector and $\rho(\vec{r})$ the charge density. From Eq. 1.16 we clearly see that \vec{d} is a polar vector. However, analogous to Eq. 1.15 the EDM has to be parallel to the angular momentum, thus

$$\vec{d} = d \frac{\vec{S}}{S}. \quad (1.17)$$

⁷A direct observation of T violation in the neutral-kaon system was reported in [20].

It is clear that therefore \vec{d} has to be parallel or antiparallel to $\vec{\mu}$, depending on the relative signs of μ and d . This can easily be understood from a more instructive argument. The existence of a finite EDM \vec{d} with $\vec{d} \nparallel \vec{S}$ would introduce an additional degree of freedom in the description of the particle. This would lead to an additional quantum number whose existence is forbidden by the Pauli principle.

Applying T or P to both sides of Eq. 1.17 yields, for the left-hand side,

$$P(\vec{d}) = -\vec{d} \quad (1.18)$$

$$T(\vec{d}) = \vec{d}, \quad (1.19)$$

and for the right-hand side (leaving out the scalar d/S)

$$P(\vec{S}) = \vec{S} \quad (1.20)$$

$$T(\vec{S}) = -\vec{S}. \quad (1.21)$$

Applying either P or T thus changes the properties of the neutron by changing the relative orientation of \vec{d} and \vec{S} with respect to each other. This fact can also be expressed by considering the scalar product $\xi = \vec{S} \cdot \vec{d}$ (or similar $\xi = \vec{\mu} \cdot \vec{d}$) which forms a T and P pseudo-scalar: $P(\xi) = -\xi$, $T(\xi) = -\xi$. This factor ξ is only invariant under P and T if d vanishes, so the existence of a finite EDM is a manifestation of the violation of both mirror and time reversal symmetry.

In the 1950's a serious search for the nEDM began, yielding an upper limit of $d < 4 \times 10^{-20} \text{ e} \cdot \text{cm}$ (90% C.L.) for the neutron [21]. In the following years the sensitivity was consequently increased leading to the current upper limit of $d < 6.3 \times 10^{-26} \text{ e} \cdot \text{cm}$ (90% C.L.) [22]. Note that if the neutron was scaled up to the size of the earth, this value would correspond to only a few μm displacement between the center of mass and the center of charge. However, the Standard Model predicts d to be on the order of $10^{-33} \text{ e} \cdot \text{cm}$ [23] which is currently far below the reach of experiments. On the other hand, extensions to the Standard Model, which are for example necessary to explain the baryon asymmetry of the universe [24], predict a nEDM which is just one or two orders of magnitude below the current experimental limit. An increase of the experimental sensitivity will thus yield a test of such theories.

1.2.2 The basic principle of EDM measurements

Experimental EDM searches rely on the fact that the magnetic moment $\vec{\mu}$ and the EDM \vec{d} are colinear with the spin. The interaction of a neutron at rest with an external magnetic field \vec{B} and electric field \vec{E} can be expressed by the Hamiltonian

$$H = -\vec{\mu} \cdot \vec{B} - \vec{d} \cdot \vec{E} = -\frac{\vec{S}}{S}(\mu\vec{B} + d\vec{E}), \quad (1.22)$$

where we used Eqs. 1.15 and 1.17. In the following we assume $\vec{B} \parallel \vec{E}$. The first term in Eq. 1.22 leads to the well-known Larmor precession with the Larmor frequency $\omega_L = 2\mu B/\hbar$ ⁸, while the second term is

⁸While this expression for the Larmor frequency is widely used in particle physics (see for example [25, 26]), it may create some confusion for atomic physicists. The interaction of the neutron with a magnetic field \vec{B}_0 is

$$H = -\vec{\mu} \cdot \vec{B}_0 = -g_n \mu_N \vec{S} \cdot \vec{B}_0,$$

where $g_n = -3.826\,085\,46(90)$ denotes the neutron g-factor and $\mu_N = 5.050\,783\,43(43) \times 10^{-27} \text{ J/T}$ the nuclear magnetic moment. Analogous to Eq. 1.1, the energy shift of the neutron depending on its spin projection along the magnetic field direction, $M_S = \pm 1/2$, is

$$\Delta E = g_n \mu_N M_S B_0,$$

and the Larmor frequency is

$$\omega_L = \gamma_n B_0 = \frac{g_n \mu_N}{\hbar} B_0,$$

where $\gamma_n = \frac{g_n \mu_N}{\hbar} \approx 2\pi \times 29.16 \text{ Hz}/\mu\text{T}$ is the gyromagnetic ratio of the neutron. With $\vec{\mu} = g_n \mu_N \vec{S}$ and Eq. 1.15 the maximum projection of the neutron magnetic moment in any given direction is $\mu = g_n \mu_N S$. Thus, with $S = 1/2$ the Larmor frequency can be written as

$$\omega_L = \frac{2\mu B}{\hbar}.$$

its electric equivalent, the “electric Larmor frequency”, $\omega_E = 2dE/\hbar$. Because \vec{B} is an axial vector and \vec{E} is a polar vector, the scalar product $\vec{B} \cdot \vec{E}$ also forms a T and P pseudo-scalar. Therefore an experiment using the relative change of the applied magnetic and electric field directions can be used to measure a possible EDM, leading to

$$\omega_{\pm} = \omega_L \pm \omega_E, \quad (1.23)$$

where ω_{\pm} denotes the resulting precession frequency under the combined interaction of the magnetic and electric field, and the indices \pm refer to the parallel or antiparallel orientation of \vec{B} and \vec{E} . Thus the signature of the EDM is an absolute shift $\Delta\omega = \omega_+ - \omega_-$ in the measured Larmor frequency when the relative orientation of \vec{B} and \vec{E} is changed from parallel to antiparallel:

$$d = \frac{\hbar\Delta\omega}{4E}. \quad (1.24)$$

In the case of $B = 1 \mu\text{T}$, $E = 10 \text{ kV/cm}$, and d on the order of $10^{-27} \text{ e}\cdot\text{cm}$, the frequency shift is $\Delta\omega/2\pi = 10 \text{ nHz}$ with $\omega_L/2\pi = 29.2 \text{ Hz}$, which corresponds to a relative frequency change of $\Delta\omega/\omega_L = 3 \times 10^{-10}$! The art of nEDM experiments is to reach the required sensitivity to resolve such small frequency changes, while controlling at the same time systematic effects at the same level.

1.2.3 The Ramsey method of separated oscillatory fields

The experimental search for the nEDM started in the 1950’s. The most important step towards lowering the measurement uncertainty by about one order of magnitude every 8 years [23] was based on the pioneering work of N. F. Ramsey who invented a magnetic resonance technique using spatially separated oscillatory magnetic fields, the so-called Ramsey method [25]. Originally this method was used for a neutron beam experiment and yet it remains the basis for modern experiments. During 30 years the neutron beam experiments were improved, but they all suffered from serious systematic effects induced by the motional fields experienced by the neutrons moving in the electric and magnetic fields. A detailed overview of the different experimental techniques and improvements can be found in [26]. In the following we focus only on modern nEDM experimental techniques using ultra-cold neutrons (UCN), which started in the 1980’s as a variant of the original method.

Ultra-cold neutrons are neutrons with an energy smaller than about 300 neV, which corresponds to a velocity of less than 8 m/s and an effective temperature of less than 2 mK. The interaction with solid matter is characterized by the large deBroglie wavelength, $\lambda = h/p$, on the order of 50 nm. When interacting with solid matter the neutrons “feel” an effective wall potential, V , made from the averaged Fermi-potential of the atoms in the solid. In solid matter the UCNs are coherently scattered by a large number of atoms and the interaction can be characterized by an index of refraction, $n < 1$, similar to optical processes. Depending on the potential V the critical angle of total reflection can reach practically normal incidence [27, 28]. In this way it is possible to store UCNs in a material “bottle” which is usually made from a substrate material such as stainless steel or aluminum, with its inner walls covered by a several hundred nanometer thick layer of material with high neutron potential V such as ^{58}Ni (335 neV), Be (252 neV), or diamond-like carbon (DLC, 300 neV) [26]. The storage time in such bottles can reach several minutes, which is an essential feature for EDM experiments as it allows much longer interaction times of the neutrons with the magnetic and electric fields when compared to the former beam experiments.

Measuring the neutron precession frequency in the presence of static magnetic and electric fields by the magnetic resonance technique is related to the discussion in Sec. 1.1.3, especially to the three-step interpretation. Before going into the details of the particular realization we address the main differences between the magnetic resonance detection in the case of Cs and in the case of neutrons, which are neutral spin-1/2 particles. While the Cs atoms are polarized by optical means, the neutrons are polarized either by the (relative) spin-dependent absorption in a sample of spin-polarized ^3He gas or by a spin filter, which is based on the spin-dependent reflection/transmission coefficients of neutrons incident on magnetized thin foils [29]. The macroscopic polarization of the neutron sample is defined as the difference

of the number of neutrons with their spin along $+z$ (spin up), N_+ , and with their spin along $-z$ (spin down), N_- , normalized to the total number of neutrons, $N_0 = N_+ + N_-$. Counting N_+ and N_- by means of a spin-selective detector yields

$$P_z = \frac{N_+ - N_-}{N_+ + N_-}. \quad (1.25)$$

In the following we assume a neutron sample initially polarized along the z -axis, i.e., $P_z = P_0 = 1$.

In addition to the small magnetic moment of the neutron, UCN samples are very dilute (on the order of 10 UCN/cm³ in experiments close to the UCN source at ILL). Thus, one can neglect depolarizing neutron-neutron collisions as well as spin-depolarizing neutron-wall collisions, and the spin relaxation times T_1 and T_2 can be considered much longer than the duration of the experiment. Considering the neutrons exposed to a static magnetic field, \vec{B}_0 , and a r.f. field, \vec{B}_1 , the neutron polarization can be described by Eqs. 1.6, 1.7, and 1.8, setting $\Gamma_1 = \Gamma_2 = 0$. From the general solution of the differential equations and with the initial conditions $\vec{P}(t=0) = (0, 0, P_0)$ one obtains for the z -component

$$P_z = \frac{\delta\omega^2 + \Omega_R^2 \cos(\Omega_{\text{eff}} t)}{\Omega_{\text{eff}}^2} = 1 - \frac{2\Omega_R^2}{\delta\omega^2 + \Omega_R^2} \sin^2\left(\frac{\Omega_{\text{eff}} t}{2}\right), \quad (1.26)$$

where $\Omega_{\text{eff}} = \sqrt{\delta\omega^2 + \Omega_R^2}$. Recall that $\delta\omega$ is the relative detuning of the Larmor frequency and the applied radio frequency, and $\Omega_R = \gamma B_1$ is the Rabi frequency.

Rather than continuously monitoring the precession frequency, as in the case of Cs, the neutron precession frequency measurement is based on discrete time sequential steps. In the discussion in Sec. 1.1.3 we have seen that on resonance ($\delta\omega = 0$) P_z changes periodically from $+P_0$ to $-P_0$ with the Rabi frequency Ω_R . Thus an r.f. field which is applied for a time τ , defined by

$$\Omega_R \tau = \pi, \quad (1.27)$$

will flip the polarization by 180° from $P_z = +P_0$ to $P_z = -P_0$. Such an applied field is called a “ π -pulse”. If the duration of the r.f. pulse fulfills the condition $\Omega_R \tau = \pi/2$, the initial polarization along the z -axis is rotated into the xy -plane (“ $\pi/2$ -pulse”).

With this knowledge one can understand the principles of the Ramsey-type magnetic resonance experiment using time-separated oscillating magnetic fields, as shown in Figs. 1.3 and 1.4 in the frame co-rotating with \vec{B}_1 and the laboratory frame, respectively:

1. A sample of spin polarized UCNs is accumulated in the storage volume exposed to a static field $\vec{B}_0 = (0, 0, B_0)$. All individual neutron spins — and therefore the magnetic and electric dipole moments — are oriented in the $+z$ -direction, yielding a macroscopic polarization $P_z = P_0$.
2. A $\pi/2$ -pulse is applied with the r.f. field B_1 along the x' -axis in the rotating frame. At the end of the pulse the neutron polarization points along the y' -axis in the rotating frame.
3. After the r.f. pulse is switched off, the spins precess freely for a time T . For $\delta\omega = 0$ in the rotating frame there is no magnetic field at all so that the spins do not rotate. If the Larmor frequency is slightly detuned with respect to the Larmor frequency, or more precisely to the mean Larmor frequency during the time T where only the *relative* change between the Larmor frequency and the radio frequency is important, the neutrons experience a small magnetic field $B_r = -\delta\omega/\gamma$ in the rotating frame and accumulate a phase $\Delta\phi = \delta\omega T$.
4. A second $\pi/2$ -pulse, which is phase coherent with the first one, is applied to the neutrons. Only if

$$\Delta\phi = 2\pi \cdot n \quad (1.28)$$

with n being an integer number, B_1 will be perpendicular to the polarization which is then rotated to $P_z = -P_0$. If the r.f. frequency is slightly detuned with respect to the neutron Larmor frequency

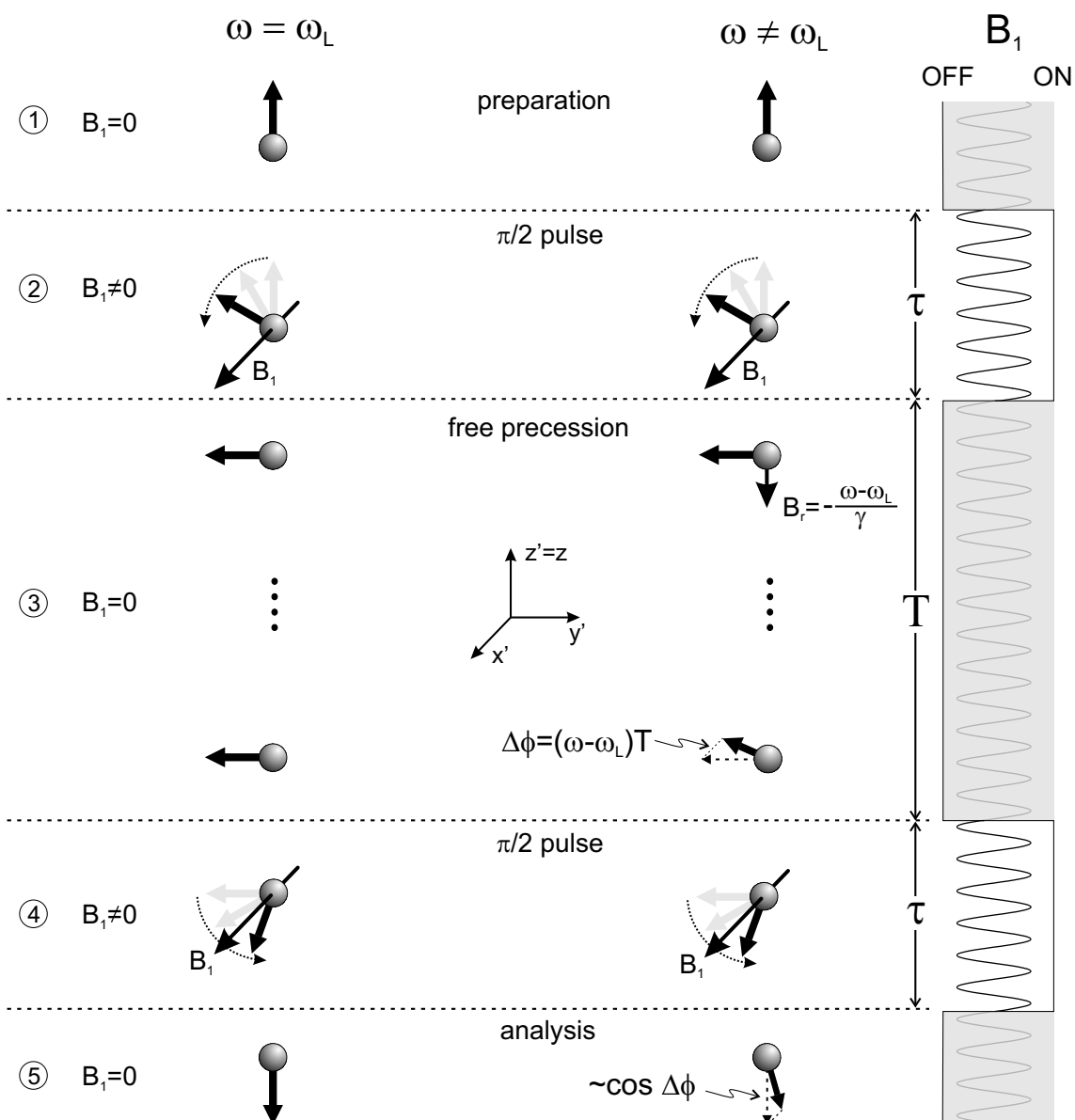


FIGURE 1.3: Ramsey-type magnetic resonance in the *rotating* frame, with the oscillating r.f. field on resonance (left) and slightly detuned from resonance (right). The numbers refer to the description in the text.

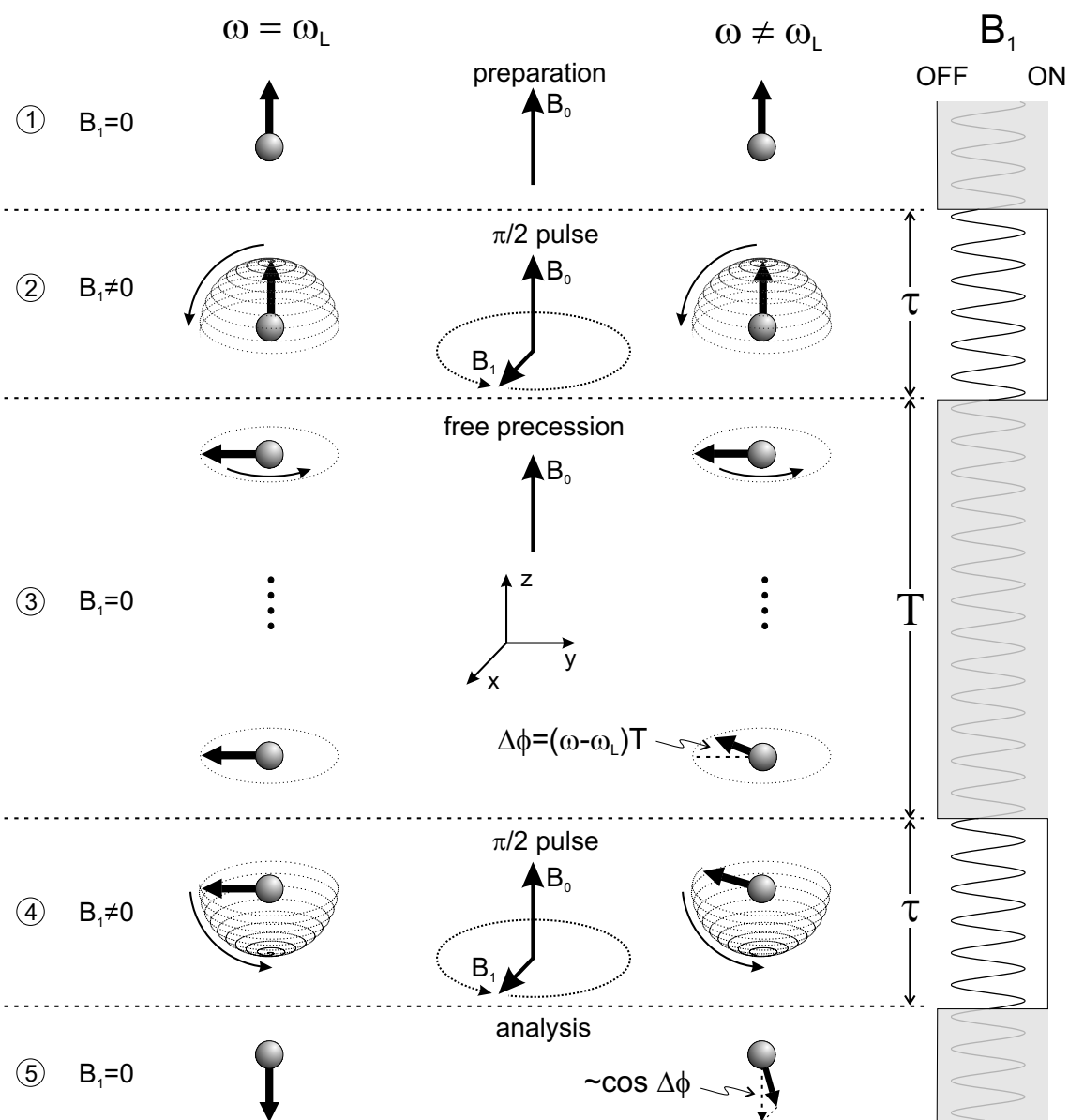


FIGURE 1.4: Ramsey-type magnetic resonance in the *laboratory* frame, with the oscillating r.f. field on resonance (left) and slightly detuned from resonance (right). The numbers refer to the description in the text.

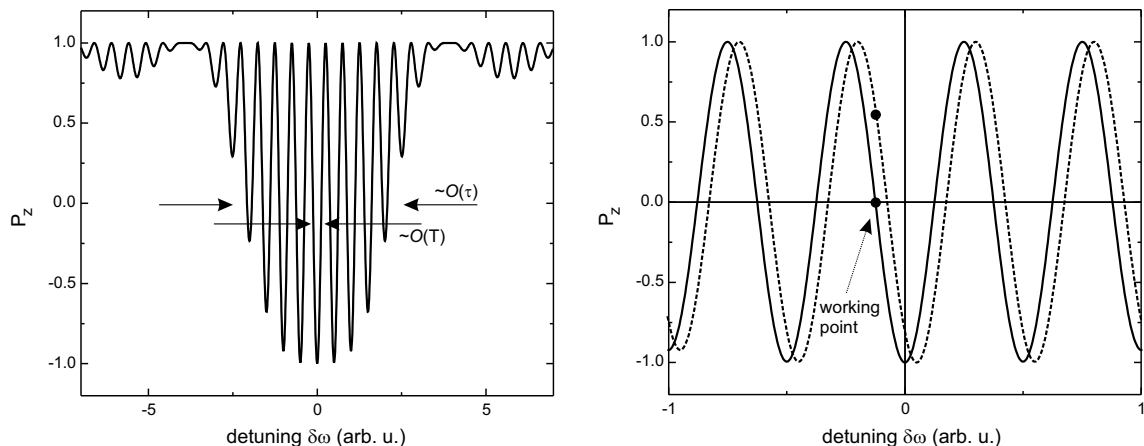


FIGURE 1.5: Left: The neutron polarization component P_z after a complete Ramsey cycle as function of the detuning $\delta\omega$ (with the two $\pi/2$ -pulses in phase). The initial polarization was $P_z = P_0 = +1$. Right: The central part of the Ramsey pattern. The dashed curve indicates the polarization change at the working point due to a change of the resonance frequency such as the frequency shift induced by an EDM coupled to an electric field.

only the polarization component $P_{y'} = P_0 \cos \Delta\phi$ will be rotated by the r.f. field during the second $\pi/2$ -pulse, yielding a final polarization

$$P_z = -P_0 \cos \Delta\phi \quad (1.29)$$

Note that only the phase of the second $\pi/2$ -pulse with respect to the first is important, whereas the second pulse can start after any time T . As long as the condition Eq. 1.28 holds, the polarization is completely rotated.

5. A polarization-selective detector is used to measure P_z by counting N_+ and N_- (Eq. 1.25).

With the general solution of Eqs. 1.6, 1.7, and 1.8 and with $\Gamma_1 = \Gamma_2 = 0$ we can determine P_z as a function of $\delta\omega$ and T . Figure 1.5 shows the so-called Ramsey pattern. The envelope is given by the Lorentzian part $\frac{2\Omega_R^2}{\delta\omega^2 + \Omega_R^2}$ in Eq. 1.26 with a full width at half maximum of $2\Omega_R$. The width of a single fringe is determined by the free precession time T .

Usually the radio frequency is tuned to the side of the central fringe with the steepest slope so that $P_z = 0$ in the absence of the electric field (“working point”), as shown on the right-hand side in Fig. 1.5. In the presence of an additional electric field \vec{E} (anti)parallel to \vec{B}_0 the precession frequency is slightly changed by $\pm\omega_E$ due to the additional torque $\vec{d} \times \vec{E}$ that acts on the neutrons. Thus the Ramsey pattern will be shifted depending on the relative orientation of \vec{E} and \vec{B}_0 . The resulting systematic change of P_z in the presence of the electric field will uncover the desired information about the nEDM. Knowing the slope at the working point and measuring the polarization dependence on the electric field orientation the precession frequencies ω_{\pm} can be extracted.

Instead of detuning the r.f. frequency to a zero crossing near the central fringe the second $\pi/2$ -pulse can be applied with a 90° phase shift with respect to the first one. For the second $\pi/2$ -pulse \vec{B}_1 is parallel to the y' -axis and, if $\delta\omega = 0$, parallel to the polarization. Thus there is no effective precession around \vec{B}_1 . This is equivalent to a change of the cosine to a sine dependence in Eq. 1.29. Therefore the polarization analysis after the Ramsey cycle yields $P_z = 0$, i.e., a zero-crossing with the steepest slope of the Ramsey pattern on resonance. It can be shown that, neglecting the sign that depends on the sign of the phase shift, the slope at this point is

$$\left. \frac{\partial P_z}{\partial \delta\omega} \right|_{\delta\omega=0} = P_0 \cdot \left(T + \frac{\pi + 2}{2\Omega_R} \right) \stackrel{T \gg 1/\Omega_R}{\approx} P_0 \cdot T. \quad (1.30)$$

1.2.4 Statistical measurement uncertainty

In the prior discussion we have seen that the absolute change of the neutron precession frequency due to the EDM is directly proportional to the magnitude of the electric field E (Eq. 1.24). Under ideal conditions the uncertainty in d , $\sigma(d)$, depends on the uncertainty $\sigma(\Delta\omega)$ in measuring the frequency difference $\Delta\omega$:

$$\sigma(d) = \frac{\sigma(\Delta\omega) \cdot \hbar}{4E}. \quad (1.31)$$

In the following we will call two consecutive Ramsey cycles each with one of the electric field orientations, measuring ω_+ and ω_- respectively, a “measurement cycle”. Assuming a Ramsey procedure with a 90° phase-shifted second $\pi/2$ -pulse, the working point, i.e., the final polarization without electric field, is at a zero crossing of a central Ramsey fringe. With Eq. 1.30 (and $P_0 = 1$), the uncertainty in extracting the precession frequency from the polarization analysis after a single Ramsey cycle is

$$\sigma(\omega) = \frac{1}{T}\sigma(P_z), \quad (1.32)$$

where the uncertainty of the polarization measurement, $\sigma(P_z)$, is approximately $1/\sqrt{N_0}$. Thus we obtain the uncertainty on the nEDM:

$$\sigma(d) = \frac{\hbar}{2\sqrt{2}\varepsilon ET\sqrt{N_0}}. \quad (1.33)$$

The coefficient $\varepsilon \leq 1$ was added in order to take into account inefficiencies due to the neutron polarization/detection and spin depolarization (relaxation) during the measurement cycle. After m measurement cycles $\sigma(d)$ will be lowered by a factor $1/\sqrt{m}$.

However, Eq. 1.24 is valid only if the magnetic field has the same average value during the measurements of ω_+ and ω_- . A change of the magnetic field between two subsequent Ramsey cycles together with a change of the electric field orientation leads to a false EDM:

$$d = \frac{\hbar\Delta\omega - 2\mu\Delta B}{4E}, \quad (1.34)$$

where $\Delta B = B_+ - B_-$ is the magnetic field change between the measurement with parallel (B_+) and antiparallel (B_-) field configuration. Thus the contribution to the EDM uncertainty arising from uncorrelated magnetic field fluctuations in m measurement cycles is

$$\sigma_{(B)}(d) = \frac{\mu\Delta B}{2E\sqrt{m}}. \quad (1.35)$$

From Eqs. 1.33 and 1.34 we can derive the major requirements for an nEDM experiment:

1. As was stated above, the magnitude of the electric field has to be as large as possible.
2. The sensitivity depends directly on the free precession time T in order to gain a measurable phase shift $\Delta\phi$ for small $\delta\omega$.
3. As one would expect from the measurement of N_0 independent systems, $\sigma(d)$ decreases with the square root of the neutron number, thus demanding a neutron density as high as possible in combination with a maximum storage volume.
4. A high temporal and spatial magnetic field stability is indispensable. Particularly harmful are systematic B-field shifts that appear synchronously with the polarity change of the electric field, for example due to leakage currents induced by the high voltage. It is therefore crucial to identify and suppress such field fluctuations.

1.2.5 Some words about the PSI-nEDM experiment

In the following we will only outline the setup of the PSI-nEDM experiment with special emphasis on the magnetometry aspect.

The concept of the PSI-nEDM experiment will be similar to the RAL-Sussex-EDM experiment [22, 30] carried out over the past 20 years at the Institut Laue-Langevin (ILL) in Grenoble, France. In that experiment polarized ultra-cold neutrons were stored in a single neutron chamber (quartz cylinder of about 20 l), enclosed between two DLC-coated electrodes. The electric field was reversed by changing the polarity of one electrode while keeping the other grounded. The neutron chamber was located in a vacuum chamber inside a cylindrical four-layer magnetic shield with an inner diameter of about 1 m made of Mumetal, and providing a shielding factor of about 10^5 [22].

A very important point for the ultimate performance of that setup was the use of a ^{199}Hg co-magnetometer [31]. Polarized ^{199}Hg atoms were stored in the same volume as the neutrons, and their Larmor precession was measured by optical means. Up to gravitational corrections for the center of the Hg and the neutron distribution in the storage volume, the magnetic field averaged by the Hg atoms coincided with the average field seen by the neutrons. In that way magnetic field fluctuations during the neutron free precession time could be monitored and corrected for. However, it was reported that the sensitivity of the co-magnetometer leads to an uncertainty in the nEDM measurement of about 20% [26] of the reported nEDM upper limit of $d < 6.3 \times 10^{-26} \text{ e} \cdot \text{cm}$ [22]. Thus in an experiment with a hundred times higher neutron density the use of that co-magnetometer will be a severe limiting factor.

The main point in lowering the existing limit on the nEDM in the PSI-nEDM-experiment will be the improvement of the statistical uncertainty while keeping systematic effects under control. A statistical improvement requires a larger number of neutrons, which will be delivered by the new UCN source under construction at PSI. The new source will provide a 100 times higher neutron density than the current ILL-UCN source [32].

In the PSI-nEDM experiment it is planned to install a double chamber consisting of two identical chambers with opposite electric field orientations rather than a single neutron volume (with a single electric field). This will not only reduce the measurement time due to the doubling of the experimental volume, but it will also suppress systematic effects due to temporal magnetic field fluctuations, as long as the spatial homogeneity is maintained. If a required sensitivity of $\sigma(d) = 10^{-27} \text{ e} \cdot \text{cm}$ ($E = 10 \text{ kV/cm}$) can be obtained in a single measurement cycle, Eq. 1.35 yields $\Delta B = 0.66 \text{ fT}$ (for the duration of the measurement cycle). However, with one measurement cycle lasting 1200 s (600 s per Ramsey cycle) and 250 days of measurements per year [33], i.e., $m = 18000$, the requirement for the magnetic field stability relaxes to $\Delta B = 90 \text{ fT}$ for the duration of one measurement cycle, reaching the same uncertainty after one year of data taking. This constraint on the magnetic field stability is still very challenging.

There are two principle solutions to the problem: 1) the magnetic field fluctuations can be suppressed below the required level by a suitable shielding. In that case no magnetometry system would be necessary. However, with conventional room-temperature magnetic shielding it is quite impossible to meet the requirement. 2) The field fluctuations are measured by a sufficiently sensitive and fast magnetometry system, and this information can be used to actively stabilize and correct for magnetic field fluctuations, as well as track and correct the phase of the Larmor precession.

For the PSI-nEDM experiment the second solution will be chosen. Instead of, or more probably in addition to, an (improved) co-magnetometer, a magnetometer array around the neutron storage chamber(s) will measure the magnetic field at many locations⁹. Each sensor has to provide an intrinsic resolution that is below the required field stability. The sensor array will consist of Cs magnetometers pumped by a single laser source. Their design, realization, and performance characterization are the main subject of this dissertation.

The crucial point of any magnetometer system is to determine the field magnitude as well as the gradients *inside* the neutron storage volume, also with an “external” sensor array. In this case the

⁹At present, sensing at 14 locations is eventually foreseen.

knowledge of the spatial and temporal magnetic field distribution is indispensable. It can be shown that with a sufficient number of well-positioned sensors the field at the neutron volume can be determined at a sufficient level in terms of a multipole expansion.

In the framework of the PSI-nEDM collaboration an 8-sensor LsOPM array was set up and successfully tested in the existing RAL-Sussex apparatus. In Figs. 1.6, 1.7, and 1.8 several details of the experimental setup are shown. As it will be discussed in detail in the following chapters, the sensitivity of the individual sensors in combination with the associated read-out and data-analysis system have proven to be sufficient for the nEDM task.

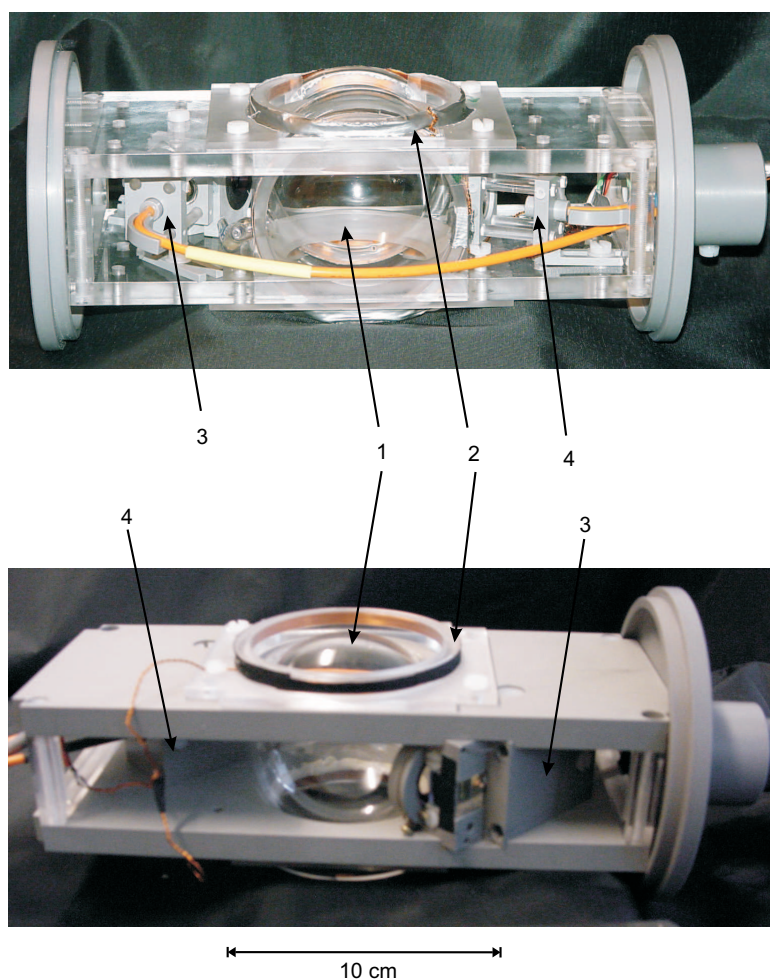


FIGURE 1.6: Magnetometry system I: Top: The prototype of the non-magnetic sensor head (without the cylindrical shield). Bottom: A nearly completely mounted “heavy duty” variant of the sensor head as it was used for the measurements at ILL. 1: 70 mm diameter glass sphere filled with Cs vapor, 2: the r.f. coils, 3: fiber coupling optics and polarizer, 4: fiber coupling optics to guide the light back to the feedback electronics.

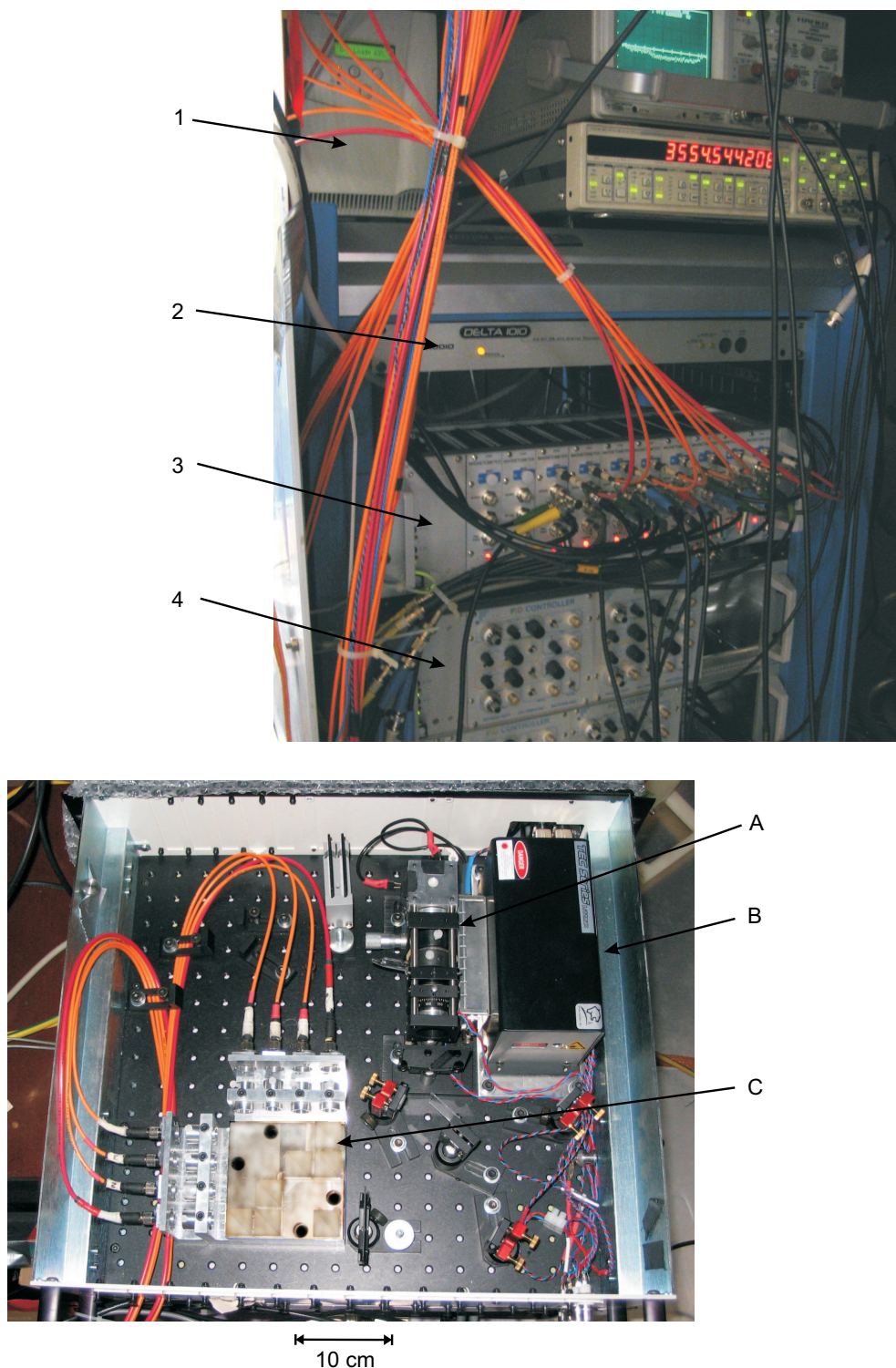


FIGURE 1.7: Magnetometry system II: Top: Main part of the electronics: 1: UPS unit to protect the laser electronics against irregularities in the electricity power supply system, 2: sound card for the frequency measurement, 3: electronics modules for 10 self-oscillating LsOPMs, 4: PID controller for the laser-frequency stabilization feedback and for the active magnetic-field stabilization. Bottom: Portable diode-laser system in a 19" rack drawer. A: laser-frequency stabilization setup with Cs vapor cell, optics and detector (DAVLL), B: extended cavity diode laser (Sacher Lasertechnik TEC 500), C: beam multiplexer with fiber coupling optics. The laser electronics unit (current and temperature stabilization) is in a separate rack not shown here.

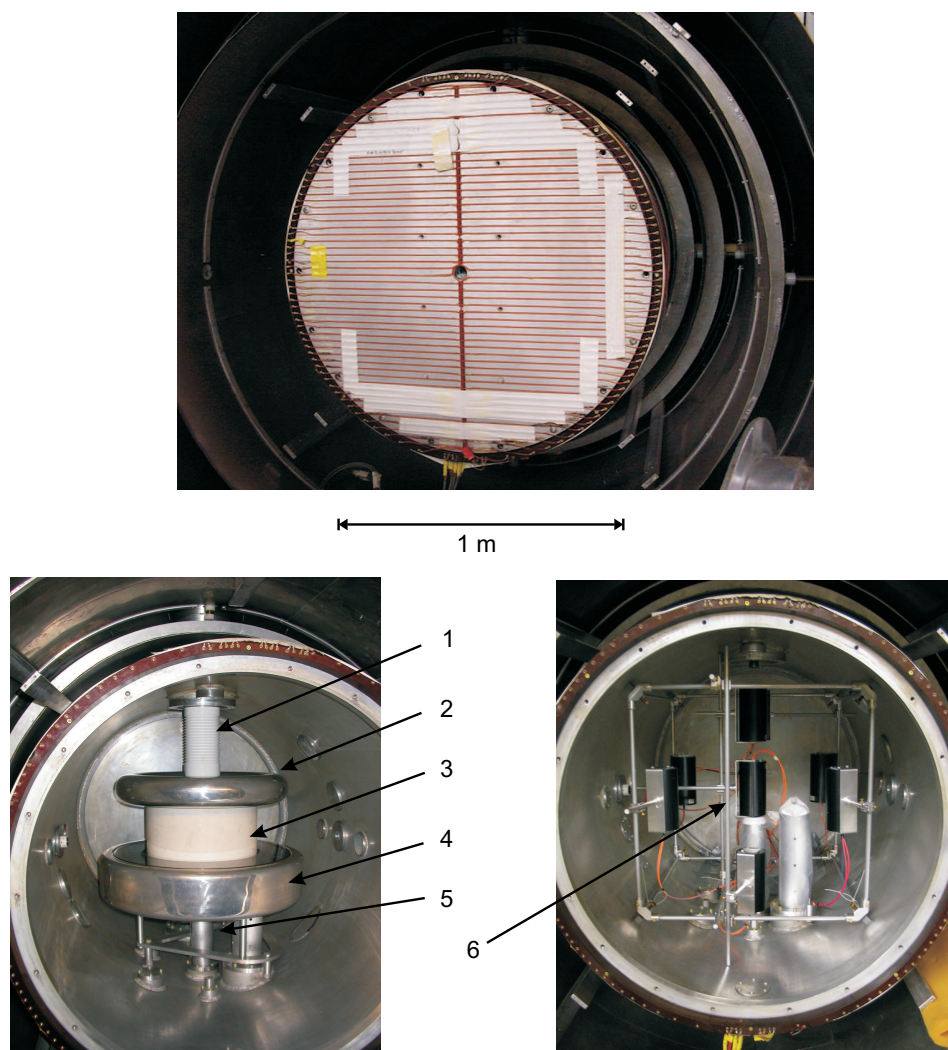


FIGURE 1.8: Top: RAL-Sussex setup: Vacuum tank inside the (opened) 4-layer magnetic shield. On the tank the windings of the main field coil can be seen producing a vertical field of $1\ \mu\text{T}$. Bottom left: Inside the vacuum tank. 1: High voltage feedthrough, 2: upper electrode, 3: neutron volume, 4: lower electrode (grounded), 5: neutron guide. Bottom right: 8-sensor LsOPM array in the RAL-Sussex experiment. The neutron volume was replaced by the central sensor head (6).

References

- [1] H. G. Dehmelt. *Modulation of a light beam by precessing absorbing atoms*. Phys. Rev. **105**(5), 1924–1925 (1957).
- [2] W. E. Bell and A. L. Bloom. *Optical detection of magnetic resonance in alkali metal vapor*. Phys. Rev. **107**(6), 1559–1565 (1957).
- [3] A. L. Bloom. *Principles of operation of the rubidium vapor magnetometer*. Appl. Opt. **1**(1), 61–68 (1962).
- [4] G. Breit and I. I. Rabi. *Measurement of nuclear spin*. Phys. Rev. **38**(11), 2082–2083 (1931).
- [5] J. Brossel and A. Kastler. *La detection de la resonance magnetique des niveaux excites - l'effect de depolarization des radiations de resonance optique et de fluorescence*. C. R. Acad. Sci. URSS **229**, 1213–1215 (1949).
- [6] W. Happer. *Optical pumping*. Rev. Mod. Phys. **44**(2), 169–249 (1972).
- [7] J. B. Taylor and I. Langmuir. *Vapor pressure of caesium by the positive ion method*. Phys. Rev. **51**(9), 753–760 (1937).
- [8] M. A. Bouchiat and J. Brossel. *Relaxation of optically pumped Rb atoms on paraffin-coated walls*. Phys. Rev. **147**(1), 41–54 (1966).
- [9] E. B. Alexandrov and V. A. Bonch-Bruevich. *Optically pumped atomic magnetometers after three decades*. Opt. Eng. **31**(4), 711–717 (1992).
- [10] S. Lang, S. Kanorsky, T. Eichler, R. Müller-Siebert, T. W. Hänsch, and A. Weis. *Optical pumping of Cs atoms in solid ^4He* . Phys. Rev. A **60**(5), 3867–3877 (1999).
- [11] F. Bloch and A. Siegert. *Magnetic resonance for nonrotating fields*. Phys. Rev. **57**(6), 522–527 (1940).
- [12] C. Cohen-Tannoudji, J. Dupont-Roc, S. Haroche, and F. Laloë. *Detection of the static magnetic field produced by the oriented nuclei of optically pumped ^3He gas*. Phys. Rev. Lett. **22**(15), 758–760 (1969).
- [13] A. Weis, J. Wurster, and S. I. Kanorski. *Quantitative interpretation of the nonlinear Faraday effect as a Hanle effect of a light-induced birefringence*. J. Opt. Soc. Am. B **10**(4), 716–724 (1993).
- [14] C. S. Wu, E. Ambler, R. W. Hayward, D. D. Hoppes, and R. P. Hudson. *Experimental test of parity conservation in beta decay*. Phys. Rev. **105**(4), 1413–1415 (1957).
- [15] R. L. Garwin, L. M. Lederman, and M. Weinrich. *Observations of the failure of conservation of parity and charge conjugation in meson decays: the magnetic moment of the free muon*. Phys. Rev. **105**(4), 1415–1417 (1957).
- [16] J. I. Friedman and V. L. Telegdi. *Nuclear emulsion evidence for parity nonconservation in the decay chain $\pi^+ - \mu^+ - e^+$* . Phys. Rev. **105**(5), 1681–1682 (1957).
- [17] J. H. Christenson, J. W. Cronin, V. L. Fitch, and R. Turlay. *Evidence for the 2π decay of the K_2^0 meson*. Phys. Rev. Lett. **13**(4), 138–140 (1964).
- [18] F. Abe et. al. *Measurement of the CP-violation parameter $\sin(2\beta)$ in $B_d^0/\bar{B}_d^0 \rightarrow J/\psi K_S^0$ decays*. Phys. Rev. Lett. **81**(25), 5513–5518 (1998).
- [19] G. Lüders and B. Zumino. *Some consequences of TCP-invariance*. Phys. Rev. **106**(2), 385–386 (1957).
- [20] A. Angelopoulos et al. *First direct observation of time-reversal non-invariance in the neutral-kaon system*. Phys. Lett. **444**(1–2), 43–51 (1998).
- [21] J. H. Smith, E. M. Purcell, and N. F. Ramsey. *Experimental limit to the electric dipole moment of the neutron*. Phys. Rev. **108**(1), 120–122 (1957).

-
- [22] P. G. Harris, C. A. Baker, K. Green, P. Iaydjiev, S. Ivanov, D. J. R. May, J. M. Pendlebury, D. Shiers, K. F. Smith, M. van der Grinten, and P. Geltenbort. *New experimental limit on the electric dipole moment of the neutron*. Phys. Rev. Lett. **82**(5), 904–907 (1999).
- [23] J. M. Pendlebury and E. A. Hinds. *Particle electric dipole moments*. Nucl. Instr. and Meth. A **440**(3), 471–478 (2000).
- [24] A. D. Sakharov. *Violation of CP invariance, C asymmetry and baryon asymmetry of the universe*. JETP Lett. **5**, 24–27 (1967).
- [25] N. F. Ramsey. *Molecular Beams*. Oxford University Press New York (1956).
- [26] I. B. Khriplovich and S. K. Lamoreaux. *CP violation without strangeness*. Springer Verlag, Berlin (1997).
- [27] R. D. Golub, D. J. Richardson, and S. K. Lamoreaux. *Ultra-cold Neutrons*. Adam Hilger Bristol, Philadelphia, New York (1991).
- [28] V. K. Ignatovitch. *The Physics of Ultracold Neutrons*. Clarendon Press Oxford (1990).
- [29] O. Zimmer, P. Hautle, W. Heil, D. Hofmann, H. Humblot, I. Krasnoschekova, M. Lasakov, T. M. Müller, V. Nesvizhevsky, J. Reich, A. Serebrov, Yu. Sobolev, and A. Vassilev. *Spin filters and supermirrors: a comparison study of two methods of high-precision neutron polarisation analysis*. Nucl. Instr. and Meth. A **440**(3), 764–771 (2000).
- [30] P.G. Harris, D.J.R. May, J.M. Pendlebury, D. Shiers, K.F. Smith, M. van der Grinten, C.A. Baker, K. Green, P. Iaydjiev, S. Ivanov, and P. Geltenbort. *The neutron EDM experiment at the ILL*. Nucl. Instr. and Meth. A **440**(3), 479–482 (2000).
- [31] K. Green, P. G. Harris, P. Iaydjiev, D. J. R. May, J. M. Pendlebury, K. F. Smith, M. van der Grinten, P. Geltenbort, and S. Ivanov. *Performance of an atomic mercury magnetometer in the neutron EDM experiment*. Nucl. Instr. and Meth. A **404**(2–3), 381–393 (1998).
- [32] URL <http://ucn.web.psi.ch/> (2005).
- [33] G. Ban et al. *Measurement of the neutron electric dipole moment*. PSI Proposal R-05-03.1 (2005).

Chapter 2

Design and performance of laser-pumped Cs magnetometers for the planned UCN EDM experiment at PSI

S. Groeger^{1,2}, G. Bison¹, and A. Weis¹

¹*Département de Physique, Université de Fribourg, Chemin du Musée 3, 1700 Fribourg, Switzerland*

²*Paul Scherrer Institute, 5232 Villigen PSI, Switzerland*

Published in J. Res. Natl. Inst. Stand. Technol. **110**(3), 179–183 (2005).

ABSTRACT: We discuss the performance of a laser-pumped cesium vapor magnetometer in the M_x configuration. The device is designed for the control and stabilization of fluctuating magnetic fields and gradients in a new experiment searching for a permanent electric dipole moment of the neutron. We have determined the intrinsic sensitivity of the device to be 30 fT in a measurement bandwidth of 1 Hz, limited by laser noise. In the shot noise limit the magnetometer can reach a sensitivity of 7 fT for 1 s integration time. Test experiments in a threefold magnetic shield have shown fluctuations of a $2 \mu\text{T}$ magnetic field on the order of 200–300 fT with integration times in the range of 2–100 seconds. Those fluctuations are traced back to the stability of the power supply used to generate the field. Consequences for neutron EDM experiments are discussed.

Key words: high precision magnetometry; laser spectroscopy; optical detected magnetic resonance; optical pumping.

2.1 Introduction

The precise measurement and control of magnetic fields and magnetic field fluctuations is important for experiments searching for a permanent electric dipole moment (EDM) of the neutron, hence it is one of the main factors limiting the accuracy. In a project approved by Paul Scherrer Institute (PSI) in Switzerland a neutron EDM spectrometer is proposed [1], in which the neutron spin flip transition frequency is measured in four UCN storage chambers exposed to a homogenous $2\ \mu\text{T}$ magnetic field. In addition each neutron chamber has two compartments in which the neutrons are exposed to a static electric field of $15\ \text{kV}/\text{cm}$ oriented parallel/antiparallel to the magnetic field. The signature of a finite EDM is a change of the neutron Larmor frequency that is synchronous with the reversal of the relative orientations of the magnetic and electric fields. This experiment imposes very stringent constraints on the homogeneity and on the stability of the magnetic field.

Fluctuations of the magnetic field will be monitored by a set of 16 optically pumped alkali vapor magnetometers (OPM), using the property that the oscillation frequency of the OPMs is proportional to the modulus of the magnetic field at their location. The magnetometers considered for the first generation of the neutron EDM experiment are self-oscillating Cs vapor magnetometers (OPM) in the M_x configuration [2, 3], optically pumped by spectral discharge lamps (LpOPM). However, it was shown previously that the replacement of the lamp by a resonant laser can lead to an appreciable gain in magnetometric sensitivity [3, 4]. In that spirit we have designed and tested a laser-pumped OPM (LsOPM) with a geometry compatible with the neutron EDM experiment under construction. In case the laser version shows superior performance it might be considered as an alternative to the lamp-pumped magnetometers in the EDM experiment. Here we present the design and discuss the performance of Cs-LsOPMs operated in a phase-stabilized mode.

2.2 The magnetometer setup

The magnetometer consists of three parts (Fig. 2.1): a) a sensor head containing no metallic parts except

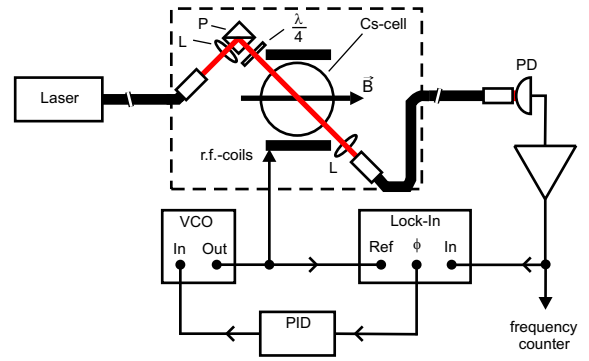


FIGURE 2.1: Schematic setup of the phase-stabilized magnetometer. The dashed box indicates the sensor head. L: lens, P: polarizing beamsplitter, $\lambda/4$: quarter-wave plate, PD: photodiode, VCO: voltage-controlled oscillator, PID: feedback amplifier. The stabilization system of the laser frequency is not shown.

the r.f. coils, b) a base station mounted in a portable 19" rack drawer, which contains the frequency stabilized laser and all optics, and c) the frequency locking electronics. The sensor head is designed to fit into a tube of 104 mm diameter, coaxial with the $2\ \mu\text{T}$ field, and has a total length of 242 mm. Its main component is a paraffin-coated, 7 cm diameter glass cell containing a droplet of cesium. The Cs atoms in the vapor are optically pumped by a circularly polarized light beam, oriented at 45° to the magnetic field. An extended-cavity diode laser, which is stabilized on the $F = 4 \rightarrow F = 3$ hyperfine component of the D_1 line at 894 nm wavelength by the dichroic atomic vapor laser lock (DAVLL) method [5], provides the resonant light which is guided from the base station to the sensor head via a 10 m long multimode fiber ($800\ \mu\text{m}$ core diameter). The light transmitted through the cell is carried back to the detection unit by a similar fiber. The pumping process produces a polarization (magnetization) in the sample which undergoes a Larmor precession with the frequency ω_L . The precession is resonantly driven by a weak radio-frequency field (with amplitude B_1 and frequency ω_{rf}) applied with a pair of circular coils surrounding the cell. The absorption of the pumping light depends on the direction of the magnetization with respect to the light direction. Therefore the resonant precession frequency appears as an amplitude modulation on the light power transmitted through the cesium vapor. The detection of the modulated transmission by a photodetector allows a direct measure of the

magnetic field in terms of the Larmor frequency.

The system behaves like a classical oscillator, i.e. when a r.f. field is applied, the phase of the response (i.e. the AC component of the transmitted laser intensity) depends on the detuning $\delta\omega = \omega_{\text{rf}} - \omega_{\text{L}}$: for $\delta\omega \ll 0$ the atoms follow the driving field adiabatically and thus the phase shift between the applied frequency and the light modulation is 0° . For $\delta\omega \gg 0$ the phase shift is -180° , while on resonance, i.e. $\delta\omega = 0$, the phase shift is -90° and a maximum modulation on the transmitted light appears. In the phase-stabilized mode this dependency is used to lock the radio frequency to the Larmor frequency: The photodiode signal is applied to a dual-channel lock-in amplifier, referenced by the driving frequency of the r.f. coils produced by a voltage controlled oscillator (VCO). Either the phase or the dispersive in-phase output of the lock-in amplifier can be used in a feedback loop to lock the driving frequency to the Larmor frequency by stabilizing the phase shift to -90° .

The bandwidth of the magnetometer, i.e., its temporal response to field changes, is determined by the feedback loop and was measured to be in the order of 1 kHz.

2.3 Performance of the magnetometer

2.3.1 Intrinsic magnetometric sensitivity

We define the intrinsic magnetometric sensitivity of the LsOPM in terms of the noise equivalent magnetic field (NEM). It is the square root of the power spectral density of magnetic field fluctuations at the magnetometer frequency which produce a photodetector signal equal to the power spectral density of the photocurrent at the same frequency, each integrated over a bandwidth f_{bw} . The NEM δB is given by

$$\delta B = \frac{1}{\gamma} \times \frac{\Delta\nu_{\text{HWHM}}}{S/N_{\text{int}}}, \quad (2.1)$$

where γ is approximately 3.5 Hz/nT for ^{133}Cs . $\Delta\nu_{\text{HWHM}}$ is the half width of the resonance and S/N_{int} the signal-to-noise ratio of the photocurrent modulation in the phase-stabilized mode. The signal S is the amplitude of the modulation. When

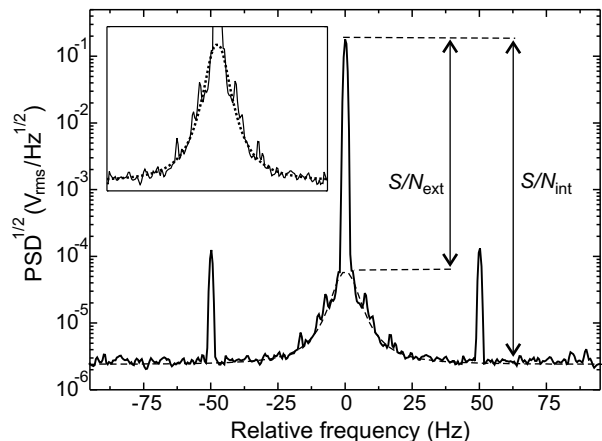


FIGURE 2.2: Square root of the power spectral density (PSD) of the magnetometer output frequency relative to the Larmor frequency of $\nu_0 = 7032$ Hz (averaged 20 times). The spectrum was measured in a 1 Hz bandwidth. The signal-to-noise ratio S/N_{int} is approximately 66000. The sidebands are due to imperfectly shielded magnetic field components oscillating at the 50-Hz power-line frequency. The dotted line shows an approximation of the pedestal. The signal-to-noise ratio S/N_{ext} due to external field noise is found to be approximately 2600.

measuring the intrinsic noise level N_{int} , care has to be taken to eliminate external contributions, such as drifts and noise from external magnetic field sources. We thus infer the intrinsic noise N_{int} from a Fourier analysis of the photodiode signal under optimal conditions (Fig. 2.2). The central peak (the so-called carrier) is the oscillating magnetometer signal. It is superposed on a broad pedestal, which results mainly from a continuous distribution of sidebands due to imperfectly shielded low-frequency field fluctuations. The two discrete sidebands originate from interference of magnetic fields oscillating at the line frequency. The intrinsic noise level N_{int} is given by the noise floor in Fig. 2.2, integrated over the detection bandwidth f_{bw} . It lies 50% above the shot noise level $\Delta I = \sqrt{2eI_{\text{pc}}f_{\text{bw}}}$ of the DC photocurrent I_{pc} in a bandwidth f_{bw} of 1 Hz.

The optimum operating point was found for a laser intensity of $9 \mu\text{W}/\text{mm}^2$ and a B_1 field amplitude of 2.7 nT, which yielded a linewidth $\Delta\nu_{\text{HWHM}} = 3.4(1)$ Hz and a signal-to-noise ratio $S/N_{\text{int}} = 97$ dB = 66000. The corresponding intrinsic sensitivity is $\delta B_{\text{int}} = 14.5$ fT. If one assumes the noise to be white, the sensitivity scales

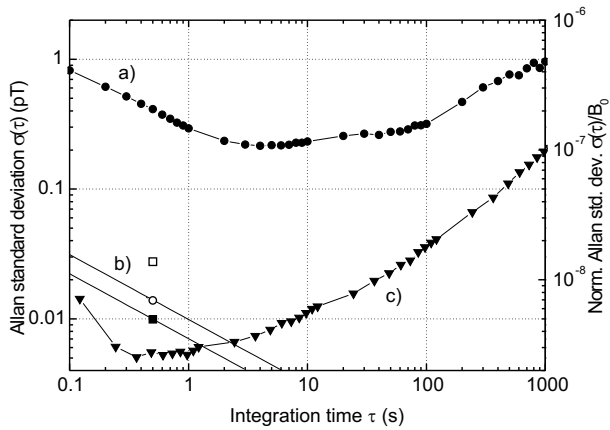


FIGURE 2.3: a) Allan standard deviation of the magnetic flux density inside the magnetic shield (●). b) Intrinsic sensitivity limit. δB_{int}^* (□): sensitivity including $1/f$ noise of the laser power; δB_{int} (○): sensitivity from experimentally determined white noise floor; δB_{SN} (■): anticipated sensitivity for shot noise limited operation. The slopes assume the presence of white noise. c) The triangles (▼) represent the light shift effect due to light power fluctuations. Solid lines in a) and c) are drawn to guide the eye. The dwell time of the frequency counter was 100 ms.

with the square root of the bandwidth. Assuming the photodiode shot noise as ultimate sensitivity limit the LsOPM should reach a sensitivity of $\delta B_{\text{SN}} = 10$ fT in a 1 Hz bandwidth. The laser generated low frequency $1/f$ noise is mixed to the Larmor frequency and thus contributes to the noise spectrum. It was found to exceed the white noise level N_{int} by a factor 2, which yields an intrinsic sensitivity of $\delta B_{\text{int}}^* = 29$ fT. Using an active stabilization of the laser power this contribution can be suppressed.

2.3.2 Application: Field fluctuations in a magnetic shield

We used the LsOPM to measure residual field fluctuations inside a three-fold magnetic shield. The Larmor frequency was recorded as multiple time series of several hours with a sampling rate of 0.1 s. From each time series the Allan standard deviations [6] of the corresponding flux densities inside the shield were calculated. A typical result is shown in Fig. 2.3. The observed fluctuations (Curve a) are well above the intrinsic sensitivity level of the magnetometer (Curves b). For integration times up to 1–2 the noise amplitude decreases as $\tau^{-1/2}$, indi-

cating the presence of white field-amplitude noise. It can be characterized by a spectral amplitude of $413 \text{ fT}/\sqrt{\text{Hz}}$. With the estimated signal-to-noise ratio $S/N_{\text{ext}} = 2600$ (cf. Fig. 2.2) we calculate from Eq. (2.1) a field stability of 370 fT in a measurement bandwidth of 1 Hz, which is in good agreement with the value in the Allan standard deviation plot. The minimum field fluctuations were found to be slightly larger than 200 fT for an integration time of 4 s. The central region of the Allan standard deviation plot shows a plateau for integration times of 2–100 s. It could be traced back to fluctuations of the 8 mA current producing the $2 \mu\text{T}$ bias field and corresponds to a relative stability of 10^{-7} for the power supply. The Allan standard deviations for integration times exceeding 100 s are due to slow drifts of laboratory fields which are not completely suppressed by our 3-layer shield, which has a measured longitudinal shielding factor of 10^3 .

The influence of light shift effects [7, 8] due to light intensity fluctuations are measured in an additional experiment. As in Fig. 2.3c shown, that effect is negligible at the present level of field stability.

2.4 Summary and conclusion

We have described the design and performance of a phase-stabilized cesium vapor magnetometer with a measurement bandwidth up to 1 kHz. The magnetometer has an intrinsic sensitivity of 29 fT, defined as the Allan standard deviation for an integration time of 1 second. This value can be reduced by a factor of 2, if the $1/f$ noise of the laser power can be lowered, e.g., by an active power stabilization. If the excess white noise floor can be reduced to the shot noise level a further increase of 1.5 can be obtained. Under these optimal conditions the LsOPM could reach a sensitivity of 7 fT for a 1 s integration time. Field fluctuations of 200–300 fT were measured in a three-layer magnetic shield for integration times between 2 and 100 seconds. Light shift fluctuations, against which no particular precautions were taken, are one to two orders of magnitude smaller than the residual field fluctuations in the shield.

The laser-pumped OPM described here will thus be a valuable tool for fundamental physics experiments and compares very favorably with state-of-the-art lamp-pumped magnetometers as it will be shown elsewhere.

ACKNOWLEDGMENTS We are indebted to E. B. Alexandrov, A. S. Pazgalev, and R. Wynands for numerous fruitful discussions. We acknowledge financial support from Schweizerischer Nationalfonds, INTAS, and Paul Scherrer Institute (PSI). We thank PSI for the loan of the high-stability current source.

References

- [1] E. Aleksandrov et al. *A new precision measurement of the neutron electric dipole moment (EDM)*. PSI Proposal R-00-05.2 (2002).
- [2] A. L. Bloom. *Principles of operation of the rubidium vapor magnetometer*. Appl. Opt. **1**(1), 61–68 (1962).
- [3] E. B. Aleksandrov, M. V. Balabas, A. K. Verhovskii, A. E. Ivanov, N. N. Yakobson, V. L. Velichanskii, and N. V. Senkov. *Laser pumping in the scheme of an Mx-magnetometer*. Opt. Spectrosc. **78**(2), 325–332 (1995).
- [4] E. B. Aleksandrov. Sov. Phys. Tech. Phys. **35**, 371 (1990).
- [5] V. V. Yashchuk, D. Budker, and J. R. Davis. *Laser frequency stabilization using linear magneto-optics*. Rev. Sci. Instrum. **71**(2), 341–346 (2000).
- [6] J.A. Barnes, A. R. Chi, L.S. Cutler, D.J. Healey, D.B. Leeson, T.E. McGunigal, J.A. Mullen, Jr., W.L. Smith, R.L. Sydner, R.F.C. Vessot, and G.M.R. Winkler. *Characterization of frequency stability*. IEEE Trans. Instrum. Meas. **20**, 105–120 (1971).
- [7] C. Cohen-Tannoudji. *Théorie quantique du cycle de pompage optique*. Ann. Phys. **7**(7–8), 423 (1962).
- [8] C. Cohen-Tannoudji. *Théorie quantique du cycle de pompage optique*. Ann. Phys. **7**(9–10), 469 (1962).

Chapter 3

A high-sensitivity laser-pumped M_x magnetometer

S. Groeger^{1,2}, G. Bison¹, J.-L. Schenker¹, R. Wynands^{1,a}, and A. Weis¹

¹*Département de Physique, Université de Fribourg, Chemin du Musée 3, 1700 Fribourg, Switzerland*

²*Paul Scherrer Institute, 5232 Villigen PSI, Switzerland*

Submitted to Eur. Phys. J. D.

ABSTRACT: We discuss the design and performance of a laser-pumped cesium vapor magnetometer in the M_x configuration. The device will be employed in the control and stabilization of fluctuating magnetic fields and gradients in a new experiment searching for a permanent electric dipole moment of the neutron. We have determined the intrinsic sensitivity of the device to be 15 fT in a 1 Hz bandwidth, limited by technical laser noise. In the shot noise limit the magnetometer can reach a sensitivity of 10 fT in a 1 Hz bandwidth. We have used the device to study the fluctuations of a stable magnetic field in a multi-layer magnetic shield for integration times in the range of 2–100 seconds. The residual fluctuations for times up to a few minutes are traced back to the instability of the power supply used to generate the field.

^aPresent address: PTB 4.41, 38116 Braunschweig, Germany

3.1 Introduction

In many areas of fundamental and applied science the sensitive detection of weak magnetic fields and small field fluctuations is of great importance. In the applied sector this concerns, for instance, non-destructive testing of materials [1], geomagnetic and archaeological prospecting [2], and the expanding field of biomagnetism [3]. In the realm of fundamental physics, strong demands on magnetometric sensitivity are placed by modern experiments looking for small violations of discrete symmetries in atoms and elementary particles. For instance, many experiments searching for time-reversal or parity violation rely on the precise monitoring and control of magnetic fields, with the sensitivity of the overall experiment directly related to the ultimate sensitivity and stability of the magnetic field detection. Picotesla or even femtotesla sensitivity requirements for averaging times of seconds to minutes are common in that field.

Our particular interest in this respect lies in the search for a permanent electric dipole moment (EDM) of the neutron. Such a moment violates both time reversal invariance and parity conservation. A finite sized EDM would seriously restrict theoretical models that extend beyond the standard model of particle physics [4]. Recently our team has joined a collaboration aiming at a new measurement of the permanent EDM of ultra-cold neutrons (UCN) to be produced from the UCN source under construction at Paul Scherrer Institute in Switzerland [5]. A neutron EDM spectrometer will be used, in which the neutron Larmor frequency will be measured by a Ramsey resonance method in UCN storage chambers exposed to a homogenous magnetic field. Each neutron chamber has two compartments in which the neutrons are exposed to a static electric field oriented parallel/antiparallel to the magnetic field. The signature of a finite EDM will be a change of the neutron Larmor frequency that is synchronous with the reversal of the relative orientations of the magnetic and electric fields. Magnetic field instabilities and inhomogeneities may mimic the existence of a finite neutron EDM. The control of such systematic effects is therefore a crucial feature of the EDM experiment. It is planned to use a set of optically pumped cesium vapor magnetometers (OPM), operated in the M_x configuration [6, 7] to perform that control.

Although OPMs pumped by spectral discharge lamps are suited for the task, we have opted for a system of laser pumped OPMs (LsOPM). It was shown previously that the replacement of the lamp in an OPM by a resonant laser can lead to an appreciable gain in magnetometric sensitivity [7, 8]. Laser pumping further offers the advantage that a single light source can be used for the simultaneous operation of several dozens of magnetometer heads. In that spirit we have designed and tested a LsOPM with a geometry compatible with the neutron EDM experiment. In this report we present the design and the performance of the Cs-LsOPM operated in a phase-stabilized mode and discuss a systematic effect specifically related to laser pumping.

3.2 The optically-pumped M_x magnetometer

Optically pumped magnetometers can reach extreme sensitivities of a few fT/ $\sqrt{\text{Hz}}$ [7], comparable to standard SQUID (superconducting quantum interference device) detectors. Recently a low field OPM with a sub-fT resolution was demonstrated [9]. The use of OPMs for the detection of biomagnetic signals was recently demonstrated by our group [10, 11].

As a general rule the optimum choice of the OPM depends on the specific demands (sensitivity, accuracy, stability, bandwidth, spatial resolution, dynamic range, etc.) of the magnetometric problem under consideration. In our particular case the main requirements are a highest possible sensitivity and stability for averaging times ranging from seconds up to 1000 seconds in a $2\mu\text{T}$ field together with geometrical constraints imposed by the neutron EDM experiment.

Optically pumped alkali vapor magnetometers rely on an optical radio-frequency (r.f.) resonance technique and are described, e.g., in [6]. When an alkali vapor is irradiated with circularly polarized light resonant with the D_1 absorption line (transition from the $nS_{1/2}$ ground state to the first $nP_{1/2}$ excited state), the sample is optically pumped and becomes spin polarized (magnetized) along the direction of the pumping light. While lamp pumped OPMs simultaneously pump all hyperfine transitions of the D_1 line, the use of a monomode laser in a LsOPM allows one to resolve the individual

hyperfine transitions provided that their Doppler width does not exceed the hyperfine splitting in both the excited and the ground states. This is, for example, the case for the D_1 transition of the alkali isotopes ^{133}Cs and ^{87}Rb . In that case it is advantageous to set the laser frequency to the $F = I + 1/2 \rightarrow F = I - 1/2$ transition, which allows one to optically pump the atoms into the two (non-absorbing) dark states $|nS_{1/2}; F; M_F = F, F-1\rangle$ using σ^+ polarized radiation. A magnetic field $\vec{B}_1(t)$ oscillating at the frequency ω_{rf} , which is resonant with the Zeeman splitting of the states, drives population out of the dark states into absorbing states, so that the magnetic resonance transition can be detected via a change of the optical transmission of the vapor. That is the very essence of optically detected magnetic resonance.

In the so-called M_x or 45° configuration the static magnetic field B_0 to be measured is oriented at 45° with respect to the laser beam, while the oscillating magnetic field $\vec{B}_1(t)$ is at right angles with respect to \vec{B}_0 (Fig. 3.1). In classical terms, the Larmor precession of the magnetization around \vec{B}_0 (at the frequency ω_L) is driven by the co-rotating component of the $\vec{B}_1(t)$ -field, which imposes a phase on the precessing spins. The projection of the precessing polarization onto the propagation direction of the light beam then leads to an oscillating magnetization component along that axis, and therefore to a periodic modulation of the optical absorption coefficient. The system behaves like a classical oscillator, in which the amplitude and the phase of the response (current from a photodiode detecting the transmitted laser intensity) depend in a resonant way on the frequency of the B_1 field. From the resonance condition $\omega_L = \omega_{\text{rf}}$ the Larmor frequency and hence the magnetic field can be inferred.

When the AC component of the detected optical signal is transmitted to the coils producing the $\vec{B}_1(t)$ field with a 90° phase shift and an appropriate gain, the system will spontaneously oscillate at the resonance frequency. In that self-oscillating configuration the OPM can in principle follow changes of the magnetic field instantaneously with a bandwidth limited by the Larmor frequency only [6].

Here we have used an alternative mode of operation, the so-called phase-stabilized mode. The in-phase amplitude X , the quadrature amplitude Y and the phase ϕ of the photocurrent with respect

to the oscillating magnetic field are given by

$$\text{a) } X(x) = -A \frac{x}{x^2 + 1 + S} \quad (3.1)$$

$$\text{b) } Y(x) = -A \frac{1}{x^2 + 1 + S} \quad (3.2)$$

$$\text{c) } \phi(x) = \arctan x, \quad (3.3)$$

where $x = (\nu_L - \nu_{\text{rf}})/\Delta\nu_{\text{HWHM}}$ is the detuning normalized to the (light-power dependent) half width at half maximum $\Delta\nu_{\text{HWHM}}$ of the resonance. S is a saturation parameter which describes the r.f. power broadening of the line. It is interesting to note that the width of the phase dependence, which is determined by the ratio of the $X(x)$ and $Y(x)$ signals, is independent of S , and hence immune to r.f. power broadening. The phase $\phi(x)$ changes from 0° to -180° as ν_{rf} is tuned over the Larmor frequency. Near resonance the phase is -90° and has a linear dependence on the detuning $\nu_L - \nu_{\text{rf}}$. $\phi(x)$ is detected by a phase sensitive amplifier (lock-in detector) whose phase output drives a voltage-controlled oscillator (VCO) which feeds the r.f. coils. The VCO signal, phase shifted by 90° , serves as a reference to the phase detector. This feedback loop thus actively locks the r.f. frequency to the Larmor frequency and the magnetometer tracks magnetic field changes in a phase coherent manner. That mode of operation is a modification of the self-oscillating magnetometer in the sense that the lock-in amplifier, the loop filter (PID), and the VCO represent the components of a tracking filter which shifts the detected signal by 90° and applies the filtered signal to the r.f. coils. The differences to the self-oscillating scheme are the following: the bandwidth of the phase-stabilized magnetometer is determined by the transmission function of the feedback loop, and the phase shift is always 90° independent of the Larmor frequency, while in the self-oscillating scheme the phase-shifter has a frequency dependence and is 90° only for a single Larmor frequency. Note that the tracking filter in a strict sense is not a phase-locked loop (PLL), since there is only one detectable frequency in the system, i.e., ν_{rf} . A detuning between the r.f. frequency and the Larmor frequency produces a static phase shift, while in a real PLL the detuning between the reference frequency and the frequency which is locked produces a time dependent phase shift.

3.3 Magnetometer hardware

The LsOPM for the n-EDM experiment consists of two parts: a sensor head containing no metallic parts except the r.f. coils, and a base station mounted in a portable 19" rack drawer, which contains the frequency stabilized laser and the photodetector. The laser light is carried from the base station to the sensor head by a 10 m long multimode fiber with a core diameter of $800\ \mu\text{m}$. The light transmitted through the cell is carried back to the detection unit by a similar fiber. The sensor head is designed to fit into a tube of 104 mm diameter, coaxial with the $2\ \mu\text{T}$ field, and has a total length of 242 mm. The main component of the sensor is an evacuated glass cell with a diameter of 7 cm containing a droplet of cesium in a sidearm connected to the main volume. A constriction in the sidearm minimizes the collision rate of vapor atoms with the cesium metal. The probability of spin depolarization due to wall collisions with the inner surface of the glass cell is strongly reduced by a thin layer of paraffin coating the cell walls. The cell was purchased from MAGTECH Ltd., St. Petersburg, Russia. A pair of circular coils (70 mm diameter separated by 52 mm) encloses the cell and produces the oscillating magnetic field $\vec{B}_1(t)$.

The light driving the magnetometer is produced by a tunable extended-cavity diode laser in Littman configuration (Sacher Lasertechnik GmbH, model TEC500). The laser frequency is actively locked to the 4-3 hyperfine component of the Cs D_1 transition ($\lambda = 894\ \text{nm}$) in an auxiliary cesium vapor cell by means of the dichroic atomic vapor laser lock (DAVLL) technique [12]. The stabilization to a Doppler-broadened resonance provides a continuous stable operation over several weeks and makes the setup rather insensitive to mechanical shocks.

At the sensor head the light from the fiber is collimated by a $f = 15\ \text{mm}$ lens and its polarization is made circular by a polarizing beamsplitter and a quarter-wave plate placed before the cesium cell. The light transmitted through the cell is focused into the return fiber, which guides it to a photodiode. The photocurrent is amplified by a low-noise transimpedance amplifier. Placing the laser, the electronics, and the photodiode far away from the sensor head eliminates magnetic interference generated by those components on the magnetometer (a photocurrent of $10\ \mu\text{A}$, e.g., produces a mag-

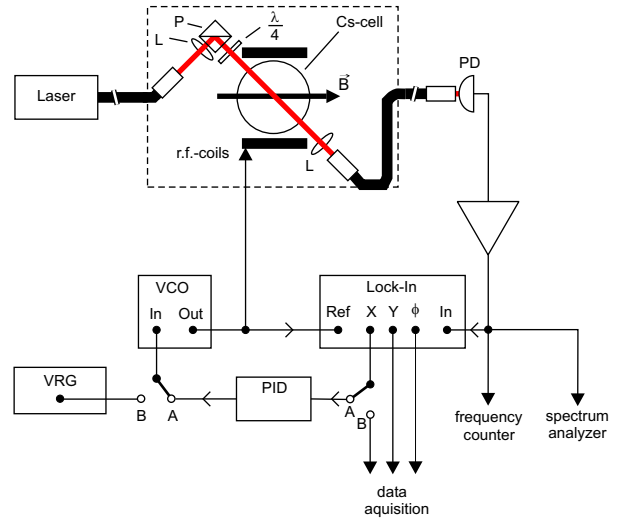


FIGURE 3.1: Schematic setup of the phase-stabilized magnetometer in the closed-loop (A) and the scanning (B) mode. The dashed box indicates the sensor head. L: lens, P: polarizing beamsplitter, $\lambda/4$: quarter-wave plate, PD: photodiode, VRG: voltage ramp generator, VCO: voltage-controlled oscillator, PID: feedback amplifier. The stabilization system of the laser frequency is not shown.

netic field of 200 pT at a distance of 1 cm). In the present setup the oscillating-field coil is fed via a twisted-pair conductor, which represents an effective antenna by which electromagnetic signals can be coupled into the magnetic shield. In a future stage of development it is planned to replace this electric lead by an opto-coupled system.

Multimode fibers were used for ease of light coupling. We found that a few loops of 3 cm radius of curvature in the fiber led to quasi-depolarization of the initially linearly polarized beam, thereby suppressing noise contributions from polarization fluctuations. A rigid fixation of the fibers was found necessary to reduce power fluctuations of the fiber transmission to a level of 4×10^{-5} in 1 Hz bandwidth.

The studies reported below were performed inside closed cylindrical shields consisting of three layers of Mumetal (size of the innermost shield: length 600 mm, diameter 300 mm) that reduces the influence of ambient magnetic field variations. For the measurement of the noise spectrum (Sec. 3.4.1) and the study of the magnetic field stability (Sec. 3.4.3) the shield was improved by three additional cylinders of Co-Netic mounted inside of the Mumetal shield (innermost diameter 230 mm). The

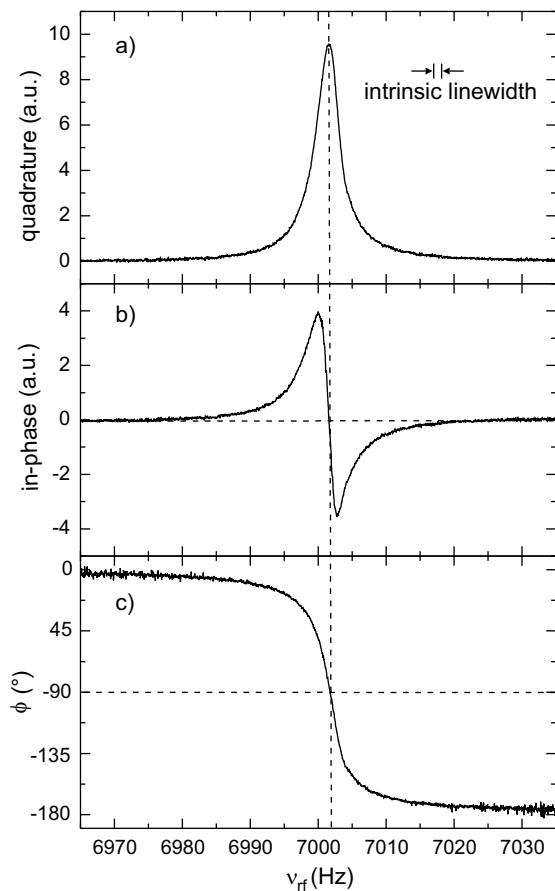


FIGURE 3.2: Magnetic resonance spectra obtained by scanning the frequency ν_{rf} of the oscillating field: a) quadrature component, b) in-phase component, c) phase between the oscillating field and the modulation of the transmitted power. The Larmor frequency ν_L is 7002.3 Hz, the power-broadened half linewidth is 2.2 Hz. The intrinsic half linewidth of 1.4 Hz is indicated.

longitudinal bias field of $2 \mu\text{T}$, corresponding to a Cs Larmor frequency of 7 kHz, is produced by a solenoid (length 600 mm, diameter 110 mm) inside the shield and the 8 mA current is provided by a specially designed stable current supply.

3.3.1 Resonance linewidth

The lineshapes of the magnetic resonance line are measured with the magnetometer operating in the open-loop mode (Fig. 3.1, mode B). A sinusoidally oscillating current of frequency ω_{rf} is supplied to the r.f. coils by a function generator, whose frequency is ramped across the Larmor frequency, and the output of the photodiode is demodulated by a lock-in

amplifier. Magnetic resonance lines were recorded for different B_1 amplitudes and different values of the pump light power. Typical resonance lines are shown in Fig. 3.2. The lineshapes were fitted by the function (3.3) to the experimental $\phi(\nu_{\text{rf}})$ curves, which allows one to infer the linewidth $\Delta\nu_{\text{HWHM}}$. We recall that the linewidth is not affected by r.f. power broadening, but that it is subject to broadening by the optical pumping process. The dependence of $\Delta\nu_{\text{HWHM}}$ on the laser intensity (Fig. 3.3) shows that the optical broadening has a nonlinear dependence on the light intensity. The minimum or intrinsic linewidth is determined by extrapolating $\Delta\nu_{\text{HWHM}}$ to zero light intensity.

For a $J = 1/2$ two-level system theory predicts a linear dependence of the linewidth on the pumping light intensity, as long as stimulated emission processes from the excited state can be neglected. However, the magnetic resonance spectrum in the $F = 4$ manifold of the Cs ground state is a superposition of eight degenerate resonances corresponding to all allowed $\Delta M = \pm 1$ transitions between adjacent Zeeman levels. The coupling of the σ^+ polarized light to the different sublevels depends on their magnetic quantum number M_F and is given by the corresponding electric dipole transition matrix elements. As a consequence each of the eight resonances broadens at a different rate. The observed linewidth results from the superposition of those individual lines weighted by the population differences of the levels coupled by the r.f. transition and the corresponding magnetic dipole transition rates. The observed nonlinear dependence of the width on the light intensity follows from the nonlinear way in which those population differences and hence the relative weights are changed by the optical pumping process.

We have calculated the lineshapes of the magnetic resonance lines by numerically solving the Liouville equation for the ground state density matrix. Interactions with the optical field as well as the static and oscillating magnetic fields were taken into account in the rotating wave approximation. We further assumed an isotropic relaxation of the spin coherence at a rate given by the experimentally determined intrinsic linewidth of Fig. 3.3. The solid curve in that figure represents the linewidths inferred from the calculated lineshapes. The calculations used as a variable an optical pumping rate (proportional to the light power intensity) and the

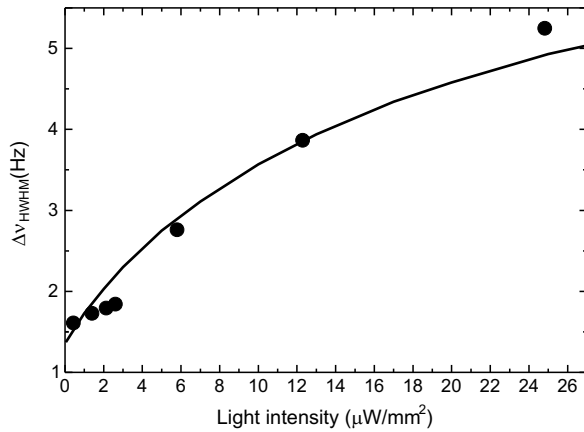


FIGURE 3.3: Resonance HWHM linewidth as a function of the light intensity delivered to the cell. The power of the laser beam is given by $I_L \cdot 2.8 \text{ mm}^2$. The dots represent the widths obtained from the phase signal of the lock-in amplifier with very low r.f. power. The extrapolated intrinsic linewidth is 1.4(1) Hz. The solid line is a one-parameter fit of a numerical calculation to the data (see text). The size of the symbols represents the vertical error bars.

only parameter used to fit the calculation to the experimental data was the proportionality constant between the laser intensity and that pump rate.

The intrinsic linewidth, i.e., the linewidth for vanishing optical and r.f. power, is determined by relaxation due to spin exchange Cs-Cs collisions, Cs-wall collisions, and collisions of the atoms with the Cs droplet in the reservoir sidearm. The latter contribution depends on the ratio of the cross section of the constriction in the sidearm and the inner surface of the spherical cell. With an inner sidearm diameter of 0.5 mm that contribution to the HWHM linewidth can be estimated to be on the order of $\Delta\nu = 1 \text{ Hz}$. The contribution from spin exchange processes at room temperature to the linewidth can be estimated using the cross section reported in [13] to be on the order of 3 Hz, which is larger than the measured width. A possible explanation for this discrepancy is the adsorption of Cs atoms in the paraffin coating [14], which may lead to an effective vapor pressure in the cell below its thermal equilibrium value.

3.3.2 Magnetometer mode

The actual magnetometry is performed in the phase-stabilized mode (Fig. 3.1, mode A) as de-

scribed above. The photodiode signal is demodulated by a lock-in amplifier (Stanford Research Systems, model SR830) locked to the driving r.f. frequency, produced by a voltage-controlled oscillator (VCO). The time constant of the lock-in amplifier was set to $\tau = 30 \mu\text{s}$, which corresponds to a bandwidth of 2.6 kHz with a -24 dB/octave filter roll-off. Either the phase (adjusted to be 0° on resonance) or the dispersive in-phase signal of the lock-in amplifier can be used to control the VCO, and hence to lock its frequency to the center of the magnetic resonance. Compared to the in-phase signal the phase signal of the lock-in amplifier has the advantage that the resonance linewidth is not affected by r.f. power broadening. However, the bandwidth of the phase output of the digital lock-in amplifier used was limited to 200 Hz by its relatively slow update rate. For the neutron EDM experiment the magnetometer has to be operated with the highest possible bandwidth. We therefore chose the in-phase signal for the following studies. That signal drives the VCO via a feedback amplifier (integrating and differentiating), which closes the feedback loop locking the radio frequency to the Larmor frequency.

3.4 Performance of the magnetometer

3.4.1 Magnetometric sensitivity

We characterize the sensitivity of the magnetometer in terms of the noise equivalent magnetic flux density (NEM), which is the flux density change δB equivalent to the total noise of the detector signal

$$\delta B^2 = \delta B_{\text{int}}^2 + \delta B_{\text{ext}}^2, \quad (3.4)$$

with both internal and external contributions: δB_{int} describes limitations due to noise sources inherent to the magnetometer proper, while δB_{ext} represents magnetic noise due to external field fluctuations. The larger of the two contributions determines the smallest flux density change that the magnetometer can detect. In general the internal NEM δB_{int} may have several contributions, which may be expressed as

$$\delta B_{\text{int}}^2 = \left(\frac{1}{\gamma} \times \frac{\Delta\nu_{\text{HWHM}}}{S/N_{\text{SN}}} \right)^2 + \sum_i \left(\frac{1}{\gamma} \times \frac{\Delta\nu_{\text{HWHM}}}{S/N_{\text{OPM}}^{(i)}} \right)^2, \quad (3.5)$$

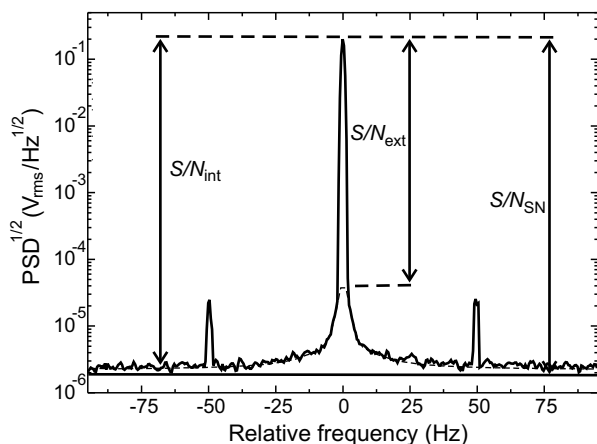


FIGURE 3.4: Square root of the power spectral density (PSD) of the photodiode output frequency relative to the Larmor frequency of $\nu_0 = 6998$ Hz (averaged 20 times). The straight line indicates the shot noise limit N_{SN} . The signal-to-noise ratio S/N_{int} is approximately 66000. The sidebands are due to imperfectly shielded magnetic field components oscillating at the 50-Hz power line frequency. The signal-to-noise ratio S/N_{ext} due to external field fluctuations is approximately 4600. All measurements were performed in a 1 Hz bandwidth.

where S is the magnetometer signal, $N_{OPM}^{(i)}$ are the noise levels of the different processes contributing to δB_{int} , and N_{SN} the fundamental shot noise limit of the OPM signal. γ is approximately 3.5 Hz/nT for ^{133}Cs and $\Delta\nu_{HWHM}$ is the half width of the resonance (cf. Sec. 3.4.2).

The magnetic field noise δB_{ext} can also be parameterized in the form of Eq. (3.5) with an equivalent signal noise N_{ext} so that Eq. (3.4) can be expressed as

$$\delta B = \frac{1}{\gamma} \times \frac{\Delta\nu_{HWHM}}{S/N}, \quad (3.6)$$

with $N^2 = N_{ext}^2 + N_{SN}^2 + \sum_i (N_{OPM}^{(i)})^2$.

In a strict sense Eqs. (3.5) and (3.6) are valid for the open loop operation of the magnetometer. The parameters γ and $\Delta\nu_{HWHM}$ do not depend on the mode of operation, whereas S/N may very well be affected by feedback.

Experimentally the spectral dependence of the noise contributions N_α are determined from a Fourier analysis of the photodiode signal (using a Stanford Research SR760 FFT spectrum analyzer), when the magnetometer is operated in the phase-stabilized mode under optimized parameter condi-

tions. Each noise figure N_α is defined as the square root of the integrated (frequency dependent) power spectral density ρ_α^2 of the corresponding signal fluctuations

$$N_\alpha = \left(\int_0^{f_{bw}} \rho_\alpha^2 df \right)^{1/2}, \quad (3.7)$$

where f_{bw} is the measurement bandwidth. If the noise is white or if the bandwidth is much smaller than the width of typical spectral features in the power spectrum the noise level at a given frequency f is given by

$$N_\alpha = \rho_\alpha \sqrt{f_{bw}} = \rho_\alpha / \sqrt{2\tau}, \quad (3.8)$$

where τ is the integration time used for calculating the Allan standard deviation introduced below. Figure 3.4 shows a typical Fourier spectrum of the OPM signal. The prominent central feature represents the Larmor oscillation of the photocurrent at 7 kHz during the phase-stabilized operation of the OPM. It is the signal-to-noise ratio at the Larmor frequency which determines the NEM of the magnetometer.

In the following we discuss the influence of different noise sources on the photodiode spectrum as well as on the magnetometer sensitivity. The magnetometer noise is affected by magnetic field fluctuations via frequency mixing. A mono-frequent field fluctuation at frequency ω and modulation index ξ will yield an effective Larmor frequency $\omega_L(1 + \xi \cos \omega t)$, which produces sidebands at $\omega_L \pm n\omega$ where n is an integer number. The two strong sidebands in Fig. 3.4 represent the first order ($n=1$) sidebands due to magnetic field perturbations oscillating at the line frequency of 50 Hz. A continuous distribution of low frequency field fluctuations leads – using the same arguments – to the 20 Hz broad pedestal under the Larmor peak, which explains the feature seen in Fig. 3.4. We make a best guess of the amplitude of that pedestal by fitting a Lorentzian to its wings. The fitted amplitude represents N_{ext} from which we extract $\delta B_{ext} = 210$ fT in a 1 Hz bandwidth.

The fundamental limit of the magnetometric sensitivity is determined by the white shot noise

$$N_{SN} = \sqrt{2eI_{DC}f_{bw}} \quad (3.9)$$

of the DC component of the photocurrent, I_{DC} . N_{SN} defines the ultimate shot noise limited NEM

δB_{SN} . About 100 Hz away from the Larmor frequency the measured constant noise floor exceeds the calculated shot noise level (N_{SN}) by a factor of 1.5. This originates from additional noise sources related, e.g., to technical laser power noise. It is reasonable to consider this noise floor to be the same under the pedestal and in particular at the Larmor frequency, thus the signal-to-(intrinsic)noise ratio S/N_{int} is 66000 and yields a NEM $\delta B_{\text{int}} = 15$ fT in a 1 Hz bandwidth. Under optimized conditions the photocurrent is $5 \mu\text{A}$, which would yield a shot noise limited NEM of $\delta B_{\text{SN}} = 10$ fT in a bandwidth of 1 Hz.

Next we address the contribution of laser power fluctuations to the magnetometer performance. We distinguish three possible contributions. a) Power fluctuations at the Larmor frequency contribute to the noise level under the Larmor peak in Fig. 3.4. As mentioned above they contain contributions from shot noise and excess technical laser power noise. b) Any low-frequency monochromatic power fluctuation will yield sidebands near the Larmor peak via amplitude modulation of the magnetometer signal. The same frequency mixing mechanism transforms a continuous low frequency spectrum of power fluctuations into a symmetric pedestal underlying the Larmor peak. However, it can be shown, e.g., by a numerical simulation [15], that this pedestal does not contribute to the noise of the phase signal (for any detuning) nor to the noise of the (resonant) in-phase signal (Fig. 3.2). Low frequency power fluctuations are therefore of no concern if any of the two signals is used to operate the magnetometer. c) Light shift fluctuations are an additional source of noise. Any fluctuations of the parameters causing a light shift (laser power and/or laser frequency detuning) will produce magnetic field equivalent noise. We will show later that for a 1 Hz detection bandwidth this effect gives a negligible contribution to the Fourier spectrum.

As the internal noise level δB_{int} is much smaller than the external field fluctuations δB_{ext} the magnetometer is well suited to measure the characteristics of such field fluctuations (cf. Sec. 3.4.3) and/or to compensate them using an active feedback loop. The accuracy of such measurements or the performance of such a stabilization is ultimately limited by the internal noise of the magnetometer, which under ideal conditions can reach the shot noise limit.

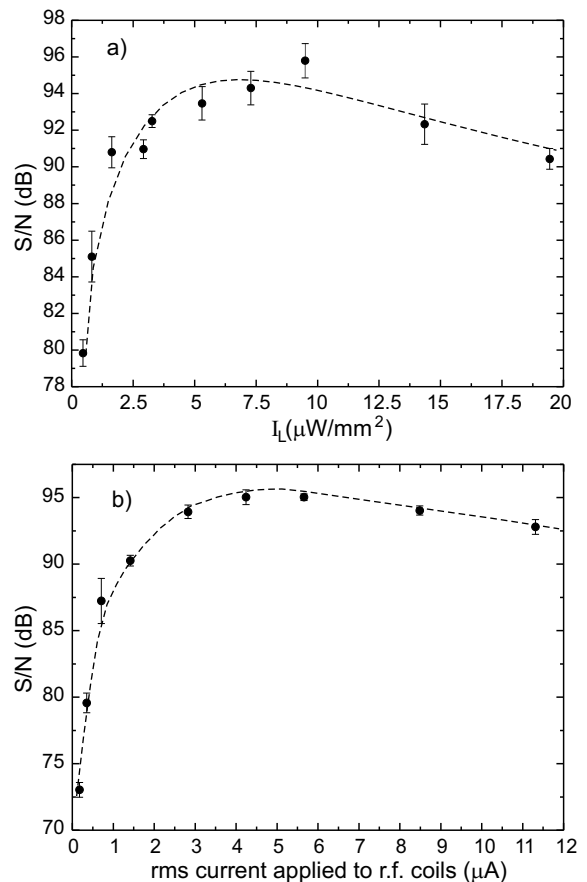


FIGURE 3.5: Dependence of the experimental signal-to-noise ratio (measured in a 1 Hz bandwidth) on the light intensity and the current applied to the r.f. coils. The noise was measured 70 Hz away from the carrier. The r.f. current in a) was $8 \mu\text{A}_{\text{pp}}$, the light intensity in b) was $7 \mu\text{W}/\text{mm}^2$. The dashed lines are drawn to guide the eyes. These are typical recordings used to optimize the system parameters.

3.4.2 Magnetometer optimization and response bandwidth

According to Eq. (3.5) the sensitivity of the magnetometer depends on the resonance linewidth $\Delta\nu_{\text{HWHM}}$ and on the signal-to-noise ratio. For given properties of the sensor medium (cesium vapor pressure and cell size) these two properties depend on the two main system parameters, viz., the laser intensity I_L (or power P_L) and the amplitude B_1 of the r.f. field. For the application in the neutron EDM experiment the sensor size and vapor pressure are dictated by the experimental constraints (fixed geometry and operation at room temperature), so

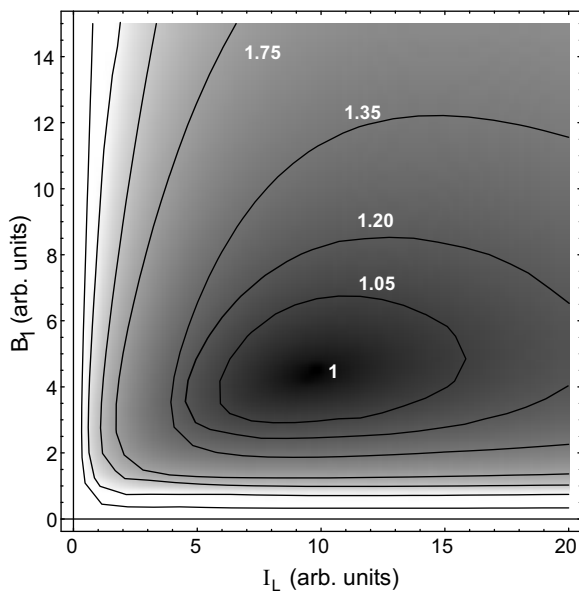


FIGURE 3.6: Density plot (in arbitrary units) of the calculated NEM δB_{SN} , in dependence on the laser intensity I_L and the r.f. amplitude B_1 .

that the experimental optimization of the magnetometric sensitivity is performed in the (I_L, B_1) space by an iterative procedure. Fig. 3.5 shows examples of signal-to-noise ratio recordings during such an iteration. The optimum operating point was found for a laser intensity I_L of $9 \mu\text{W}/\text{mm}^2$ and a r.f. field amplitude B_1 of 2.7 nT. The resonance linewidth under optimum conditions is $\Delta\nu_{\text{HWHM}} = 3.4(1)$ Hz, which exceeds the intrinsic linewidth by a factor of 2.4.

In order to investigate the dependence of the NEM on the two optimization parameters we have calculated that dependence using the density matrix formalism by assuming that the signal noise is determined by the shot noise of the photocurrent. The result is shown in Fig. 3.6 as a density plot. One recognizes a broad global minimum which is rather insensitive to the parameter values as it rises only by 5% when the optimum light and r.f. power are varied by 50%.

The bandwidth of the magnetometer, i.e., its temporal response to field changes was measured in the following way: a sinusoidal modulation of the static magnetic field with an amplitude of 5 nT was applied by an additional single wire loop (110 mm diameter) wound around the Cs cell. The response of the magnetometer to that perturbation was measured directly on the VCO input voltage in the

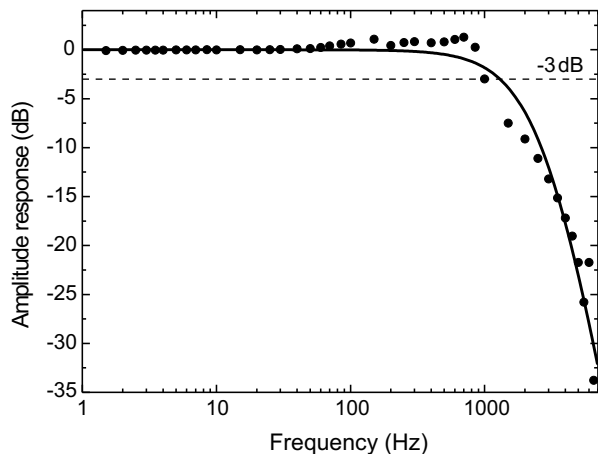


FIGURE 3.7: Frequency dependence of the magnetometer response to a small amplitude sinusoidal modulation of the static field B_0 (circles). The solid line indicates the amplitude response of a 4th-order low-pass filter (-24 dB/octave roll-off).

phase-stabilized mode. The result is shown in Fig. 3.7. The overall magnetometer response follows the behavior of a low-pass filter (-24 dB/octave roll-off) with a -3 dB point at approximately 1 kHz. The lock-in time constant was $30 \mu\text{s}$ which corresponds to a bandwidth of 2.6 kHz. The difference is due to additional filters in the feedback loop.

3.4.3 Application: Field fluctuations in a magnetic shield

External field fluctuations are the dominant contribution to the noise of the LsOPM when it is operated in the six-layer magnetic shield. We have used the magnetometer to study the temporal characteristics of the residual field variations. The Allan standard deviation [16] is the most convenient measure for that characterization. With respect to the experimental specifications of the neutron EDM experiment our particular interest is the field stability for integration times in the range of 100 to 1000 s. For that purpose we recorded the Larmor frequency in multiple time series of several hours with a sampling rate of 0.1 s by feeding the photodiode signal, filtered by a resonant amplifier (band-pass of 200 Hz width centered at 7 kHz), to a frequency counter (Stanford Research Systems, model SR620). From each time series the Allan standard deviation of the flux density inside the shield was calculated. A typical result is shown in Fig. 3.8 with both ab-

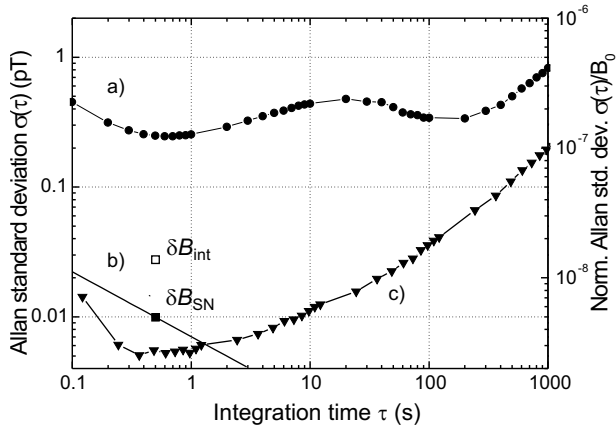


FIGURE 3.8: a) Allan standard deviation δB_{ext} of the magnetic flux density inside the magnetic shield (●). b) NEM δB_{int} (□) limited by laser power fluctuations; extrapolated NEM δB_{SN} (■) for shot noise limited operation. The slope represents Eq. (3.8) assuming a white noise behavior. c) Measured contributions to δB_{int} from light power fluctuations (▼) with present setup. Solid lines in a) and c) are drawn to guide the eye. The dwell time of the frequency counter was 100 ms.

solute and relative scales. For integration times below one second the observed fluctuations (curve a) decrease as $\tau^{-1/2}$, indicating the presence of white field-amplitude noise. It is characterized by a spectral density of $245 \text{ fT}/\sqrt{\text{Hz}}$. Although the Allan standard deviation represents a different property than the Fourier noise spectrum it is worthwhile to note that the latter value is comparable with the NEM $\delta B_{\text{ext}} = 210 \text{ fT}$ of the pedestal in Fig. 3.4 discussed above. The field fluctuations reach a minimum value of about 240 fT for an integration time of 0.7 s .

The central region of the Allan plot (Fig. 3.8a) shows a bump for integration times of 1–100 seconds. It is probably due to fluctuations of the 8 mA current producing the $2 \mu\text{T}$ bias field. A magnetic field fluctuation of 200 fT corresponds to a relative current stability of 10^{-7} , i.e., to current fluctuations of 800 pA . In an auxiliary experiment we measured the current fluctuations ΔI by recording voltage fluctuations over a series resistor for several hours. We found relative fluctuations of $\Delta I/I$ in the corresponding Allan plot of the same order of magnitude as the $\Delta B/B$ fluctuations. It is thus reasonable to assume that the origin of the plateau in Fig. 3.8a is due to current fluctuations of the power supply.

The measurement of the magnetic field during

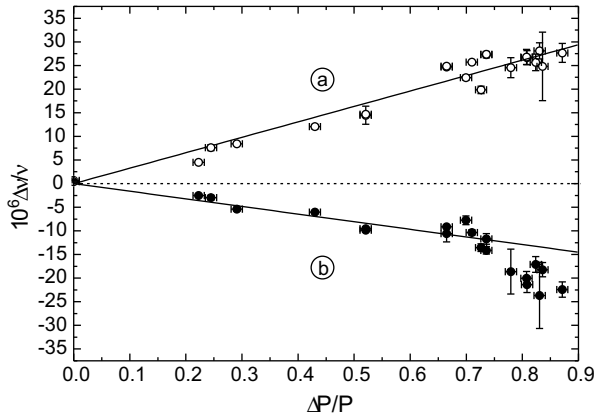


FIGURE 3.9: Relative light shift of the Larmor frequency as a function of the relative modulation amplitude ΔP of the laser power P . Curves (a) and (b) represent measurements with light of opposite circular polarization.

several days shows fluctuations with a period of one day and an amplitude of about 1 Hz , superposed by additional uncorrelated drifts. The periodic fluctuations are probably due to changes of the solenoid geometry induced by temperature fluctuations. The Allan standard deviations for integration times exceeding 200 s are thus determined by temperature fluctuations and drifts of the laboratory fields, which are not completely suppressed by the shield.

3.4.4 Frequency noise due to light power fluctuations

It is well-known that a near-resonant circularly polarized light field shifts the Zeeman levels in the same way as a static magnetic field oriented along the light beam. The light shift has contributions from the AC Stark shift and coherence shift due to virtual and real transitions [17]. The AC Stark shift, and hence the equivalent magnetic field B_{LS} is proportional to the light intensity I_L and has a dispersive (Lorentzian) dependence on the detuning of the laser frequency from the center of the optical absorption line. It is therefore expected to vanish at the (optical) line center. In our experiment the laser frequency is locked to the center of a Doppler-broadened hyperfine component. However, that frequency does not coincide with the frequency for which the light shift vanishes, because of finite light shift contributions from the adjacent hyperfine component. While the two hyperfine components

are well separated in the optical absorption spectra, their corresponding light shift spectra overlap because of the broad wings of their dispersive line-shapes.

In order to measure the light shift effect we periodically changed the light power between $P + \Delta P/2$ and $P - \Delta P/2$ and recorded the corresponding Larmor frequencies. False effects from drifts of the external magnetic field were suppressed by recording data over several modulation periods. For each modulation amplitude ΔP the Larmor frequency was measured with both σ^+ and σ^- polarizations by rotating the quarter-wave plate by means of a mechanical remote control from outside the shield. The induced changes of the magnetometer readings for both polarizations are shown in Fig. 3.9.

As anticipated, the shift of the Larmor frequency is proportional to the modulation amplitude of the light power and changes sign upon reversing the light helicity. However, it can be seen that the slope of the light shift depends on the helicity. This asymmetry is the result of contributions from three distinct effects, which we discuss only qualitatively here.

(1) The light shift due to virtual transitions (AC Stark shift), which is proportional to the helicity of the light and thus leads to a symmetric contribution to the curves of Fig. 3.9 (equal in magnitude, but opposite in sign); (2) the light shift due to real transitions (coherence shift)[17], whose origin is a change of the effective g -factor of the Cs atom due to the fact that with increasing laser power the atom spends an increasing fraction of its time in the excited state with a 3 times smaller g_F -factor of opposite sign than that of the ground state; (3) a possible power dependent change of the capacity of the photodiode and a subsequent power dependent phase shift of the photocurrent. The latter two effects yield shifts which have the same sign for both light polarizations, so that the combined contribution of the three effects may explain the different magnitudes of the slopes. A quantitative study of those effects is underway.

Using curve (a) as a worst-case estimate for the fluctuations of the Larmor frequency due to light power fluctuations we estimated, based on measured power fluctuations, the resulting magnetic field fluctuations. The results are shown as triangles in Fig. 3.8. Light shift fluctuations of the magnetometer readings are thus one to two orders of

magnitude smaller than residual field fluctuations in the present shield. The light shift noise can of course be further suppressed by adjusting the laser frequency to the zero light shift frequency point or better by actively stabilizing it to that point or by actively stabilizing the laser power.

3.5 Summary and conclusion

We have described the design and performance of a phase-stabilized cesium vapor magnetometer. The magnetometer has an intrinsic NEM of 15 fT, defined as the Allan standard deviation for a bandwidth of 1 Hz. If the excess white noise floor can be reduced to the shot-noise level, the LsOPM should reach a NEM of 10 fT for a 1 Hz bandwidth. The bandwidth of the phase-stabilized LsOPM is 1 kHz. We have used the LsOPM to measure field fluctuations in a six-layer magnetic shield for integration times between 0.1 and 1000 seconds, whose lowest values were found to be on the order of 200–300 fT. Light shift fluctuations, against which no particular precautions were taken, are one to two orders of magnitude smaller than the residual field fluctuations in the shield.

The LsOPM described here compares very favorably with state-of-the-art lamp-pumped magnetometers. Details on that comparison will be published elsewhere. It will be a valuable tool for fundamental physics experiments. The LsOPM presented above meets the requirements of the neutron-EDM experiment on the relevant time scales in the range of 100 to 1000 seconds.

ACKNOWLEDGMENTS We are indebted to E. B. Alexandrov and A. S. Pazgalev for numerous fruitful discussions. We acknowledge financial support from Schweizerischer Nationalfonds, Deutsche Forschungsgemeinschaft, INTAS, and Paul Scherrer Institute (PSI).

References

- [1] Y. Zhang, Y. Tavrín, H. J. Krause, H. Bousack, A. I. Braginski AI, U. Kalberkamp, U. Matzander, M. Burghoff, and L. Trahms. *Applications of high-temperature SQUIDS*. Applied Superconductivity **3**(7–10), 367–381 (1995).

- [2] H. Becker. *From nanotesla to picotesla - a new window for magnetic prospecting in archaeology*. *Archaeological Prospection* **2**, 217–228 (1995).
- [3] W. Andrä and H. Nowak (eds.). *Magnetism in Medicine*. Wiley-VCH Berlin (1998).
- [4] I. S. Altarev, Y. V. Borisov, N. V. Borovikova, A. I. Egorov, S. N. Ivanov, E. A. Kolomensky, M. S. Lasakov, V. M. Lobashev, V. A. Nazarenko, A. N. Pirozhkov, A. P. Serebrov, Y. V. Sobolev, and E. V. Shulgina. *Search for the neutron electric dipole moment*. *Physics of Atomic Nuclei* **59**(7), 1152–1170 (1996).
- [5] URL <http://ucn.web.psi.ch/> (2005).
- [6] A. L. Bloom. *Principles of operation of the rubidium vapor magnetometer*. *Appl. Opt.* **1**(1), 61–68 (1962).
- [7] E. B. Aleksandrov, M. V. Balabas, A. K. Verhovskii, A. E. Ivanov, N. N. Yakobson, V. L. Velichanskii, and N. V. Senkov. *Laser pumping in the scheme of an M_x -magnetometer*. *Opt. Spectrosc.* **78**(2), 325–332 (1995).
- [8] E. B. Aleksandrov. *Sov. Phys. Tech. Phys.* **35**, 371 (1990).
- [9] I. K. Kominis, T. W. Kornack, J. C. Allred, and M. V. Romalis. *A subfemtotesla multi-channel atomic magnetometer*. *Nature* **422** (6932), 596–599 (2003).
- [10] G. Bison, R. Wynands, and A. Weis. *A laser-pumped magnetometer for the mapping of human cardiomagnetic fields*. *Appl. Phys. B* **76** (3), 325–328 (2003).
- [11] G. Bison, R. Wynands, and A. Weis. *Dynamical mapping of the human cardiomagnetic field with a room-temperature, laser-optical sensor*. *Opt. Expr.* **11**(8), 904–909 (2003).
- [12] V. V. Yashchuk, D. Budker, and J. R. Davis. *Laser frequency stabilization using linear magneto-optics*. *Rev. Sci. Instrum.* **71**(2), 341–346 (2000).
- [13] N. Beverini, P. Minguzzi, and F. Strumia. *Foreign-gas-induced cesium hyperfine relaxation*. *Phys. Rev. A* **4**(2), 550–555 (1971).
- [14] E. B. Alexandrov, M. V. Balabas, D. Budker, D. English, D. F. Kimball, C.-H. Li, and V. V. Yashchuk. *Light-induced desorption of alkali-metal atoms from paraffin coating*. *Phys. Rev. A* **66**, 042903 (2002).
- [15] G. Bison et al. To be published.
- [16] J.A. Barnes, A. R. Chi, L.S. Cutler, D.J. Healey, D.B. Leeson, T.E. McGunigal, J.A. Mullen, Jr., W.L. Smith, R.L. Sydnor, R.F.C. Vessot, and G.M.R. Winkler. *Characterization of frequency stability*. *IEEE Trans. Instrum. Meas.* **20**, 105–120 (1971).
- [17] C. Cohen-Tannoudji. *Théorie quantique du cycle de pompage optique*. *Ann. Phys.* **7**(7–8), 423 (1962).

Chapter 4

Comparison of discharge lamp and laser pumped cesium magnetometers

S. Groeger^{1,2}, A. S. Pazgalev^{1,3}, and A. Weis¹

¹*Département de Physique, Université de Fribourg, Chemin du Musée 3, 1700 Fribourg, Switzerland*

²*Paul Scherrer Institute, 5232 Villigen PSI, Switzerland*

³*Ioffe Physical Technical Institute, Russ. Acad. Sc., St. Petersburg, 194021, Russia*

Published in *Appl. Phys. B* **80**(6), 645–654 (2005).

ABSTRACT: We have performed a comparison of laser (LsOPM) and lamp (LpOPM) pumped cesium vapor magnetometers. Although the LsOPM operated 50% above its shot-noise limit we found an intrinsic sensitivity of $15 \text{ fT}/\sqrt{\text{Hz}}$ and $25 \text{ fT}/\sqrt{\text{Hz}}$ for the LsOPM and LpOPM respectively. Two modes of operation, viz., the phase-stabilized and the self-oscillating mode were investigated and found to yield a similar performance. We have compared the performance of the LsOPM and the LpOPM directly by simultaneous measurements of field fluctuations of a $2 \mu\text{T}$ magnetic field inside a multilayer magnetic shield and have used one of the magnetometers for an active field stabilization. In the stabilized mode we found a gradient instability of 25 fT within an integration time of 100 s , which represents an upper limit of the long-term stability of the magnetometers. Our research is motivated by the need for an improved control of magnetic fields and gradients in a planned neutron electric-dipole experiment.

4.1 Introduction

The precise measurement and control of magnetic fields and field fluctuations is of crucial importance in many fundamental physics experiments. The suppression of systematic uncertainties in experiments searching for permanent electric dipole moments (EDMs) in atoms and neutrons is one prominent example. New generations of EDM experiments with ultracold neutrons (UCNs) aim at putting more stringent limits on (or even observing) an EDM by the use of higher UCN flux and larger storage volumes, which improve the statistical sensitivity. The increased sensitivity also puts more stringent constraints on systematic effects and calls, in particular, for a better control of the stability of the magnetic field and its gradients. Although magnetometers based on superconducting quantum interference devices (SQUIDs) are the most sensitive magnetometers available to date they are of limited interest for monitoring magnetic fields in large volumes. Moreover, SQUIDs do not measure absolute field values.

Two distinct magnetometric techniques were used in past EDM experiments. In the ILL experiment [1], which has produced the presently lowest upper bound on the neutron EDM, a vapor of ^{199}Hg atoms filled into the ultracold neutron storage chamber (20 liter) served as “cohabitating” magnetometer. The PNPI experiment [2], on the other side, used a set of two self-oscillating cesium vapor magnetometers placed above and below the storage chamber for monitoring the field in the chamber. Both techniques have pros and cons. Co-magnetometers yield only a volume-averaged field value, which yields no information on field gradients and their fluctuations. External magnetometers, on the other hand, do not measure the field in the volume of interest directly, but allow – if used in sufficient number – to access field distributions, thereby permitting the active control of specific multipole moments of the field. Borisov et al. have proposed a large volume (external) magnetometer based on nuclear spin precession in ^3He [3]. That device uses a double pulse Ramsey resonance technique, which besides its lack of spatial resolution also suffers from a lack of temporal resolution.

The PNPI experiment used two conventional state-of-the-art discharge lamp pumped self-oscillating cesium vapor magnetometers (OPM) [2].

Such types of magnetometers - developed since the 1950's - have a shot-noise limited performance and large bandwidths. The high spatial and temporal resolution of optically pumped alkali magnetometers thus make such devices interesting alternatives for the continuous monitoring of fields, gradients, and fluctuations thereof. The use of alkali OPMs for the field control in larger volumes calls for a substantially larger number of sensor heads, which suffers from the fact that a single discharge lamp can only drive a limited number of sensors. The steady development in the past decades of narrow-band semiconductor diode lasers makes such light sources attractive alternatives to discharge lamps. Owing to the high spectral density of its radiation a single diode laser of moderate power (a few mW) can be used to drive dozens of magnetometer heads.

Having a multichannel external magnetometer approach for a planned neutron EDM experiment in mind we have performed a comparative study of state-of-the-art discharge lamp pumped magnetometers (LpOPM) and laser pumped magnetometers (LsOPM) using similar room temperature sensor cells (7 cm and 6 cm diameter respectively) and identical electronics. We discuss the principle of operation and details of their practical realization. The devices were operated in two distinct modes, viz., the self-oscillating mode and the phase-stabilized mode. Details of the development and performance of the LsOPM will be published elsewhere [4]. We have determined the intrinsic sensitivities of the magnetometers and present measurements of the fluctuations of a $2\mu\text{T}$ field recorded simultaneously by the LsOPM and the LpOPM in a multilayer magnetic shield. The LpOPM reached its ultimate shot-noise limited performance while the LsOPM showed a superior intrinsic sensitivity, although its performance still lies 50% above its fundamental shot-noise limit.

4.2 Optically pumped magnetometers

4.2.1 General principle

An OPM measures the Larmor precession frequency ω_L of a vapor sample of spin polarized atoms in an external magnetic field B_0 . In small magnetic fields

$$\nu_L = \frac{\omega_L}{2\pi} = \frac{\gamma_A}{2\pi} B_0, \quad (4.1)$$

and the field measurement reduces to a frequency measurement. In Eq. 4.1 the subscript of γ_A refers to the total angular momentum of the precessing atomic state. Although OPMs based on nuclear spin polarization were demonstrated in the past [1, 3, 5, 6] we restrict the present discussion to alkali vapors in which the precessing levels are one or both of the hyperfine ground states with total angular momentum $F = I \pm 1/2$, where I is the nuclear spin. Magnetic resonance is used to measure the precession frequency by inducing resonant spin flips by a weak magnetic field B_1 oriented at right angles with respect to B_0 and oscillating at the frequency ω_{rf} . Although for the magnetometer discussed here ω_{rf} lies in the audio range of frequencies the index “rf” (radio-frequency) is used to comply with common notation.

Optical pumping with a resonant circularly polarized light beam creates spin polarization in the medium (room temperature alkali atom vapor contained in a glass cell) and hence an associated net bulk magnetization. It has been realized for many years that the pumping process is most efficient for D_1 resonance light driving the transition $|nS_{1/2}\rangle \rightarrow |nP_{1/2}\rangle$, although magnetometers can also be realized using D_2 ($|nS_{1/2}\rangle \rightarrow |nP_{3/2}\rangle$) light. In general the optically pumped medium becomes transparent with respect to the pumping light, except for the spectrally resolved closed $|nS_{1/2} F\rangle \rightarrow |nP_{3/2}, F+1\rangle$ transition [7], in which case the absorption of the pumped medium increases. The fact that the optical properties of the medium depend on its spin polarization is used to detect the magnetic resonance transition by monitoring either the power or the polarization of the transmitted or scattered light beam. The technique is known as optically detected magnetic resonance (ODMR).

In the present study we have used a particular realization of the ODMR technique, the so-called M_x method, in which B_0 is oriented at 45° with respect to the direction of propagation (\hat{k}) of the circularly polarized light beam. The particular feature of that technique is that the transmitted light intensity is modulated at the frequency ω_{rf} of the oscillating field, when ω_{rf} is tuned close to ω_L . The amplitude of the modulation depends as $\sin 2\theta$ with $\cos \theta = \widehat{B}_0 \cdot \widehat{k}$. The amplitude and phase of the modulation depend on ω_{rf} as a classical Lorentz oscillator with a resonance frequency ω_L . On resonance the phase shift between the oscillating B_1 -field and

the transmitted light modulation is 90° and for a small detuning $\delta\omega = \omega_{\text{rf}} - \omega_L$ the phase shift varies linearly with $\delta\omega$. The width of the resonance(s) are determined by the transverse relaxation rate of the spin polarization, which is limited by several effects. In atom-atom collisions only the sum of the angular momenta of the collision partners is preserved but spin-exchange processes can change the individual polarizations. The rate of spin exchange depolarization is proportional to the collision rate, i.e., to the vapor density, the spin-exchange cross-section, and the relative velocities of the collision partners. The dominant depolarization mechanism is due to collisions of the atoms with the cell walls and the depolarization rate depends on the adsorption time of the atoms on the walls and on the wall collision rate. This process can be suppressed by either preventing the atoms from reaching the walls through the addition of an inert buffer gas or by reducing the sticking time on the walls by a suitable coating of the wall surfaces by paraffin or silanes. However, these coatings may act as a sink for alkali atoms thereby significantly lower the atomic density [8]. A stable vapor pressure is established by having the vapor in thermal equilibrium with a droplet of alkali metal contained in a sidearm. Depolarizing collisions with the bulk metal are suppressed by connecting the cell proper to the sidearm via a small aperture.

The intrinsic linewidth resulting from the combined action of the mentioned depolarization effects depends on temperature, quality of the wall coating and cell geometry. Besides those intrinsic broadening mechanisms the interaction with the optical field and with the oscillating magnetic field further broaden the magnetic resonance line. These processes are known as optical and r.f. power broadening respectively.

4.2.2 Effects of hyperfine structure

The ground state of alkali atoms with a nuclear spin I splits into two hyperfine levels with total angular momenta $F_\pm = I \pm 1/2$ with $2F_\pm + 1$ Zeeman sublevels labeled by the magnetic quantum number M , respectively. The general evolution of the hyperfine levels in a magnetic field is described by the Breit-Rabi-Formula [9]. In low magnetic fields (Zeeman interaction \ll hyperfine interaction) the energy of the state $|F_\pm, M\rangle$ is shifted by

$\Delta E_{\pm, M} = g_{\pm} \mu_B B_0 M$. Here, μ_B is the Bohr magneton, and the g-factors g_{\pm} are given by

$$\begin{aligned} g_+ &= +\frac{1}{2I+1}g_J - \frac{2I}{2I+1}g_I \\ g_- &= -\frac{1}{2I+1}g_J - \frac{2I+2}{2I+1}g_I, \end{aligned} \quad (4.2)$$

where $g_J > 0$ is the electronic g-factor, defined via $\vec{\mu}_J = -g_J \mu_B \vec{J}/\hbar$ and g_I is the nuclear g-factor, defined via $\vec{\mu}_I = g_I \mu_B \vec{I}/\hbar$. The magnetic resonance process consists in driving transitions between adjacent sublevels with a resonance frequency ω_L given by

$$\nu_L = \left| \frac{\Delta E_{\pm, M+1} - \Delta E_{\pm, M}}{h} \right| = \left| \frac{g_{\pm} \mu_B B_0}{h} \right|, \quad (4.3)$$

which is equivalent to Eq. 4.1 with

$$\gamma_F = g_{\pm} \mu_B / \hbar. \quad (4.4)$$

For ^{133}Cs one has

$$\begin{aligned} \gamma_4/2\pi &= +3.4986 \text{ Hz/nT} \\ \gamma_3/2\pi &= -3.5098 \text{ Hz/nT}. \end{aligned} \quad (4.5)$$

In second order in the field B_0 the levels acquire an additional energy shift depending on M^2 and B_0^2 (quadratic Zeeman effect) which shifts the $|F_{\pm}, M\rangle \rightarrow |F_{\pm}, M+1\rangle$ transition frequency by an additional amount

$$|\Delta \nu_L^{(2)}| = \left(\frac{(g_J + g_I) \mu_B B_0}{h(2I+1)} \right)^2 \frac{2M+1}{\nu_{\text{hfs}}} = \frac{\epsilon}{2} B_0^2, \quad (4.6)$$

where ν_{hfs} is the ground state hyperfine splitting. The quadratic Zeeman effect thus splits the magnetic resonance into a series of equidistant lines separated by

$$\delta \nu^{(2)} = \epsilon B_0^2, \quad (4.7)$$

For cesium ($I = 7/2$), one has

$$\epsilon = 2.6716 \text{ nHz/nT}^2. \quad (4.8)$$

In the $2 \mu\text{T}$ field used here $\delta \nu^{(2)} = 0.011 \text{ Hz}$, which is much smaller than the resonance linewidth. The low field approximation (Eq. 4.1) is therefore valid for the present work.

4.2.3 Practical realization

In this work we compare the performance of lamp pumped and laser pumped magnetometers. Both devices have a common basic design consisting of

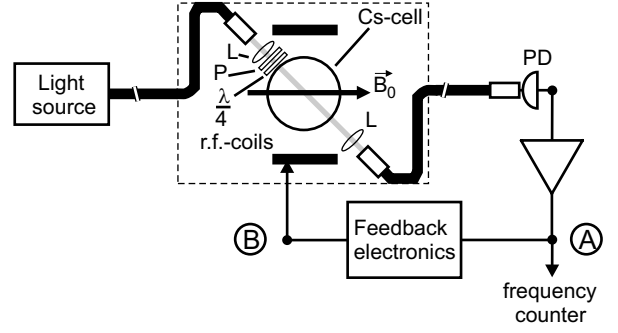


FIGURE 4.1: Principle of the M_x magnetometer. The light source is the discharge lamp or the diode laser as explained in the text. L: lens, P: polarizer and D_1 interference filter (in case of lamp pumping), $\lambda/4$: quarter-wave plate, PD: photodiode.

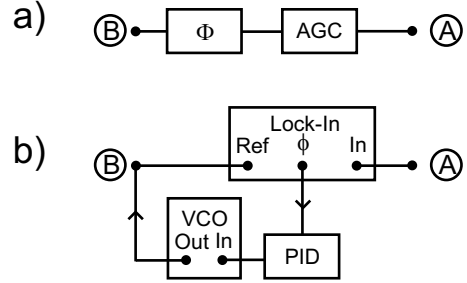


FIGURE 4.2: Scheme of feedback electronics in the self-oscillating mode (a) and in the phase-stabilized mode (b). AGC: amplitude gain control, Φ : phase shifter, VCO: voltage-controlled oscillator, PID: feedback controller.

the light source, the sensor head, the detector and feedback electronics (Figs. 4.1, 4.2). The sensor head contains the sensor proper, a spherical glass cell (60 mm diameter for the LpOPM, produced in the group of one of the authors, A.S.P., and 70 mm diameter for the LsOPM, purchased from MAGTECH Ltd., St. Petersburg, Russia) coated with paraffin in which cesium vapor is in thermal equilibrium with a droplet of metallic cesium at room temperature. The cell is mounted in a (200 mm long, 110 mm diameter) cylindrical housing. The pumping light is carried from the light source to the sensor cell by a multimode fiber (800 μm diameter) in the LsOPM and by a fibre bundle (6 mm diameter) in the LpOPM. The light transmitted through the cell is carried back to a detector (photodiode) by an identical fiber in the LsOPM and by an 8 mm diameter fiber bundle in the LpOPM. The lengths of the fibers are 8 m and 5 m length respectively for the laser and the lamp

pumped device. The sensor head contains also polarization optics (linear polarizer and quarter-wave plate) for making the light circularly polarized prior to entering the cell as well as lenses for collimating the incoming light and focussing the outgoing light into the return fiber (bundle). Particular care was taken to use only non-magnetic components in the sensor head. The coils producing the oscillating field consist of two 70 mm diameter loops with 12 turns of copper wire each, separated by 52 mm. When two sensors are operated in close proximity, the cross-talk of the respective r.f. fields is avoided by sliding a 1 mm thick Al cylinder over the heads. The optical, electronic and mechanical components of the LsOPM were produced at the University of Fribourg, while the LpOPM was realized at the Ioffe Institute.

The characterization of the magnetometers described in Sec. 4.3.1 was performed in Fribourg. Two magnetometers were placed inside of a multi-layer cylindrical magnetic shield as shown in Fig. 4.3 and Tab. 4.1. The magnetic field of $2\ \mu\text{T}$ was produced by a 50 cm long, 15 cm diameter solenoid driven by an ultra-low noise current supply.

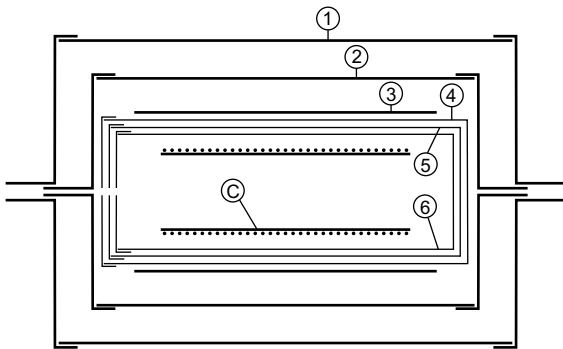


FIGURE 4.3: Scheme of the Fribourg shield. The labels 1–6 denote the different layers as described in Tab. 4.1. C: magnetic field coil.

For a direct comparison of the noise performance with an accuracy below 0.1 pT the level of magnetic field fluctuations at the experimental site have to be kept below that level, a performance, which is hard to realize. Magnetic field variations (in a 1 Hz bandwidth) in unshielded environments are of the order of several nT_{rms} or more. A shielding factor exceeding 10'000 is thus needed to suppress fluctuations at that level.

Layer	d (mm)	l (mm)	t (mm)	Material
1	600	900	1.5	Mumetal
2	450	750	1.5	Mumetal
3	300	600	1.5	Mumetal
4	285	743	0.76	Co-Netic
5	256	714	0.76	Co-Netic
6	229	686	0.76	Co-Netic

TABLE 4.1: The Fribourg magnetic shield. d : inner diameter, l : inner length, t : layer thickness. Note that all layers are closed by endcaps except of layer 3.

4.2.4 Features of the LsOPM and the LpOPM

In both types of magnetometers the D_1 transition $|6S_{1/2}\rangle \rightarrow |6P_{1/2}\rangle$ of Cs at a wavelength of 894 nm is used for optical pumping. The LpOPM is driven by an electrodeless discharge lamp, in which a power stabilized high frequency generator ($\sim 100\text{ MHz}$) produces a discharge in a 12 mm diameter glass bulb containing cesium vapor and Xenon as buffer gas. The pumping light is collimated and filtered by a D_1 interference filter centered at 894.5 nm with a FWHM=11.5 nm. Because of the high temperature of the discharge plasma the spectrum of the emitted D_1 radiation is considerably broader than the Doppler width of the room temperature absorption line in the sensor cell. All four hyperfine components of the D_1 line are excited simultaneously as indicated in Fig. 4.4(a). As the same light is used for detecting the ground state spin precession the LpOPM detects magnetic resonance in both the $F=4$ and the $F=3$ hyperfine ground states. Because of the differing g -factors of the two states (Eq. 4.6) the corresponding magnetic resonance lines are split by 22 Hz in the $2\ \mu\text{T}$ field, which is larger than the width of the magnetic resonance lines ($\sim 2.5\text{--}5\text{ Hz}$) under optimized conditions. The $F=3$ component is much weaker than the $F=4$ component, so that the former plays a minor role for magnetometry.

The LsOPM is pumped by a tunable extended cavity laser in Littman configuration (Sacher Lasertechnik, model TEC500). The output power of more than 10 mW exceeds the power required for magnetometry by more than three orders of magnitude. Therefore a single laser can be used to drive dozens of magnetometers in experiments calling for the simultaneous monitoring of the magnetic field in different locations. The laser frequency is actively

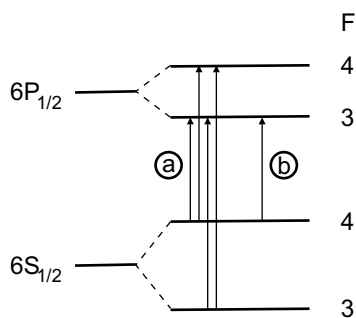


FIGURE 4.4: Hyperfine structure of the cesium D_1 line. The arrows indicate the transitions driven by the discharge lamp (a) and the laser (b).

stabilized to the Doppler broadened $F = 4 \rightarrow F = 3$ hyperfine transition using a dichroic atomic vapor laser lock (DAVLL) [10] in an auxiliary (vacuum) cesium cell. This lock is very stable and allows a reliable operation of the magnetometer over measurement periods of several weeks.

In both magnetometers the states $|6S_{1/2}; F = 4, M = 4\rangle$ are dark states¹ which can not absorb circularly polarized light. At the same time the repopulation of absorbing (bright) states by the magnetic resonance r.f. transitions from these levels is used for the optical detection of the magnetic resonance. The LsOPM drives the $|6S_{1/2}; F = 4\rangle \rightarrow |6P_{1/2}; F = 3\rangle$ transition, and excited atoms can decay into any of the sublevels of the $|6S_{1/2}; F = 3\rangle$ hyperfine state, which do not interact with the narrow band light. This process, called hyperfine pumping, degrades the efficiency of the optical pumping process and reduces the overall spin polarization which can be achieved with laser radiation. A straightforward way to reduce that loss is to empty the $|6S_{1/2}; F = 3, M\rangle$ sublevels using a repumping laser tuned to a transition emanating from the $F=3$ hyperfine ground state. An experimental study of that process is underway. In the LpOPM all four hyperfine components are pumped simultaneously. As a result the loss due to hyperfine pumping is excluded and a larger spin polarization is obtained in the $F=4$ state. The drawback of the large spectral width of the beam from the lamp is that an appreciable part of its spectrum lies outside of the room temperature absorption spectrum of the sensor cell. The corresponding photons carry

¹Owing to the resolved hyperfine structure in the LsOPM the states $|6S_{1/2}; F = 4, M = 3\rangle$ and $|6S_{1/2}; F = 3, M\rangle$ are also dark states.

no spectroscopic information, but produce excess shot noise in the detected photocurrent. In that respect narrow-band laser light leads to a better detection efficiency in the LsOPM.

4.2.5 Modes of operation

Both types of magnetometers were operated in two different modes. The self-oscillating mode (SOM) (Fig. 4.2 a) uses the fact that at resonance the driving r.f. field and the modulated photocurrent are dephased by 90° . For that reason the sinusoidal part of the photocurrent can be used, with an appropriate amplification and phase shift to drive the r.f. coils in a feedback loop. In such a configuration the system will auto-oscillate at the Larmor frequency. An amplitude gain control ensures that the amplitude of the coil current is kept constant independently of phase and frequency, so that any r.f. power dependent systematic effects are suppressed.

The phase-stabilized mode (PSM) (Fig. 4.2 b) also uses the characteristic phase dependence between the applied oscillating field and the modulation of the detected photocurrent for locking the frequency of an external oscillator to the Larmor frequency. The phase, the in-phase component, and the quadrature component are detected simultaneously by a lock-in amplifier (Stanford Research Systems SR830). Both the in-phase signal (dispersive Lorentzian) and the 90° phase shifted phase signal (arctan-dependence) show a linear zero-crossing near zero detuning ($\omega_{rf} = \omega_L$). Either of the two signals can thus be used as discriminant in a feedback loop, which stabilizes the phase to 90° . It can be shown that from a statistical point of view both signals yield an equivalent magnetic field sensitivity. The phase signal is less sensitive to light power fluctuations, which may be advantageous to suppress systematic effects related to power fluctuations [11]. However, the used commercial digital lock-in amplifier had only a moderate update rate of 400 Hz of its phase output, so that the much faster in-phase signal was used in the feedback loop.

In principle the PSM can be understood as a variant of the SOM, in which the phase-detector, the VCO, and the feedback controller form a tracking filter. In both modes of operation changes of the magnetic field lead to instantaneous changes of the Larmor frequency and thus to instantaneous changes of the transmitted modulation frequency.

The time needed for the radio-frequency to adjust to a new value after a sudden field change depends on the filters and other delays in the feedback loop. If a very fast response is not required, as in our applications, the bandwidth can be decreased by appropriate filters. In the SOM it is the preamplifier of the photodetector which limits the bandwidth to 10 kHz, whereas in the PSM the feedback loop filters provide a bandwidth up to 1 kHz [4]. From a practical point of view the registered bandwidth is limited by the data acquisition system. Because of the frequency dependence of the phase-shifter the SOM is, in general, optimized only for a given Larmor frequency, which reduces the dynamic range of the SOM device. The phase-stabilized magnetometer keeps the phase-shift at 90° independently of the Larmor frequency. In practice the dynamic range is limited by the frequency range of the voltage-controlled oscillator (VCO) used to generate the oscillating field. The long-term stability of both feedback schemes is limited by temperature dependent phase drifts.

The Al shield slipped over each magnetometer for avoiding cross-talk effectively acts as a low-pass filter for external magnetic field fluctuations (skin effect) which reduces the response bandwidth of all devices to about 250 Hz (Fig. 4.5).

4.3 Performance

4.3.1 Magnetometric sensitivity: Basics and fundamental limit

The sensitivity of the magnetometer is defined as the noise equivalent magnetic flux density (NEM), which is the flux density change δB equivalent to the total noise of the detector signal. In a perfectly stable external magnetic field the smallest detectable field changes are limited by the intrinsic magnetometer noise δB_{int} . For a measurement bandwidth $\Delta\nu_{\text{bw}}$ the intrinsic resolution δB_{int} depends on the magnetic resonance linewidth $\Delta\nu$ (HWHM) and on the signal-to-noise ratio S/N_{int} of the magnetometer signal according to

$$\delta B_{\text{int}} = \frac{1}{\gamma} \times \frac{\Delta\nu}{S/N_{\text{int}}}. \quad (4.9)$$

For a feedback operated magnetometer using an optically thin medium ($\kappa L \ll 1$) the light power (expressed in terms of photocurrent) detected after

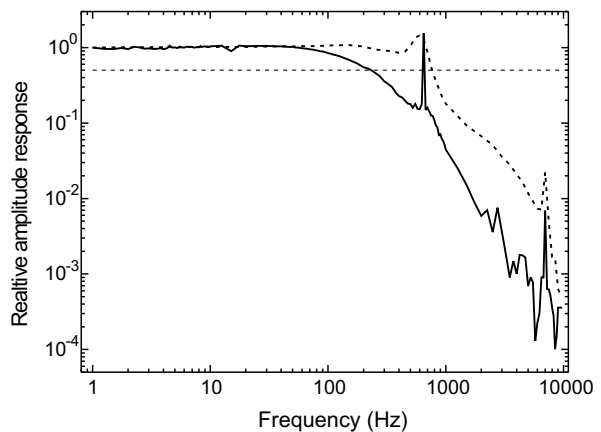


FIGURE 4.5: Normalized amplitude response of the LsOPM (PSM) to a periodic magnetic field change, measured at the VCO input: with Al shield (full line) and without Al shield (dashed line). The horizontal dashed line indicates an amplitude response of 0.5. In both cases the loop filter was adjusted to be about 750 Hz. By using the Al shield the bandwidth is reduced to about 250 Hz. Note that using the phase-stabilized LpOPM yields the same result since the bandwidth is independent of the light source.

the sensor cell is given by

$$I_{\text{pc}} = I_{\text{in}} \exp(-\kappa L) \approx I_{\text{in}}(1 - \kappa L), \quad (4.10)$$

where I_{in} is the incident power, κ the resonant optical absorption coefficient and L the sample length. The absorption coefficient can be written as

$$\kappa = \kappa_0(1 + \eta \cos \omega_L t), \quad (4.11)$$

where κ_0 is the mean absorption coefficient and η is the modulation depth which depends - among others - on the degree of spin polarization and the amplitude of the oscillating field. We can then write Eq. 4.10 as

$$I_{\text{pc}} = I_0 + I_m \cos \omega_L t = I_0(1 + \xi \cos \omega_L t), \quad (4.12)$$

where $I_0 = I_{\text{in}}(1 - \kappa_0 L)$ and $I_m = \eta \kappa_0 L I_{\text{in}} = \xi I_0$. The contrast ξ is the ratio of the modulation amplitude and the average photocurrent in the approximation $\kappa_0 L \ll 1$. The signal S is given by the rms value of the oscillating part of the magnetometer signal

$$S = \xi I_0 / \sqrt{2}. \quad (4.13)$$

The fundamental limit of the magnetometric sensitivity is obtained for a shot-noise limited signal,

with a noise level $N_{\text{int}} = N_{\text{SN}} = \sqrt{2eI_0\Delta\nu_{\text{bw}}}$ of I_{pc} . The shot-noise limited sensitivity then reads

$$\delta B_{\text{SN}} = \frac{\Delta\nu}{\gamma} \frac{2}{\xi} \sqrt{\frac{e\Delta\nu_{\text{bw}}}{I_0}}. \quad (4.14)$$

The magnetometer signal of interest is contained in the amplitude and phase of the sinusoidal modulation of the light power after the sensor cell. The power spectrum of the spectral power density of an ideal magnetometer in a perfectly stable magnetic field thus consists of a delta function centered at the Larmor frequency, superposed on a flat background of shot-noise fluctuations. In practice the peak is broadened by the resolution (1 Hz) of the FFT analyzer (Stanford Research Systems, model SR760) used for its recording. The relevant noise contributions which define the S/N ratio are fluctuations of the photocurrent at the Larmor frequency, i.e., the value of the background below the Larmor peak. In practice that ideal spectrum is modified by various imperfections which degrade the magnetometer performance. In the following we address contributions from light power fluctuations and magnetic field fluctuations.

4.3.2 Limitations by light power fluctuations

The light power I_{in} has a continuous (technical) noise spectrum, which lies above the shot-noise level, in particular at frequencies below 100 Hz, as shown for the laser in Fig. 4.6. The individual peaks are even and odd harmonics of the 50 Hz line frequency. Power fluctuations contribute to the photocurrent noise at ω_L by two distinct processes. First, there is a direct contribution via the noise component of I_0 in Eq. 4.12 at the Fourier frequency ω_L . At $\omega_L/2\pi = 7\text{kHz}$ this noise level is close to the shot-noise level. The second contribution is due to the second term in (4.12). Each Fourier component (at ω) of the power fluctuations is multiplied by $\cos\omega_L t$, and this mixing produces sidebands at $\omega_L \pm \omega$ in the power density spectrum. In this way the continuous low frequency part of the technical noise around $\omega = 0$ (Fig. 4.6) produces a symmetric background under the Larmor peak. Although the power noise around $\omega = 0$ is 18 times (Fig. 4.6) larger than the shot noise around $\omega = \omega_L$, it is suppressed – according to Eq. 4.12 – by a factor ξ , which has a value of approximately 0.05 in the LsOPM. As a consequence the contribution of the modulation term in

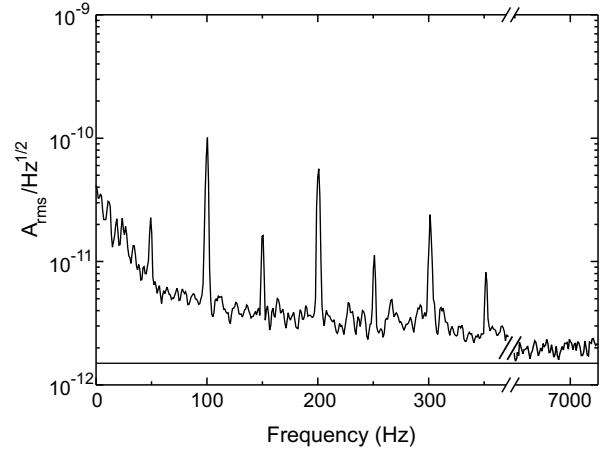


FIGURE 4.6: Power spectral density of the low frequency noise of the laser power. The power was $13\ \mu\text{W}$ and the corresponding shot-noise level is shown as solid line. The noise at 7 kHz, which lies 50% above the shot noise level, is also shown.

Eq. 4.12 to the photocurrent noise is less than the contribution from I_0 . We have verified that this is indeed fulfilled in a carefully calibrated auxiliary experiment.

4.3.3 Limitations by magnetic field fluctuations

In presence of uncorrelated magnetic field fluctuations, δB_{ext} , the highest resolution with which a magnetic field change can be detected is given by $\delta B = \sqrt{\delta B_{\text{int}}^2 + \delta B_{\text{ext}}^2}$. The fluctuations δB_{ext} of the external magnetic field can be parameterized by the equivalent noise N_{ext} that they produce on the signal, and δB can be expressed in a form similar to Eq. 4.9 by

$$\delta B = \frac{1}{\gamma} \times \frac{\Delta\nu}{S/N}, \quad (4.15)$$

where $N^2 = N_{\text{int}}^2 + N_{\text{ext}}^2$. Fourier components of the field fluctuations at frequency ω will mix with the magnetometer oscillation frequency ω_L in Eq. 4.12. Monochromatic field fluctuations, such as the 50 Hz line frequency and harmonics thereof produce symmetric sidebands, while low frequency magnetic field fluctuations produce a continuous background underlying the Larmor peak.

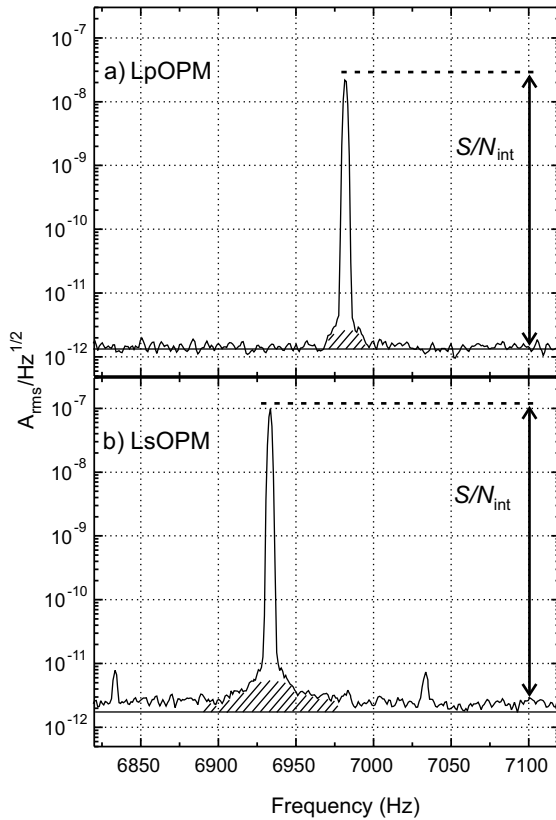


FIGURE 4.7: Power spectral density plots of the photocurrent fluctuations in the LpOPM (a) and the LsOPM (b), both operated in the *phase-stabilized mode*. The signal-to-noise ratios S/N_{int} are 29000 (a) and 98000 (b) respectively. The photocurrents are $4.3 \mu\text{A}$ for the LpOPM and $5 \mu\text{A}$ for LsOPM. The corresponding shot-noise levels are represented by the horizontal lines. The dashed areas indicate the pedestal discussed in the text.

4.3.4 Measurement of the intrinsic sensitivity

The intrinsic linewidth of the magnetic resonance transition was measured by extrapolating the experimental linewidth to zero light power and zero r.f. power. We found a HWHM of 1.63 Hz for the cell in the LpOPM and 2.35 Hz for the cell in the LsOPM. As all cells were manufactured by the same person the difference of the intrinsic linewidths is probably due to the slightly larger aperture between the cell and the sidearm in the case of the LsOPM. After optimizing the signal-to-noise ratio with respect to light and r.f. power the (power-broadened) magnetic resonance linewidth (HWHM) is $\Delta\nu = 2.5 \text{ Hz}$ for the LpOPM and 5.0 Hz for the LsOPM.

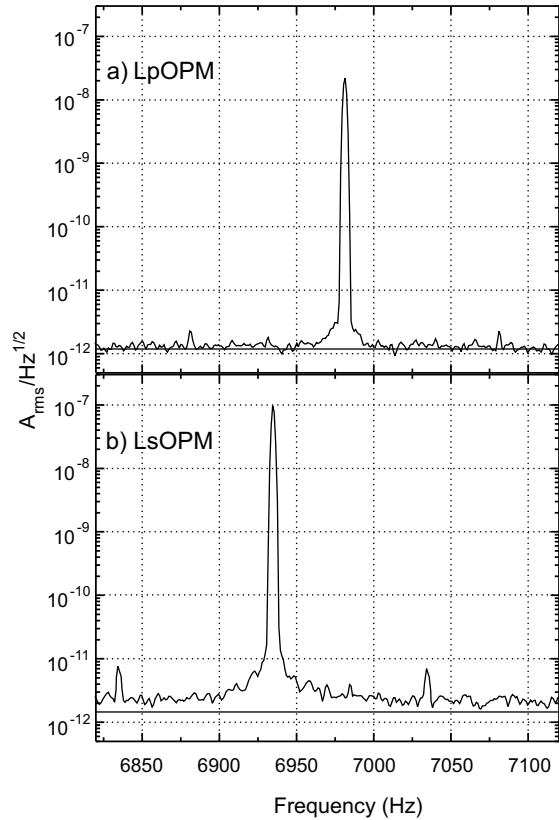


FIGURE 4.8: Power spectral density plots of the photocurrent fluctuations in the LpOPM (a) and the LsOPM (b), both operated in the *self-oscillating mode*. The signal-to-noise ratios are similar to those in Fig. 4.7 and the corresponding shot-noise levels are represented by horizontal lines.

Figures 4.7 and 4.8 show typical power density spectra – recorded in the phase-stabilized and self-oscillating mode of operation – of the r.m.s. voltage fluctuations at the output of the current-to-voltage preamplifier of the photodiode current. The spectra contain all structures discussed above. The pedestal (indicated as dashed area in Fig. 4.7) underlying the Larmor peak contains contributions from fluctuations of the light power and of the magnetic field. The white noise floor in the far wings of the central structure represents the intrinsic OPM noise N_{int} . Its numerical value for use in Eq. 4.9 was measured 70 Hz above the carrier. At that frequency this noise represents the noise component of I_0 of the power noise in Eq. 4.12. We have verified that the noise component of the modulated contribution in Eq. 4.12 is 8 times less than the noise contribution of I_0 under present experimental conditions. The pedestal under the Larmor peak is thus most

probably due to low-frequency field fluctuations.

After optimizing the magnetometric sensitivity with respect to light power and r.f. power the LpOPM yields a S/N ratio of 29000, while the LsOPM reaches 98000 in a bandwidth $\Delta\nu_{\text{bw}}$ of 1 Hz. It can be seen from the figures that the signal-to-noise ratio does not depend on the mode of operation (SOM or PSM). For the LpOPM the shot-noise level is nearly reached while in the LsOPM $N_{\text{int}} = 1.5 \times N_{\text{SN}}$. According to Eq. 4.9 the measured S/N ratios and linewidths under optimized conditions result a NEM δB_{int} of 25 fT for the LpOPM and of 15 fT for the LsOPM in a bandwidth of 1 Hz. The LsOPM is thus 1.7 times more sensitive than the LpOPM, although its performance is not yet shot-noise limited.

4.3.5 Discussion

In order to get a better understanding of the excess power noise in the LsOPM we measured the dependence of the photocurrent noise on the light power for the laser in comparison to that of the lamp. In those measurements only the noise component of I_0 (Eq. 4.12) at 7 kHz was recorded as it represents the dominant noise contribution of I_{pc} . For each of the measurements the cesium cell was removed and the light beam was detected directly by the photodiode using a transimpedance amplifier for the photocurrent. The noise N_0 measured in this way gives a lower limit of the intrinsic magnetometer performance. The results for the laser and lamp source are shown in Fig. 4.9. The noise can be written as

$$N_0^2 = N_{\text{SN}}^2 + N_{\text{dark}}^2 + N_{\text{T}}^2, \quad (4.16)$$

where N_{SN} is the shot-noise of the photocurrent I_0 , N_{dark} the intrinsic detector (photodiode and amplifier) noise, and N_{T} technical noise of the light source, which is proportional to I_0 .

N_{dark} was measured with the light beams blocked for all (discrete) amplification stages of the transimpedance amplifier. With the highest amplification ($10^{-1} \mu\text{A}/\text{V}$) used for $I_0 < 600 \text{ nA}$ we measured $N_{\text{dark}} = 48 \text{ fA}/\sqrt{\text{Hz}}$. This corresponds to the shot noise of a current I_0 of 7 nA, so that above 7 nA the intrinsic detector noise can be neglected. This dark current is responsible for the deviation of the measured noise from the (dotted) shot-noise line (Fig. 4.9) at low currents.

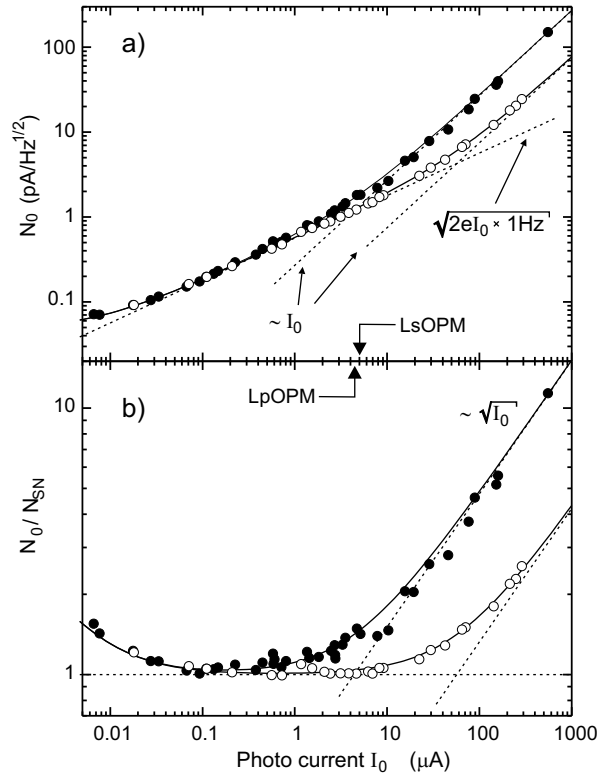


FIGURE 4.9: a) Measured noise N_0 of the photocurrent produced by laser light (black dots) and by light from the discharge lamp (open circles) at 7 kHz. The measurement bandwidth was 1 Hz. The dashed lines indicate the calculated photodiode shot noise ($\propto \sqrt{I_0}$) and the fitted technical laser noise ($\propto I_0$). b) Ratio of N_0 to the calculated shot noise N_{SN} . The technical noise appears to be proportional to $\sqrt{I_0}$ in this representation. The full lines in both plots represent the calculated sum of all noise contributions according to Eq. 4.16. The arrows refer to the (optimized) photocurrent for both devices.

For larger photocurrents technical noise N_{T} , which is proportional to the light power, dominates over the shot noise. We found $N_{\text{T}} = k \cdot I_0$, with $k_{\text{Ls}} = 2.6 \times 10^{-7}$ and $k_{\text{Lp}} = 0.8 \times 10^{-7}$ for the laser and the lamp source respectively. With the laser source the shot noise N_{SN} becomes equal to the technical noise N_{T} for a photocurrent I_0 of $4.9 \mu\text{A}$, which thus yields a noise level $N_0 = \sqrt{2}N_{\text{SN}}$ at that photocurrent. The laser power for optimized magnetometer parameters corresponds to $5 \mu\text{A}$, thereby explaining the excess noise of the LsOPM in Figs. 4.7 and 4.8. In the case of lamp pumping the technical noise becomes important for $I_0 > 60 \mu\text{A}$, so that the magnetometer is shot-noise limited for

the (optimized) photocurrent of $4.3 \mu\text{A}$.

If one succeeds in eliminating the excess noise of the laser power, e.g., by an active power stabilization of the LsOPM one can achieve an intrinsic shot-noise limited sensitivity of 10 fT , thereby outperforming the LpOPM by a factor of 2.5. This is compatible with earlier results [12] obtained from a comparative study of lamp and laser pumped magnetometers using ^{39}K , in which the sensitivity of the LsOPM version was found to be 2.3 times higher than of the corresponding LpOPM device. It is also interesting to compare those results with the present results on an absolute scale. The sensitivity of the ^{39}K -LsOPM was found to be $1.8 \text{ fT}/\sqrt{\text{Hz}}$. This superior performance compared to the ^{133}Cs magnetometer discussed here is mainly due to the two times larger diameter of the potassium sensor cell, which, combined with the appreciably smaller spin exchange cross section of potassium, led to an operating linewidth of 1 Hz compared to 5 Hz with the present Cs-LsOPM. Furthermore the g-factor of ^{39}K is twice as large than that of ^{133}Cs . These two factors explain the superior performance of the K-magnetometer (1.8 fT) compared to the Cs magnetometer (15 fT).

4.4 Applications

4.4.1 Direct comparison of LsOPM and LpOPM

We performed a direct comparison of the performance of the LpOPM and the LsOPM in simultaneous measurements of magnetic field fluctuations inside the multilayer shield described above (Fig. 4.3). Both devices were mounted coaxially in the shield and the centers of their sensor cells were separated by 21 cm . The oscillatory signal of each magnetometer was filtered by a resonance amplifier, centered near 7 kHz with a FWHM of 500 Hz , and analyzed by a frequency counter (Stanford Research Systems, model SR620) with a gate time of 0.1 s . An example of such a recording over a continuous interval of 6 hours with the LpOPM operated in PSM and the LsOPM operated in the SOM is shown in Fig. 4.10. One sees that both devices oscillate at different average frequencies, which can be explained by the presence of a magnetic field gradient of 66 pT/cm which drifts by 0.4% over the 6 hour interval. The drift is probably due to a thermal drift of the shield's magnetization. Simi-

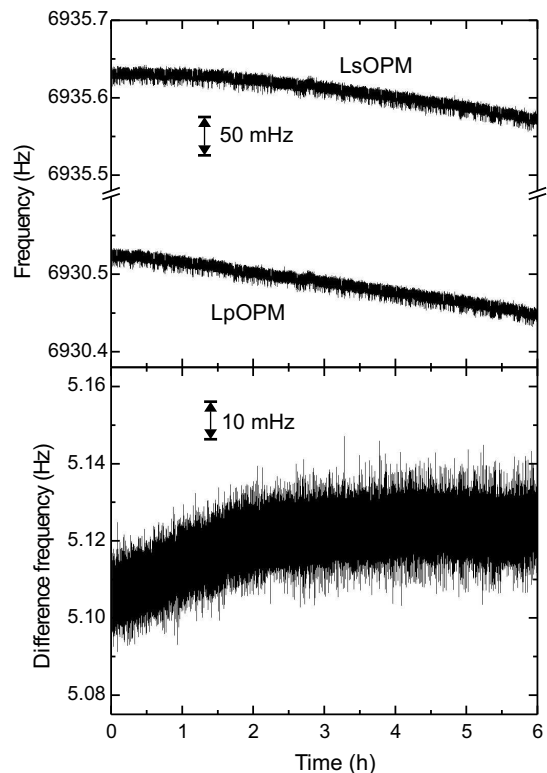


FIGURE 4.10: Fluctuations of the Larmor frequency recorded with the LpOPM (PSM) and the LsOPM (SOM) recorded over 6 hours (top traces). The difference of both frequencies shows a drift of the field gradient (bottom trace).

lar gradients were measured after interchanging the positions of the two OPMs. Figure 4.11 shows a 5 minutes time slice of the data in Fig. 4.10.

There are highly correlated irregular field jumps of approximately 3.6 pT in both traces. These fluctuations correspond to relative fluctuations of the solenoid current at a level of 10^{-6} and are suspected to be caused by the current source. The Allan standard deviation [13] of the data is a convenient way for characterizing the field drifts on various time scales. Fig. 4.12 shows the Allan plot of the data from Fig. 4.10 as a function of integration time both in absolute and in relative units. Both magnetometers show the same field stability and the data points are indistinguishable for small integration times. While the short term stability is governed by white noise, the bump between 1 and 200 s is due to the irregular field jumps. The long term stability is determined by long term field drifts of the imperfectly shielded external field and thermal drifts of the solenoid support structure.

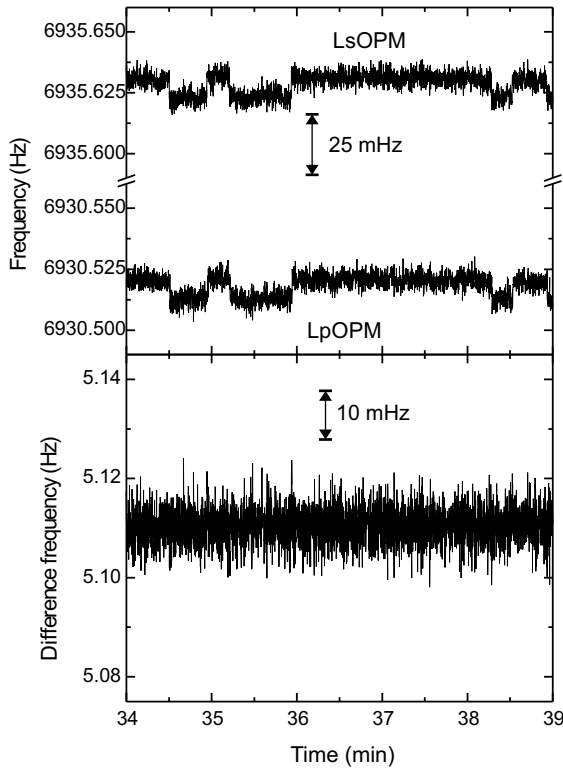


FIGURE 4.11: Five-minutes slices of the traces in Fig. 4.10. Individual readings of the magnetometers (top) and of their difference frequency (bottom).

4.4.2 Systematic effects

The magnetometric performance is affected by the following systematic effects. Any deviations of the phase shift $\delta\phi$ from the optimum value of $-\pi/2$ in the loop will change the measured frequency by an amount $\delta\nu = \Delta\nu \delta\phi$. As $\delta\phi$ can not be controlled on a very high level this type of magnetometer is not a highly accurate device. However, as long as the phase shift is kept constant, e.g., by temperature stabilizing the feedback electronics, the sensitivity is not affected.

When the laser frequency is detuned from resonance the Larmor frequency will be systematically changed by the light shift, which acts as an effective additional magnetic field. In that situation light power fluctuations will also limit the sensitivity. Light shift effects are less dramatic in the case of lamp pumping as the broad spectrum of the resonance lines from the lamp cancels the dispersively shaped light shift dependence. At the level of field fluctuations reported here false effects induced by

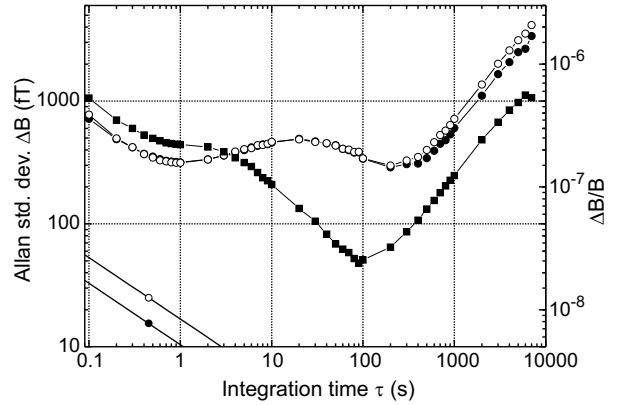


FIGURE 4.12: Allan standard deviation of the time traces in Fig. 4.10. Open circles: LpOPM measurement, black dots: LsOPM measurement, black squares: field gradient measured over 21 cm. For times below 200 seconds the LsOPM data and the LpOPM data points overlap and cannot be distinguished. The lines are drawn to guide the eye. In the two lower graphs the single points at $\tau = 0.5$ s indicate the NEM of the LpOPM (open circle) and of the LsOPM (black dot), and their extrapolation to other integration times assuming white noise.

the light shift are negligible. Details of this are discussed in [4].

As shown in Sec. 4.2.2 the different Zeeman transitions can not be resolved in a magnetic field of $2\mu\text{T}$. Only in magnetic fields between $10\mu\text{T}$ and $200\mu\text{T}$, where the quadratic Zeeman splitting is on the order of the resonance linewidth, the resonance line appears to be asymmetric and light power fluctuations induce fluctuations of that asymmetry, which then yield frequency changes.

4.4.3 Active field stabilization

We have further investigated the performance of the magnetometers in an active magnetic field stabilization system using a phase-locked loop. For that purpose the phase of the LpOPM oscillation (PSM) relative to the phase of a reference oscillator was measured by a lock-in amplifier and used as error signal driving a correction coil. While field fluctuations common to both sensors are strongly suppressed by this method, gradient drifts and fluctuations are not compensated and thus detected by the free-running magnetometer.

The performance of the stabilization scheme is shown in Fig. 4.13, where the top traces represent

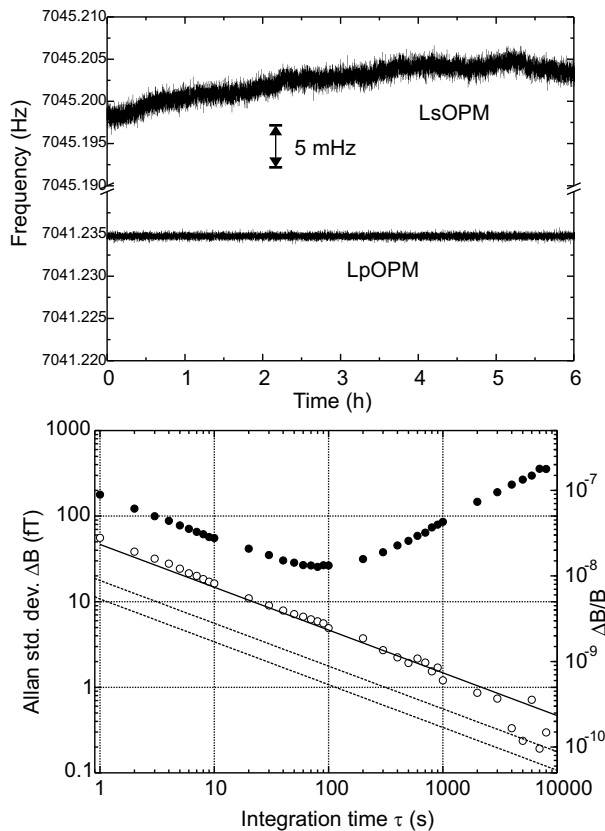


FIGURE 4.13: Field fluctuations in both sensors when the field is stabilized to the LpOPM signal. Upper graph: Time series of the residual fluctuations, recorded with a 1 s gate time of the frequency counter. Lower graph: Allan standard deviations of the time traces: LpOPM (open circles) and LsOPM (black dots). The solid line represents the resolution limit of the frequency counter. The dashed lines indicate the NEM of the LpOPM (upper) and of the LsOPM (lower).

time series of the field readings (1 s gate time of the frequency counter) of the free-running LsOPM and the LpOPM used for the feedback. The lower part of Fig. 4.13 shows the Allan standard deviation of those data. The jumps in the magnetic field measured by the LsOPM (Fig. 4.11) are completely suppressed by the feedback loop and only white noise in the short term stability and contributions from gradient drifts in the long term stability remain. The field fluctuations reach a minimum of 25 fT for $\tau = 100$ s, which corresponds to a relative field stability of 1.3×10^{-8} . Due to the fact that the field is stabilized to the LpOPM one would expect a significant lowering of the LpOPM's Allan standard deviation for short integration times. The white

noise behavior (slope $-1/2$ in the Allan plot) of the LpOPM trace is entirely due to the resolution of the frequency counter, which is limited by trigger time jitter due to amplitude noise of the measured sine wave.

We also realized a setup, in which the roles of the LsOPM and the LpOPM were reversed. The observed performance was identical with the one described.

4.5 Further applications

OPMs based on Cs vapor are well suited for operation in magnetic fields smaller than $10 \mu\text{T}$ (such as typical fields used in neutron EDM experiments). As already mentioned above in such fields asymmetries of the magnetic resonance line due to the quadratic Zeeman effect will not affect their long-term stability (accuracy). In magnetic fields above $300 \mu\text{T}$ the quadratic Zeeman shift exceeds the linewidth and the magnetic resonance spectrum consists of 8 resolved lines [14]. This offers a further possibility for the use of cesium magnetometers. The performance of the LsOPM in that field range is expected not to be worse than the one measured in a $2 \mu\text{T}$ field. This expectation is based on the fact that the (performance determining) laser power noise does not increase with frequency, so that a shot-noise limited sensitivity can be reached. A magnetometer based on the quadratic Zeeman effect in potassium has been demonstrated earlier [15].

In contrast to buffer gas cells, which require the whole cell volume to be illuminated in order to achieve a maximum sensitivity, paraffin-coated cells can be pumped with a laser beam of much smaller diameter. This allows one to adapt the spatial dimensions of the paraffin-coated sensors to specific experimental requirements. One can think, e.g., of using very large cells of several liters for measuring volume averaged fields. Compared to other proposed large cell schemes [3], the use of a Cs-OPM offers the further advantage of a high temporal resolution. Recently, a novel type of optically pumped magnetometer with a sub-fT (gradiometric) sensitivity was demonstrated [16]. Besides its use of very high buffer gas pressures and its operation at a temperature of 190°C , specific features of that magnetometer are its limited operation range near zero field and its reduced bandwidth of 20 Hz.

ACKNOWLEDGMENTS We thank G. Bison for fruitful discussions and careful reading of this manuscript. We acknowledge financial support from Schweizerischer Nationalfonds, INTAS, and Paul Scherrer Institute (PSI). One of the authors (A.S.P.) acknowledges financial support from the University of Fribourg.

References

- [1] K. Green, P. G. Harris, P. Iaydjiev, D. J. R. May, J. M. Pendlebury, K. F. Smith, M. van der Grinten, P. Geltenbort, and S. Ivanov. *Performance of an atomic mercury magnetometer in the neutron EDM experiment*. Nucl. Instr. and Meth. A **404**(2-3), 381–393 (1998).
- [2] I. S. Altarev, Y. V. Borisov, N. V. Borovikova, A. I. Egorov, S. N. Ivanov, E. A. Kolomensky, M. S. Lasakov, V. M. Lobashev, V. A. Nazarenko, A. N. Pirozhkov, A. P. Serebrov, Y. V. Sobolev, and E. V. Shulgina. *Search for the neutron electric dipole moment*. Physics of Atomic Nuclei **59**(7), 1152–1170 (1996).
- [3] Yu. Borisov, W. Heil, M. Leduc, V. Lobashev, E.W. Otten, and Yu. Sobolev. *Feasibility study of a ^3He -magnetometer for neutron electric dipole moment experiments*. Nucl. Instr. and Meth. A **440**(3), 483–488 (2000).
- [4] S. Groeger, J.-L. Schenker, R. Wynands, and A. Weis. *A high-sensitivity laser-pumped M_x magnetometer*. arXiv:physics/0406105 v2 19 Aug 2004).
- [5] O. Moreau, B. Cheron, H. Gilles, J. Hamel, and E. Noel. *Laser diode pumped He-3 magnetometer*. J. Phys. III **7**(1), 99–115 (1997).
- [6] H. Gilles, J. Hamel, and B. Cheron. *Laser pumped He-4 magnetometer*. Rev. Sci. Instr. **72**(5), 2253–2260 (2001).
- [7] A. P. Kazantsev, V. S. Smirnow, A. M. Tumaikin, and I. A. Yagofarov. *Effect of atomic ground-state self-polarization in the cycle of optical-pumping on the increase of linear light-absorption for $F=J \rightarrow J+1$ transitions*. Opt. Spectrosc. **57**(2), 189–191 (1984).
- [8] E. B. Alexandrov, M. V. Balabas, D. Budker, D. English, D. F. Kimball, C.-H. Li, and V. V. Yashchuk. *Light-induced desorption of alkali-metal atoms from paraffin coating*. Phys. Rev. A **66**, 042903 (2002).
- [9] G. Breit and I. I. Rabi. *Measurement of nuclear spin*. Phys. Rev. **38**(11), 2082–2083 (1931).
- [10] V. V. Yashchuk, D. Budker, and J. R. Davis. *Laser frequency stabilization using linear magneto-optics*. Rev. Sci. Instrum. **71**(2), 341–346 (2000).
- [11] G. Bison, R. Wynands, and A. Weis. *Optimization and performance of an optical cardio-magnetometer*. J. Opt. Soc. Am. B. **22**(1), 77–87 (2005).
- [12] E. B. Aleksandrov, M. V. Balabas, A. K. Verhovskii, A. E. Ivanov, N. N. Yakobson, V. L. Velichanskii, and N. V. Senkov. *Laser pumping in the scheme of an M_x -magnetometer*. Opt. Spectrosc. **78**(2), 325–332 (1995).
- [13] J.A. Barnes, A. R. Chi, L.S. Cutler, D.J. Healey, D.B. Leeson, T.E. McGunigal, J.A. Mullen, Jr., W.L. Smith, R.L. Sydnor, R.F.C. Vessot, and G.M.R. Winkler. *Characterization of frequency stability*. IEEE Trans. Instrum. Meas. **20**, 105–120 (1971).
- [14] D. Nettels, R. Müller-Siebert, S. Ulzega, and A. Weis. *Multi-photon processes in the zeeman structure of atomic Cs trapped in solid helium*. Appl. Phys. B **77**(6–7), 563–570 (2003).
- [15] E. B. Alexandrov, A. S. Pazgalev, and J. L. Rasson. *Observation of four-quantum resonance in zeeman structure in the potassium-39 ground-state*. Opt. Spectrosc. **82**(1), 14–20 (1997).
- [16] I. K. Kominis, T. W. Kornack, J. C. Allred, and M. V. Romalis. *A subfemtotesla multi-channel atomic magnetometer*. Nature **422** (6932), 596–599 (2003).

Chapter 5

A sound card based multi-channel frequency measurement system

S. Groeger^{1,2}, G. Bison¹, P. E. Knowles¹, and A. Weis¹

¹*Département de Physique, Université de Fribourg, Chemin du Musée 3, 1700 Fribourg, Switzerland*

²*Paul Scherrer Institute, 5232 Villigen PSI, Switzerland*

Submitted to Eur. Phys. J. AP

ABSTRACT: For physical processes which express themselves as a frequency, for example magnetic field measurements using optically-pumped alkali-vapor magnetometers, the precise extraction of the frequency from the noisy signal is a classical problem. We describe herein a frequency measurement system based on an inexpensive commercially available computer sound card coupled with a software single-tone estimator which reaches Cramér–Rao limited performance, a feature which commercial frequency counters often lack. Characterization of the system and examples of its successful application to magnetometry are presented.

5.1 Introduction

The present work is motivated by the need for a high resolution frequency measurement system for analyzing signals generated by optically-pumped cesium magnetometers [1]. A set of such magnetometers will be used for a detailed investigation of magnetic field fluctuations and gradients in an experiment searching for a neutron electric dipole moment (nEDM). The experiment calls for a magnetic field of between 1 to 2 μT controlled at the 80 fT level when measured over 100 s time intervals, control corresponding to a relative uncertainty between 40 to 80 ppb. The magnetometers are based on the fact that for low magnetic fields the Larmor precession frequency f_L in a vapor of Cs atoms is proportional to the modulus of the magnetic field \vec{B}

$$f_L = \gamma |\vec{B}|. \quad (5.1)$$

The proportionality factor γ is a combination of fundamental and material constants and has a value of $\approx 3.5 \text{ kHz}/\mu\text{T}$ for ^{133}Cs . The precession of the atoms modulates the resonant absorption coefficient of the cesium vapor, which is measured by a photodiode monitoring the power of a laser beam traversing the atomic vapor [2]. In the self-oscillating mode of operation [2, 3] the magnetometer signal is of the form

$$s(t) = A \sin(2\pi f_L t + \phi) + s_0. \quad (5.2)$$

The Larmor frequency, f_L , has to be extracted from the signal. Equation 5.1 connects the frequency determination precision directly to the resulting field measurement precision. The basic demand on the frequency measurement system in order to achieve the required field precision is a resolution of a few hundred μHz in an integration time of 100 s. Moreover, the synchronous detection of signals from an array of magnetometers requires a cost-effective multi-channel solution.

In our recent study [3] of optically-pumped magnetometer performance, frequency measurements were made with a commercial frequency counter (Stanford Research Systems, model SR620), which has a limited frequency resolution, thereby limiting the magnetic field determination. Frequency counters rely on the detection of zero crossings of a periodic signal in a given dwell time. Their performance is limited by their resolution of the zero crossing times, an event which is affected by the amplitude,

offset, and phase noise of the signal. In demanding applications, such as the one investigated here, that timing jitter limits the ultimate frequency resolution of the magnetometer signal measurement. Put simple, the limitation of frequency counters is due to the fact that they use only information in the vicinity of the zero crossings, while valuable waveform information from in between the zero crossings is ignored.

As a more powerful alternative one can use numerical frequency estimation algorithms to extract the frequency from the complete waveform sampled at an appropriate rate and with a sufficient resolution. The performance of an ADC-based measurement system for measuring a single frequency of about 8 Hz was discussed in [4]. Under the assumption that a stable clock triggers the ADC, the authors in [4] show that the lower limit of the frequency resolution of their system coincides with the Cramér–Rao lower bound (CRLB) [5]. The CRLB is a well-known concept from information theory and describes principle limits for the estimation of parameters from sampled signals.

In our application, the Larmor frequency in a magnetic field of $2 \mu\text{T}$ lies in the audio frequency range ($f_L = 7 \text{ kHz}$). We have investigated whether a commercially available (and rather inexpensive) professional multi-channel sound card would present a viable solution for sampling the magnetometer signals. The estimation of the frequency from the sampled data was done by a software algorithm. In the following we will show that such a simple system can indeed be used for CRLB limited real-time frequency measurements and for a detailed study of noise processes which limit the precision of atomic magnetometers.

5.2 The system

The frequency measurement system consists of a professional sound card (M–Audio Delta 1010) for digitizing the analog input data, an atomic clock to provide a stable time reference, and a standard personal computer (PC) which reads the data and runs the frequency estimation algorithm. The sound card provides 8 analog input channels in a breakout box that connects to a PCI interface card in the PC. The analog input signals can be sampled with a

resolution of up to 24 bit at a sampling rate of up to 96 kHz. In order to limit the amount of data we used only 16-bit resolution, which was proven to yield sufficient precision. Jitter or drifts of the sampling rate induce additional phase noise on the sampled signal which can seriously degrade the precision of the frequency estimation. An essential feature of the Delta 1010 sound card is its “world clock” input which can be used to phase-lock the internal clock of the sound card to an external 96 kHz time base. The time base was realized by a frequency generator synchronized to the 10 MHz signal of a rubidium frequency standard (Stanford Research Systems, model PRS10). The Rb frequency standard provides a relative stability of 10^{-12} in 100 s which minimizes possible sampling rate jitter and drifts far below the required level. The requirements for the PC system are not very demanding as long as it allows for the continuous recording of the 16 bit data sampled at a rate of 96 kHz (5.8 GB/h for 8 channels). A 1.8 GHz Pentium-4 processor was fast enough for real-time frequency determination for all eight channels at a given integration time. However, for the detailed analysis described below, in which the integration time is varied, the time series were evaluated off-line from the stored sampled data.

5.3 Performance

Considering the magnetometer signal given by Eq. 5.2, the frequency f_L is to be determined from the AC-coupled signal data which, after sampling, are of the form

$$x_n = A \sin \left[2\pi \sum_{k=1}^n (f_L + \delta f_k) \Delta t + \phi_0 + \delta \phi_n \right] + \delta x_n, \\ n = (0, \dots, N-1), \quad (5.3)$$

where A is the signal amplitude, Δt the time resolution (inverse of the sampling rate r_s), and ϕ_0 the initial phase. The number of sample points is $N = \tau/\Delta t (= \tau r_s)$, where τ is the measurement integration time. Also shown is the noise contribution at each point n arising from phase noise $\delta \phi_n$, frequency noise $\sum_{k=1}^n \delta f_k$, and offset noise δx_n . The frequency is determined from the data x_n by a maximum likelihood estimator based on a numerical Fourier transformation which provides a CRLB limited value [6]. The algorithm iteratively searches for the frequency f that maximizes the modulus of the

noise source	$\sigma_A^2(\tau)$	$\sigma_A(\tau)$
white offset	$\frac{3}{\pi^2 A^2} \cdot \rho_x^2 \cdot \frac{1}{\tau^3}$	$\propto \tau^{-3/2}$
flicker frequency	$2 \ln 2 \cdot h_f^2 \cdot 1$	$\propto \tau^0$
white frequency	$\frac{1}{2} \cdot \rho_f^2 \cdot \frac{1}{\tau}$	$\propto \tau^{-1/2}$
flicker phase	$\frac{3}{4\pi^2} \cdot h_\phi^2 \cdot \frac{\ln(2\pi f_c \tau)}{\tau^2}$	$\propto \tau^{-1}$
white phase	$\frac{3}{8\pi} \cdot \rho_\phi^2 \cdot \frac{f_c}{\tau^2}$	$\propto \tau^{-3/2}$

TABLE 5.1: The central column shows the dependence of the Allan variance σ_A^2 on the integration time τ and measurement bandwidth f_c for the noise sources listed at the left [7]. White noise sources α are characterized by their power spectral density ρ_α^2 . The frequency dependent spectral density of flicker noise process α is modeled by $\rho_\alpha^2(f) = h_\alpha^2/f$. By assuming the relation $f_c = (2\tau)^{-1}$ we find the power laws which typify each noise type, shown in the right hand column.

Fourier sum

$$MF(f) = \left| \sum_{n=0}^{N-1} x_n W_n \exp \left(i \frac{2\pi f}{r_s} n \right) \right|, \quad (5.4)$$

where W_n is a windowing function.

Under ideal conditions (stable field and ideal electronics), the frequency and phase noise (δf_k and $\delta \phi_n$) are not present in the signal (Eq. 5.3). The fundamental noise contribution is the photocurrent shot noise, which is proportional to the square root of the DC offset s_0 in Eq. 5.2. The noise is converted, by a transimpedance amplifier, to voltage V_{pc} and has a Gaussian amplitude distribution with zero mean, corresponding to a white frequency spectrum that is characterized by its power spectral density ρ_x^2 (in V^2/Hz). The signal-to-noise ratio (SNR) is defined as $A^2/(\rho_x^2 f_s)$, where $f_s = (2\Delta t)^{-1} = r_s/2$ is the sampling rate limited bandwidth, i.e., the Nyquist frequency or the highest frequency that can be detected unaliased. The CRLB of the frequency estimation from such an ideal magnetometer signal is given by the variance [5]

$$\sigma_{\text{CRLB}}^2 = \frac{3\rho_x^2}{\pi^2 A^2 \tau^3}. \quad (5.5)$$

In frequency metrology it is customary to represent frequency fluctuations in terms of the Allan

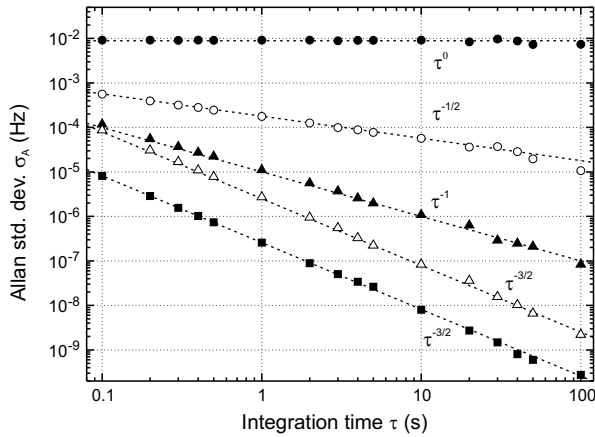


FIGURE 5.1: Allan standard deviation of the frequency of a synthesized sine wave affected by different noise processes. From top to bottom: flicker frequency noise (black dots), white frequency noise (open circles), flicker phase noise (black triangles), white phase noise (open triangles), white offset noise (black squares).

standard deviation σ_A – or its square σ_A^2 , the Allan variance [8, 7]. One can show that for white noise σ_A coincides with the classical standard deviation [9]. A double logarithmic plot of the dependence of σ_A on the integration time τ is a valuable tool for assigning the origin of the noise processes that limit the performance of an oscillator (see for example [8, 7]). As shown in Table 5.1, the variance σ_A^2 depends both on integration time τ and measurement bandwidth f_c , which, for a measurement interval τ , is given by $f_c = (2\tau)^{-1}$. When that relation between bandwidth and integration time is inserted into the formulas given in the central column of Table 5.1 [7], one finds the typical τ dependencies of the Allan standard deviation σ_A shown in the right-hand column. In the presence of several uncorrelated noise processes, α , the variance of the estimated frequency is given by

$$\sigma^2 = \sum_{\alpha} \sigma_{\alpha}^2(f). \quad (5.6)$$

Note that for a magnetometer signal, the contribution from Eq. 5.5 will always be present in the sum.

We first investigated whether our data analysis algorithm reproduces the theoretical τ -dependencies shown in Table 5.1. For that purpose we generated time series (16 bit, 96 kHz) corresponding to Eq. 5.3 with only one of the phase, frequency, or offset noise

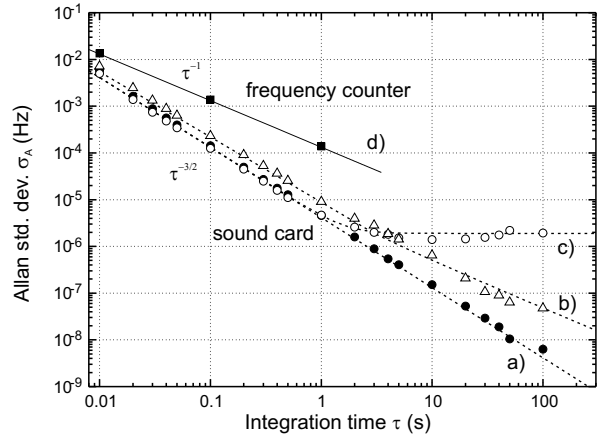


FIGURE 5.2: Allan standard deviation of the frequency of a sine wave affected by different noise processes, measured with the sound card (a–c) and a frequency counter (d): a) white offset noise, b) white offset noise and flicker phase noise, c) white offset noise and flicker frequency noise. The dashed lines represent the dependencies calculated on an absolute scale using the applied noise amplitudes. d) The same signal as in a) measured with a commercial frequency counter (Stanford Research model SR620) with a 300 Hz input bandpass filter.

terms enabled, and selected with well defined spectral characteristics (flicker or white). Figure 5.1 shows the Allan standard deviation σ_A of those synthetic data. The emphasis here lies on the slopes rather than on the absolute values, which were chosen to yield a readable graph.

Next, we investigated the ability of the sound card to reach CRLB limited detection of a 7 kHz sine wave. The wave was generated by a digital function generator (Agilent, model 33220A) stabilized to the same Rb frequency standard as the sound card. In order to simulate a signal comparable to that of the magnetometers, the SNR of the function generator output was artificially decreased from its nominal value of better than 5×10^5 to about 1.3×10^5 (in a 1 Hz bandwidth) by adding white offset noise. We recorded a 1 h time series of that signal, sampled with 16-bit resolution. The data were analyzed with the same algorithm as above and yielded an Allan standard deviation $\sigma_A(\tau)$, shown as black dots in Fig. 5.2a). The measurement agrees on an absolute scale with the CRLB calculated using Eq. 5.5 and the applied SNR. In addition to the offset noise, a second noise

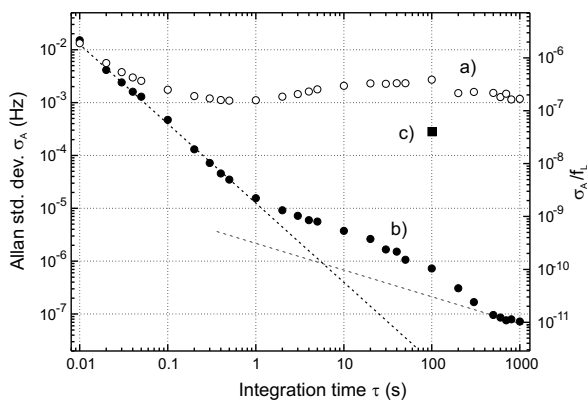


FIGURE 5.3: a) ASD σ_A of magnetic field fluctuations inside a multi-layer magnetic shield. b) Residual fluctuations of the stabilized magnetic field. The dashed lines indicate the CRLB (left) and an assumed white frequency noise limitation (right). c) Stability required for the proposed nEDM experiment.

source was used to apply $1/f$ noise, in turn, to the frequency or to the phase modulation input of the function generator. The resulting σ_A of the measured data is shown in Figs. 5.2b) and c). Figure 5.2d) shows σ_A derived from the same signal as Fig. 5.2a) but analyzed by the commercial frequency counter (Stanford Research Systems, model SR620) that was used in [3]. The three points shown correspond to the three possible integration times of the SR620. It can be clearly seen that the counter technique does not allow the correct measurement of these faint noise processes. However, extrapolation of the data points suggest that for integration times less than 10 ms the CRLB could be reached.

Finally, after the frequency estimator algorithm and the sound card had proven their CRLB performance limit, we used the system to analyze the frequency generated by an optically-pumped magnetometer (OPM). A magnetic field of $2\ \mu\text{T}$ was produced by a solenoid driven by an ultra-stable current source. The OPM signal in that field is a 7 kHz sine wave. The OPM and the solenoid were located in a 6-layer magnetic shield in order to suppress external field fluctuations. Figure 5.3a) shows σ_A of a 2 h time series recorded with the sound card. The data represent pure magnetic field fluctuations. In particular, the approximately 2 mHz fluctuations in the range between 2 to 200 s could be traced back to

irregular current fluctuations in the solenoid. Nevertheless, the relative field stability — and therefore the relative current stability — is on the order of 3×10^{-7} for that range of integration times. However, for a 100 s integration time the field instability exceeds the requirement for the nEDM experiment mentioned in the introduction.

In order to determine the magnetometer performance limit, we actively stabilized the magnetic field in the following way. The magnetometer frequency was compared to a stable reference oscillator (i.e., the Rb frequency standard) by means of a phase comparator, and the error signal was used to control the solenoid current, thus realizing a phase-locked loop. Figure 5.3b) shows the Allan standard deviation of the OPM in the stabilized field, which is CRLB-limited up to an integration time of 1 s. The noise excess between 1 and 300 s above the limits expected from the CRLB and the assumed white noise limitation shows the limitation of the current stabilization scheme, which nonetheless allows the suppression of the fluctuations by three orders of magnitude at the integration time of interest.

We have realized a frequency measurement system based on a digital sound card and have shown that it yields a performance superior to commercial frequency counters. We have proven that the system yields CRLB limited frequency resolution in measurements of sine waves affected by various sources of noise. We have used the system to prove that, at least in a limited range of integration times, an active field stabilization by an optically pumped magnetometer is limited by the theoretical Cramér–Rao bound. The performance and the multi-channel feature of the sound card and its external frequency reference option present a low-cost alternative for applications requiring simultaneous characterization of several frequency generation systems, especially for long integration times.

ACKNOWLEDGMENTS We thank Francis Bourqui for help in developing the read-out software. We acknowledge financial support from Schweizerischer Nationalfonds (grant no. 200020–103864), and Paul Scherrer Institute (PSI).

References

- [1] S. Groeger, G. Bison, and A. Weis. *Design and performance of laser-pumped Cs magnetometers for the planned UCN EDM experiment at PSI*. J. Res. Natl. Inst. Stand. Technol. **110**(3), 179–183 (2005).
- [2] A. L. Bloom. *Principles of operation of the rubidium vapor magnetometer*. Appl. Opt. **1**(1), 61–68 (1962).
- [3] S. Groeger, A. S. Pazgalev, and A. Weis. *Comparison of discharge lamp and laser pumped cesium magnetometers*. Appl. Phys. B **80**(6), 645–654 (2005).
- [4] Y. Chibane, S. K. Lamoreaux, J. M. Pendlebury, and K. F. Smith. *Minimum variance of frequency estimations for sinusoidal signal with low noise*. Meas. Sci. Technol. **6**, 1671–1678 (1995).
- [5] S. M. Kay. *Fundamentals of Statistical Signal Processing, Volume I: Estimation Theory*. Prentice-Hall signal processing series. Prentice Hall PTR Upper Saddle River, New Jersey 07458 (1993).
- [6] D. C. Rife and R. R. Boorstyn. *Single-tone parameter estimation from discrete-time observations*. IEEE Trans. Inf. Theory **20**(5), 591–598 (1974).
- [7] P. Lesage and C. Audoin. *Characterization and measurement of time and frequency stability*. Radio Science **14**(4), 521–539 (1979).
- [8] J.A. Barnes, A. R. Chi, L.S. Cutler, D.J. Healey, D.B. Leeson, T.E. McGunigal, J.A. Mullen, Jr., W.L. Smith, R.L. Sydnor, R.F.C. Vessot, and G.M.R. Winkler. *Characterization of frequency stability*. IEEE Trans. Instrum. Meas. **20**, 105–120 (1971).
- [9] D. W. Allan. *Time and frequency (time-domain) characterization, estimation, and prediction of precision clocks and oscillators*. IEEE Trans. Ultrason. Ferroel. Freq. Contr. **34**(6), 647–654 (1987).

Chapter 6

Laser-pumped optically detected magnetic resonance using linearly polarized light

S. Groeger^{1,2}, G. Bison¹, A. S. Pazgalev^{1,3}, M. Rebetz¹, and A. Weis¹

¹*Département de Physique, Université de Fribourg, Chemin du Musée 3, 1700 Fribourg, Switzerland*

²*Paul Scherrer Institute, 5232 Villigen PSI, Switzerland*

³*Ioffe Physical Technical Institute, Russ. Acad. Sc., St. Petersburg, 194021, Russia*

To be submitted.

ABSTRACT: We describe a novel method of optically detected magnetic resonance in Cs vapor using linearly polarized light. When the light propagation direction is parallel to the magnetic field, a resonance signal can be detected in the transmitted light intensity at the second harmonic of the radio-frequency field. We find that the linewidth of the resonance is twice narrower than the one observed in the same sample using the well-known M_x geometry, which relies on circularly polarized light. This offers an interesting possibility for low field magnetometry.

6.1 Introduction

Optically pumped alkali-vapor magnetometers (OPM) using circularly polarized light are widely used in many applications. One of the most common realizations is the so-called M_x magnetometer [1]. In that technique circularly polarized light is used to create a macroscopic polarization (orientation) in a vapor of alkali atoms at an angle of 45° with respect to the static magnetic field \vec{B}_0 under investigation. A small additional magnetic field $\vec{B}_1(t)$ (hereafter referred to as radio-frequency or r.f. field) oscillating at a frequency close to the Larmor frequency induces coherent sublevel population oscillations in the sample, which lead to a synchronous modulation of the transmitted light intensity. The modulation amplitude shows a resonant behavior when the r.f. frequency coincides with the Larmor frequency. On resonance the intensity modulation is dephased by 90° with respect to the r.f. field. These properties can be used to determine the magnetic field from the modulation frequency. Discharge lamps are commonly used as light sources for alkali OPMs. Spectral lamps emit a broad spectrum and can be used for optical pumping only, when a single fine structure component (typically the D_1 line for alkalis) is isolated by means of an appropriate filter [2].

Pumping with circularly polarized light builds up a vector polarization (orientation) in the medium. It is well known [3] that pumping with linearly polarized light leads to the creation of a tensor polarization (alignment) in the atomic ground state. However, only media with an angular momentum $F \geq 1$ can have a tensor polarization. It is also well known [2] that light interacting with the atoms via an electric dipole transition couples only to the vector and (second order) tensor polarization, so that higher order multipole moments can not be detected (in a simple way) via optical interactions. The ground state of alkali atoms has an angular momentum $J = 1/2$, which can not be aligned. However, the hyperfine interaction with the nuclear spin I splits the ground state into two hyperfine levels with angular momenta $F_\pm = |I \pm 1/2|$, which can be aligned provided $F \geq 1$. That alignment can be detected if the light source has a sufficient spectral resolution to interact only with the aligned hyperfine state. In the same way an alignment can only

be created, when the pumping light can address isolated hyperfine components. In general discharge lamps do not allow to address individual hyperfine lines and hence cannot be used to create (or detect) a ground state alignment. Nonetheless optical pumping with linearly polarized light was observed in Rb using an isotope filtering technique [4, 5]. That technique is however restricted to Rb and cannot be applied to neither Na nor K because of the unresolved hyperfine spectrum in the emission spectrum of the lamp, nor to Cs for which no isotope filters are available.

Due to their very narrow spectral widths (several MHz compared to the Doppler broadening of several hundred MHz), tunable lasers offer the possibility to selectively drive an isolated optical hyperfine transition, which is a very effective way to create an alignment with linearly polarized light. M_x magnetometers using laser pumping with circularly polarized light were demonstrated to yield a superior magnetometric performance compared to lamp pumped devices [6, 7].

The first detection of an optically induced alignment was reported in ^4He [8]. In [4] the authors observed the alignment in a lamp-pumped ^{87}Rb vapor using the same beam for pumping and probing the atoms by analyzing the induced linear birefringence of the vapor. Prior to that experiment the DC component and components oscillating at the fundamental and double resonance frequency of the alignment tensor have been observed in ^{87}Rb via birefringence measurements [5] using a double beam technique. A very extensive discussion of laser pumping with circularly and linearly polarized light in ^4He can be found in [9, 10]. These authors have investigated several magnetometry techniques using both orientation and alignment signals and they observed magnetic resonances by applying a radio-frequency field, light intensity modulation, polarization modulation, or laser frequency modulation. A variant of the latter technique in which a polarizer was inserted for the detection of magneto-optical rotation was realized with ^{87}Rb by [11, 12].

In this work we report on the creation and detection of alignment in Cs vapor by a single linearly polarized laser beam combined with the destruction of the alignment by a resonant r.f. field. In contrast to prior work reported in [5, 4, 9] we detect the signal at the second-harmonic of the applied r.f. field.

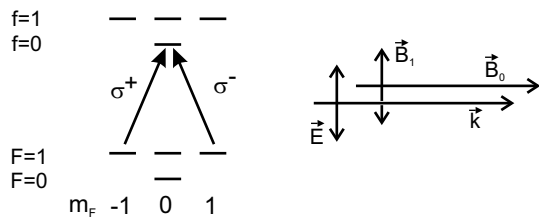


FIGURE 6.1: Left: Spin-1 system as simplification of the Cs level scheme. Right: Experimental geometry: the linearly polarized light propagation direction, \vec{k} , is parallel to the static magnetic field, \vec{B}_0 . The radio-frequency field, \vec{B}_1 , is perpendicular to the static field.

This offers the possibility to detect the alignment at low magnetic fields where the quadratic Zeeman splitting is negligible. This was not possible with the technique reported in [4], where the signals at the first harmonic cancel each other in the low field limit.

6.2 Theory

For a theoretical description we used a density matrix approach to calculate the resonance signals.

Cesium has a nuclear spin $I = 7/2$, which implies that there are 16 Zeeman sublevels in the two hyperfine levels $F = 3, 4$ of the ground state. In order to get a problem, which can be analyzed algebraically, in a way similar to the (vector) orientation based systems, we model the atom as having a nuclear spin $I = 1/2$, as shown in Fig. 6.1. The relevant hyperfine transition in this system is $F = 1 \rightarrow f = 0$. We chose a geometry, in which the light propagation direction, \vec{k} , is along the static magnetic field, \vec{B}_0 (Fig. 6.1). The r.f. field is perpendicular to \vec{B}_0 with an amplitude $2B_1$ and an oscillation frequency ω . The plane of polarization of the light is characterized by the electric field vector, \vec{E} , which is also perpendicular to \vec{B}_0 . As a basis for the polarization states of light we use the orthogonal states of circular (σ_+ , σ_-) and linear ($\sigma_0 = \pi$) polarization. In the most general geometry all of these polarization states contribute to the optical pumping with intensities I_+ , I_- , and I_0 , which are proportional to the squares of the corresponding electric field components. In our case $I_+ = I_- \equiv I_\sigma$ and $I_0 = 0$.

The density matrix, ρ , describing the atomic en-

semble can be decomposed in terms of irreducible spherical tensors $T_q^{(k)}$

$$\rho = \sum_{k=0}^{2F} \sum_{q=-k}^k \rho_q^{(k)} T_q^{(k)}, \quad (6.1)$$

where

$$\rho_q^{(k)} = \langle T_q^{(k)} \rangle \quad (6.2)$$

represent the components (labeled by q) of the state multipoles or multipole moments. $k = 0, 1, 2$ represent the scalar, the vector, and the second-rank tensor, which correspond to the state population, its orientation, and its alignment components respectively. The components $\rho_q^{(k)}$ represent coherent superpositions of levels with magnetic quantum numbers differing by $\Delta M = q$ and are therefore also referred to as $\Delta M = q$ coherences. In a transverse magnetic field B , the multipole components $\rho_q^{(k)}$ precess at the frequencies $q\omega_L$ around the magnetic field direction. The frequency $\omega_L = \gamma_F B$ is the Larmor frequency in the low field limit (linear Zeeman splitting) and γ_F is the gyromagnetic ratio, which is approximately $\gamma_F/2\pi \approx 3.5 \text{ Hz/nT}$ for cesium. When coherently driven by the r.f. field the precessing multipoles modulate the (complex) index of refraction of the medium, and hence its absorption coefficient in a synchronous manner. The precessing multipole moments $\rho_{\pm 2}^{(2)}$ thus yield a modulation of the transmitted intensity at the second harmonic of the Larmor frequency.

One can show that $\rho_{2\omega} = \rho_2^{(2)}$, i.e., the amplitude of ρ oscillating at the frequency 2ω , is proportional to I_σ . In the limit where both the pumping light intensity (expressed as pumping rate $\gamma_p \propto I_\sigma$) and the Rabi-frequency of the applied r.f. field, $\Omega = \gamma_F B_1$, are small compared to the relaxation rate, the second harmonic alignment signal ($\Delta M = 2$ coherence) is given by

$$\rho_{2\omega} \propto \frac{\gamma_p \Omega^2}{(\gamma^{(1)} + i\delta)(\gamma^{(2)} + 2i\delta)} e^{2i\omega t}, \quad (6.3)$$

where we used the rotating-wave approximation. The parameters $\gamma^{(1)}$ and $\gamma^{(2)}$ represent the relaxation rates of the orientation ($\rho^{(1)}$) and of the alignment ($\rho^{(2)}$), respectively, and $\delta = \omega - \omega_L$ is the detuning of the r.f. frequency with respect to the Larmor frequency. It is worthwhile to note that $\gamma^{(1)}$ is the linewidth observed in the M_x magnetometer signal. We have made the assumption that the longitudinal and transversal relaxation rates for

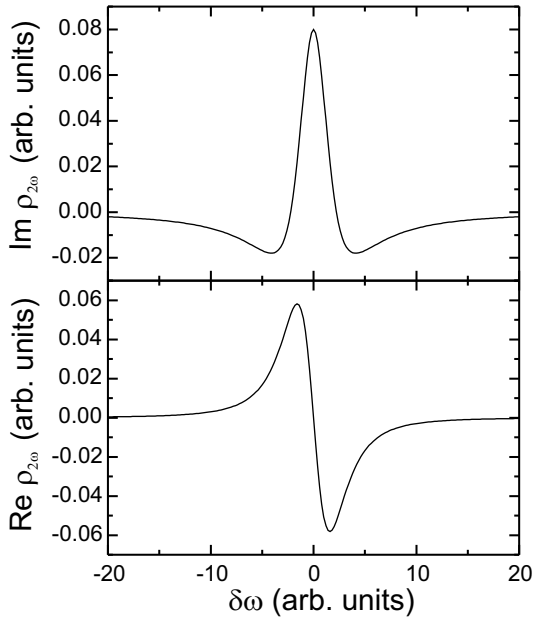


FIGURE 6.2: Theoretical lineshapes of the magnetic resonance signal oscillating at the second harmonic of the r.f. frequency as a function of the r.f. detuning $\delta\omega$ for $\gamma^{(1)} = \gamma^{(2)}$. We define the frequency span between the extrema of the imaginary part as the full linewidth.

each specific multipole moment are the same, i.e., that the relaxation rates depend on k , but not on q . The real and imaginary part in Eq. 6.3 yield the in-phase and quadrature signals of the the experimental phase sensitive detection. The detected signal is proportional to $\gamma_p \rho_{2\omega}$. In Fig. 6.2 the lineshapes corresponding to the real and the imaginary part of Eq. 6.3 is shown.

If we assume that the alignment relaxes at the same rate as the orientation, i.e., $\gamma^{(2)} = \gamma^{(1)} \equiv \gamma$, the frequency difference between the two extrema of the dispersively shaped real part of $\rho_{2\omega}$ is given by 0.768γ , while the width of the corresponding resonance in the M_x magnetometer is 2γ . One therefore expects a 2.6 times narrower width with the linearly polarized arrangement.

This fact can be intuitively understood in the following way. In order to alter the $\Delta M = 2$ coherence two r.f. photons have to be absorbed. As a consequence a detuning by $\delta\omega$ from the one-photon resonance corresponds to a detuning of $2\delta\omega$ from the the $\Delta M = 2$ resonance, which explains why the resonance of the alignment signal is twice as narrow. A

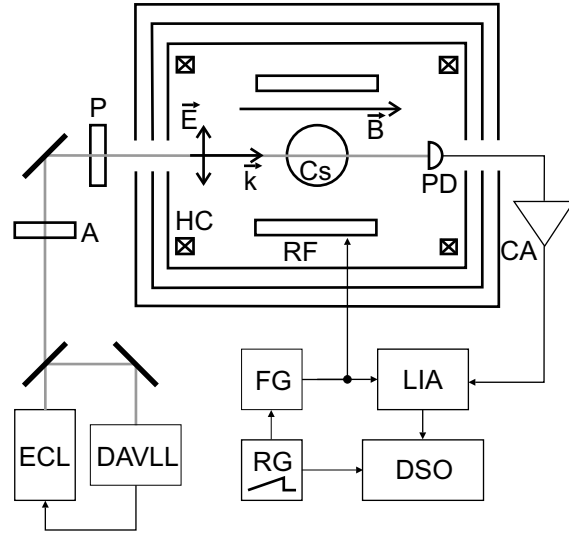


FIGURE 6.3: Experimental setup: Inside the three-layer Mumetal shield: Cs: paraffin coated Cs cell, HC: Helmholtz coils producing the longitudinal magnetic field, RF: radio-frequency coils, PD: non-magnetic photodiode. Outside the shield: ECL: extended cavity diode laser, DAVLL: laser frequency stabilization, A: optical attenuator, P: linear polarizer, CA: current amplifier, FG: function generator, RG: ramp generator, LIA: lock-in amplifier, DSO: digital storage oscilloscope.

correction to this simple argument comes from the fact that the lineshape (Eq. 6.3) of the alignment resonance differs from the dispersive Lorentzian observed with the M_x geometry.

6.3 Experiment

The cesium vapor was contained in an evacuated cylindrical glass cell (20 mm diameter, 20 mm length, purchased from MAGTECH Ltd., St. Petersburg, Russia). The inner walls of the cell have a paraffin coating in order to prevent the atoms being depolarized due to wall collisions. In an preliminary experiment we have determined the intrinsic linewidth $\Delta\nu_1$ of the cell in the M_x geometry. The measurement was done by extrapolating the measured linewidths (inferred from fits to the observed resonances) to zero r.f. power and zero light power. We found an intrinsic linewidth of $\Delta\nu_1 = 4.7(4)$ Hz (at about 21°C) for the cell volume of about 6.5 cm^3 .

The experimental setup using an extended cavity stabilized diode laser (Sacher Lasertechnik

TEC500) is shown in Fig. 6.3. The laser frequency is stabilized to the $6S_{1/2}, F = 4 \rightarrow 6P_{1/2}, f = 3$ hyperfine component by means of a dichroic atomic vapor laser lock (DAVLL) [13]. The power of the light beam can be adjusted by a variable neutral-density filter. The light beam passes through a linear polarizer and irradiates the Cs cell, which is located inside a three-layer Mumetal shield. A pair of Helmholtz coils produce a magnetic field of about $2 \mu\text{T}$ parallel to the light propagation direction inside the shield. The light intensity transmitted through the cell is detected by a non-magnetic photodiode (HAMAMATSU S6801-01). The photodiode signal is amplified by a low-noise transimpedance amplifier (FEMTO DLPCA-200) and analyzed by a lock-in amplifier (Stanford Research SR830) tuned to the second harmonic of the r.f. frequency. A function generator, which serves also as reference for the lock-in amplifier, provides the r.f. signal at a frequency ω via the Helmholtz-like r.f. coils surrounding the cell. Magnetic resonance spectra were recorded by sweeping the r.f. frequency with a ramp generator. The in-phase and quadrature signals of the lock-in amplifier were recorded by a digital storage oscilloscope. Typical in-phase and quadrature spectra, recorded in a single scan with a lock-in time constant of 10 ms, are shown in Fig. 6.4. The dispersive shape of the quadrature signal with a zero crossing on resonance can be used in magnetometry applications.

The linewidth of the $\Delta M = 2$ coherence can be determined from a fit using the lineshape given by Eq. 6.3. Similar to the measurements with the M_x geometry, the intrinsic linewidth of the $\Delta M = 2$ coherence, $\Delta\nu_2$, was inferred by extrapolating a series of measured resonance linewidths to zero r.f. power and zero light power. We found $\Delta\nu_2 = 2.4(2) \text{ Hz}$, which is a factor two narrower than $\Delta\nu_1$. Using Eq. 6.3 we find $\gamma^{(2)}/\gamma^{(1)} \approx 1.6$.

6.4 Conclusion

Optical pumping with linearly polarized light and the light propagation direction parallel to a static magnetic field can be used to detect at the second harmonic of the r.f. field a well-resolved magnetic resonance line with an M-shaped profile of the in-phase component and a dispersive quadrature component. The observed signal is narrower than the signal measured in the standard M_x geometry. In

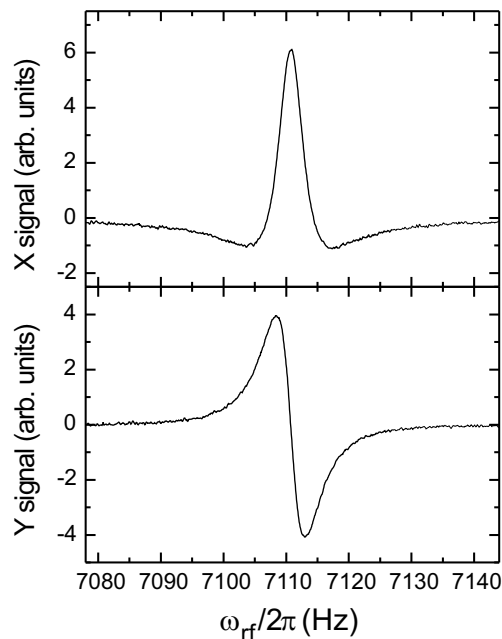


FIGURE 6.4: Experimental resonance signal in a single-shot measurement with a lock-in time constant 10 ms, and a sweep speed of approximately 1 Hz per second.

order to get a better understanding of the underlying processes a more detailed theoretical and experimental study is underway. The use of the same light beam for optical pumping and for detecting the alignment signal is particularly convenient in view of device design. In particular the possibility to use light propagating along the magnetic field to be measured will allow very compact designs for multi-sensor (gradiometer) applications. Another, not yet investigated benefit of this novel technique, lies in the fact that the detection at 2ω yields a lower noise in low-frequency (few kHz) applications, where flicker ($1/f$) noise predominates. This feature, together with the narrower linewidth, lets us expect that the linearly polarized magnetometer described here will have a higher magnetometric sensitivity than the standard M_x magnetometer.

ACKNOWLEDGMENTS We thank the Swiss National Science Foundation (grant no. 200020-103864, 205321-105597) for financial support. One of the authors (A.S.P.) acknowledges financial support from the Research foundation of the University Fribourg.

References

- [1] A. L. Bloom. *Principles of operation of the rubidium vapor magnetometer*. Appl. Opt. **1**(1), 61–68 (1962).
- [2] W. Happer. *Optical pumping*. Rev. Mod. Phys. **44**(2), 169–249 (1972).
- [3] D. Budker, W. Gawlik, D. F. Kimball, S. M. Rochester, V. V. Yashchuk, and A. Weis. *Resonant nonlinear magneto-optical effects in atoms*. Rev. Mod. Phys. **74**(4), 1153–1201 (2002).
- [4] E. B. Aleksandrov and M. V. Balabas. *Optical alignment of ^{87}Rb atoms*. Opt. Spectrosc. **69**(1), 4–6 (1990).
- [5] B. S. Mathur, H. Y. Tang, and W. Happer. *Light propagation in optically pumped alkali vapors*. Phys. Rev. A **2**(3), 648–660 (1970).
- [6] E. B. Aleksandrov, M. V. Balabas, A. K. Ver-shovskii, A. E. Ivanov, N. N. Yakobson, V. L. Velichanskii, and N. V. Senkov. *Laser pumping in the scheme of an Mx -magnetometer*. Opt. Spectrosc. **78**(2), 325–332 (1995).
- [7] S. Groeger, A. S. Pazgalev, and A. Weis. *Comparison of discharge lamp and laser pumped cesium magnetometers*. Appl. Phys. B **80**(6), 645–654 (2005).
- [8] W. E. Bell and A. L. Bloom. *Observation of forbidden resonances in optically driven spin systems*. Phys. Rev. Lett. **6**(11), 623–624 (1961).
- [9] H. Gilles, B. Cheron, and J. Hamel. *Magné-tomètre à ^4He pompé par laser. Isotropie spatiale des signaux de résonance en résonance magnétique et en modulation de lumière*. J. Phys. II France **2**(4), 781–799 (1992).
- [10] H. Gilles, J. Hamel, and B. Cheron. *Laser pumped He-4 magnetometer*. Rev. Sci. Instr. **72**(5), 2253–2260 (2001).
- [11] D. Budker, D. F. Kimball, S. M. Rochester, V. V. Yashchuk, and M. Zolotarev. *Sensitive magnetometry based on nonlinear magneto-optical rotation*. Phys. Rev. A **62**, 043403 (2000).
- [12] D. Budker, D. F. Kimball, V. V. Yashchuk, and M. Zolotarev. *Nonlinear magneto-optical rotation with frequency-modulated light*. Phys. Rev. A **65**, 055403 (2002).
- [13] V. V. Yashchuk, D. Budker, and J. R. Davis. *Laser frequency stabilization using linear magneto-optics*. Rev. Sci. Instrum. **71**(2), 341–346 (2000).

Outlook

In this thesis we have described the development of laser-pumped Cs magnetometers (Cs-LsOPM) in the M_x geometry which will be used in the nEDM experiment at PSI. The steady improvement of the individual components and the study and suppression of performance spoiling systematic effects have yielded an intrinsic sensitivity on the order of $14\text{fT}/\sqrt{\text{Hz}}$, which is superior to the performance of the conventional state-of-the-art lamp-pumped variant (LpOPM) of the magnetometer. This is an important result as it helps to answer – from a scientific point of view – the question about the adequate choice of the optical pumping source in the case of Cs. Moreover, the laser as a single light source in combination with the possibility of using single fibers rather than fiber-bundles (as in the case of LpOPMs) provides an enormous advantage from the point of view of system design, especially if one considers a multi-sensor array.

The stable and reliable operation of an 8-sensor Cs-LsOPM array inside the shield of the RAL-Sussex experiment at ILL has been demonstrated. A major point for the successful operation of that setup was the development of an original frequency measurement system based on a multi-channel sound card. That system has proven to be superior to high-end commercial frequency measurement devices as it allows a Cramér-Rao-limited measurement which represents the ultimate achievable performance. Moreover, the system is easily scalable to a larger array size.

After the study and characterization of the LsOPM and a principle measurement system there remains of course the need for further development work in the frame of the PSI-EDM experiment.

Comparison of Cs-LsOPM array and Hg co-magnetometer In the near future the joint operation of a suitable Cs-LsOPM array and the Hg co-magnetometer inside the existing RAL-Sussex EDM experiment is expected to provide evidence for the superior measurement performance of the Cs system due to the substantially larger amount of information. For such an experiment the LsOPM sensor heads have to be operated in vacuum which demands the development of a compact and reliable vacuum optical feed-through system.

Magnetometry in the presence of strong electric fields Depending on the final design of the EDM experiment LsOPMs will be in an electric field on the order of 10 kV/cm and the influence of that field on the magnetometer performance has to be investigated. On one hand, this requires a sensor array that does not cause sparks and discharges when mounted close to the high voltage electrodes. On the other hand, the electric field may cause a shift of the optical transition due to the Stark effect, which then can appear as an electric-field dependent shift of the magnetometer signal. Such a possible systematic effect has to be studied and – if necessary – to be suppressed. One solution could be the shielding of the Cs by means of a thin (transparent) metallic layer on the Cs cell or a suitable thin Al-shield around the whole sensor head.

Measurement of the magnetic field components and active field stabilization Based on the existing sensor technique the development of a vector magnetometer, measuring all three spatial field components rather than the modulus of the field, can lead to a significantly higher information content of the signals and hence of the distribution of the field and its gradients. This may yield a reduction of the number of the sensors needed. The LsOPM, as it is currently operated, measures the modulus $|\vec{B}|$ of the magnetic field, whose main component is along the z -axis

$$B = \sqrt{B_x^2 + B_y^2 + B_z^2} \approx B_z \left(1 + \frac{B_x^2 + B_y^2}{2B_z^2}\right). \quad (6.4)$$

$|\vec{B}|$ depends quadratically on the transverse field component B_x and B_y . If these components are modulated by means of additional (local) coils at frequencies $\omega_x, \omega_y \ll \omega_{\text{BW}}$ (ω_{BW} is the magnetometer

bandwidth) and with small amplitudes β_x, β_y , Eq. 6.4 will yield signal components with amplitudes $B_x\beta_x/B_z$ and $B_y\beta_y/B_z$ oscillating at the frequencies ω_x and ω_y , respectively, which will allow to infer B_x and B_y by phase-sensitive detection. If the system is fast enough, external compensation coils could then be used to stabilize and minimize the transverse field components as well as the longitudinal component B_z .

Magnetometry with linearly polarized light The demonstration of the superior performance of laser-pumping with circularly polarized light is a strong argument for the investigation and the development of alternative magnetometry techniques, as for example the use of linearly polarized light, which requires a laser as pumping source and does not work with lamp pumping. The variant demonstrated for the first time in this work seems to be very promising and a detailed study shall show its applicability for the nEDM project as well as for other areas of magnetometry. Similarly to the characterization of the conventional LsOPM, the linearly-pumped magnetometer (LPM) has to be investigated with respect to the power dependencies of the signal amplitude, linewidth, noise, and light shift. Due to the fact that linearly polarized light can be decomposed into left- and right-circularly polarized components with equal amplitudes there should be no residual AC-Stark shift. Finally, the parameters of the LPM have to be optimized in order to obtain a maximum intrinsic magnetometric sensitivity.

Danksagung

An dieser Stelle möchte ich all denen danken, die zum Gelingen dieser Arbeit beigetragen haben.

An erster Stelle gebührt mein Dank Herrn Prof. Antoine Weis. In seiner Forschungsgruppe habe ich die Möglichkeit gefunden, mich einem bis dahin für mich komplett neuen Arbeitsgebiet zuzuwenden. Dabei habe ich von Anfang an von Tuns stets die Förderung als auch die nötige Freiheit und das damit verbundene Vertrauen erhalten, die erforderlich sind, um kreativ und produktiv arbeiten zu können. In den zahlreichen Diskussionen und durch seine vielseitigen Anregungen hat er es stets verstanden, die Qualität (und so manches Mal auch die Quantität) meiner Projekte zu fördern und voranzutreiben. Tuns Begeisterung für die Physik und sein Anspruch, die Dinge mit dem erforderlichen Maß an Perfektion durchzuführen, habe ich als sehr inspirierend empfunden. Nicht zuletzt danke ich ihm auch für die zahlreichen Konferenzbesuche, die er mir ermöglicht hat.

Prof. Jean-Claude Dousse danke ich für die angenehme Zusammenarbeit im Rahmen des Vorgerückten Praktikums und dafür, dass er die Bewertung dieser Arbeit übernommen hat.

Manfred Daums Vermittlung und Mithilfe habe ich es mitunter zu verdanken, dass ich die Doktorentsstelle in Fribourg finden konnte. Ihm danke ich für seine stets freundliche und hilfsbereite Art der Zusammenarbeit. Ich freue mich ganz besonders, dass er gerne die Begutachtung dieser Arbeit übernommen hat.

Robert Wynands, der leider nicht allzu lange in unserer Gruppe verbrachte, danke ich für die vielen wertvollen Diskussionen innerhalb sowie außerhalb des Labors, in denen er es oft verstand, die nötigen neuen Impulse und Anregungen zu geben.

I am very grateful to Paul Knowles, who I appreciate very much from both personal and professional point of view, for all his help. Moreover, working together with him in Fribourg and especially in Grenoble was really fun.

I would like to thank Anatoly Pazgalev for teaching me magnetic resonance right at the beginning of my thesis and for the very fruitful collaboration during the time he spent in our group.

Ich danke Georg Bison für die gute Zusammenarbeit und die etlichen Diskussionen, in denen sein großes physikalisches wie technisches Verständnis mir oftmals eine gute Hilfestellung waren. Für seine weitere Arbeit und sein Bestreben bezüglich der Kardiomagnetometrie wünsche ich ihm viel Erfolg.

I thank Simone Ulzega not only for being a colleague but mainly for being just a friend. I appreciate our numerous discussions we had about physics as well as about those things which are sometimes even better. I wish him good luck for his thesis and all further challenges.

Adrian Hofer und Peter Moroshkin sowie Hervé Saudan danke ich für das kollegiale und angenehme Verhältnis und die gute Zusammenarbeit. Adrian danke ich ganz besonders auch wegen seiner freundschaftlichen und hilfsbereiten Art (nicht nur, wenn es um meinen Heimweg ging) und ich wünsche ihm ebenfalls viel Erfolg für seine weitere Arbeit.

Die Zusammenarbeit mit Martin Rebetez habe ich immer als sehr angenehm empfunden, nicht nur wegen seiner Zuverlässigkeit sondern vor allem auch wegen seiner freundlichen und ruhigen Art. Ich danke ihm für seine tatkräftige Mithilfe vor und während der Messungen in Grenoble und wünsche ihm viel Glück und Erfolg für seine Masterarbeit und seinen Werdegang darüberhinaus.

Allen ehemaligen Kollegen, hierbei im besonderen Daniel Nettels und Reinhard Müller-Siebert möchte ich für die gute und kollegiale Zusammenarbeit danken. Ebenso gilt mein Dank Stephan Tandler, Mondher Gantri und José Lamas-Valverde.

Allen Mitarbeitern der PSI-UCN/EDM-Gruppe sowie der EDM-Kollaboration danke ich für die angenehme und erfolgreiche Zusammenarbeit.

Für das kritische Lesen des Manuskripts und die damit verbundenen vielen Verbesserungsvorschläge möchte ich Tun, Paul und Georg danken.

Neben dem Bemühen und den Anstrengungen des Physikers hängt das Gelingen einer experimentellen Arbeit wie der hier vorliegenden natürlich in ganz beträchtlichem Maße von der zur Verfügung stehenden „Hardware“ ab. Daher liegt es mir ganz besonders am Herzen, mich bei den Mitgliedern der Werkstatt – Elmar Moser, Oswald Raetzo, Roland Schmid, Roger Vonlanthen und Cédric Mora – sowie der Elektronikwerkstatt – Jean-Luc Schenker, Olivier Huot und Francis Bourqui – zu bedanken. Über die gesamte Zeit meiner Arbeit hinweg standen sie mir mit Rat und Tat zur Seite und ich konnte immer auf ihre Kreativität, Zuverlässigkeit, Präzision und Flexibilität zählen.

Mein Dank gilt auch den Sekretärinnen Elisabeth Francois, Eliane Esseiva, Marie-Louise Raemy, Bernadette Kuhn-Piccand, Aude Ferrari und Carine Jungo. Speziell bei den zahlreichen Gelegenheiten, in denen es galt, sich auftuende administrative Hürden zu überwinden, konnte ich stets auf Elisabeths und Elianes Hilfsbereitschaft zählen, der ich hiermit noch einmal ganz besonders danken möchte.

Diese Arbeit wurde durch die finanzielle Unterstützung des Schweizerischen Nationalfonds (Nr. 200020–103864) sowie des Paul Scherrer Instituts ermöglicht.

Meinen Eltern möchte ich für ihre stete Unterstützung – sowohl in seelischer als auch finanzieller Hinsicht – meinen tiefen Dank aussprechen.

Meiner Frau Claudia danke ich aus tiefstem Herzen für ihre Liebe und ihre seelische Unterstützung, gerade auch bezüglich meiner Entscheidung für Fribourg und in den dreieinhalb Jahren, in denen sie das dauernde Pendeln zwischen Eching und Fribourg ertragen hat.

Curriculum vitae

Stephan Wilhelm Gröger

Route de l'Aurore 14
1700 Fribourg
Switzerland
Tel.: +41 (0)26 465 1859

Theresienstr. 17a
85386 Eching
Germany
Tel.: +49 (0)89 318 12 999

E-Mail: stephan.groeger@gmx.net



Personal details

Date of birth	November 22, 1975
Place of birth	Munich, Germany
Nationality	German
Status	Married

Education

1986 – 1995	High school (Dom-Gymnasium Freising, Germany)
1995	High school degree (Abitur)
1995 – 2001	Studies in Physics at Technische Universität München (TUM), Germany. Special courses: low temperature physics and superconductivity, applied nuclear physics, medical radiation physics.
July 2000 – Aug. 2000 Oct. 2001 – Jan. 2002,	Working student (“Studentische Hilfskraft”) at TUM: characterization of a beryllium sputter device and production of beryllium coatings on various substrates.
Nov. 2000 – Nov. 2001	Diploma thesis in the research group of Prof. Dr. S. Paul: “ <i>Untersuchungen zu festem Deuterium als Konvertermaterial für ultrakalte Neutronen</i> ”.
Nov. 2001	Diplom in Allgemeiner Physik, Technische Universität München.
since Mar. 2002	Graduate student in the research group of Prof. Dr. A. Weis, Physics Department, University of Fribourg, Switzerland.
May 2003 – June 2003	Graduate course (3ème cycle): “ <i>Atomic physics tests of the Standard Model</i> ”, by Prof. Dr. A. Weis.

Articles

1. W. Schott, J. M. Pendlebury, I. Altarev, S. Groeger, E. Gutsmedl, F. J. Hartmann, S. Paul, G. Petzoldt, P. Schmidt-Wellenburg, and U. Trinks. *UCN production in superfluid helium*. Eur. Phys. J. A **16**, 599–601 (2003).
2. E. Aleksandrov et al. *Search for a Neutron Electric Dipole Moment: Progress Report*. PSI – Scientific Annual Report 2002, Vol. 1, R-00-05, p.25 (2003).
3. E. Aleksandrov et al. *The Magnetic Test Experiment for the Neutron EDM Measurement*. PSI – Scientific Annual Report 2002, Vol. 1, R-00-05.1, p.26 (2003).
4. S. Gröger, G. Bison, R. Wynands, and Antoine Weis. *An Alternative, Laser-Pumped Magnetometer for the Proposed Neutron EDM Experiment*. PSI – Scientific Annual Report 2002, Vol. 1, R-00-05.2, p.27 (2003).
5. E. Aleksandrov et al. *Magnetic Field Stabilization by a Helmholtz-like Coil Configuration*. PSI – Scientific Annual Report 2003, Vol. 1, R-00-05.2, p.136 (2004).
6. S. Groeger, J.-L. Schenker, P. E. Knowles, A. S. Pazgalev, and A. Weis. *A laser pumped cesium magnetometer for neutron-EDM experiments*. PSI – Scientific Annual Report 2004, Vol. 1, R-05-03.CS, p. 150 (2005).
7. S. Groeger, J.-L. Schenker, P. E. Knowles, A. S. Pazgalev, and A. Weis. *Comparison of discharge lamp and laser pumped cesium magnetometers and active magnetic field stabilization*. PSI – Scientific Annual Report 2004, Vol. 1, R-05-03.LL, p. 151 (2005).
8. S. Groeger, A. S. Pazgalev, and A. Weis. *Comparison of discharge lamp and laser pumped cesium magnetometers*. Appl. Phys. B **80**, 645–654 (2005). DOI: 10.1007/s00340-005-1773-x.
9. A. Weis, G. Bison, S. Groeger, and R. Wynands. *Laser magnetometry in fundamental science and in biomagnetic applications* (13th International School on Quantum Electronics: Laser physics and applications, Bourgas, Bulgaria, Sept. 2004). Proc. of SPIE **5830**, 143–149 (2004). DOI: 10.1117/12.617407.
10. S. Groeger, G. Bison, and A. Weis. *Design and performance of laser-pumped Cs magnetometers for the planned UCN EDM experiment at PSI*. J. Res. Natl. Inst. Stand. Technol. **110**(3), 179–183 (2005).
11. S. Groeger, G. Bison, P.E. Knowles, R. Wynands, and A. Weis. *Laser-pumped cesium magnetometers for high resolution medical and fundamental research*. To be published in Sensors and Actuators A:Physical.
12. S. Groeger, G. Bison, P.E. Knowles, and A. Weis. *A sound card based multi-channel frequency measurement system*. Submitted to Eur. Phys. J. AP (arXiv:physics/0506068).
13. S. Groeger, G. Bison, J.-L. Schenker, R. Wynands, and A. Weis. *A high-sensitivity laser-pumped M_x magnetometer*. Submitted to Eur. Phys. J. D (arXiv:physics/0406105).
14. S. Groeger, G. Bison, A. S. Pazgalev, M. Rebetez, and A. Weis. *Laser-pumped optically detected magnetic resonance using linearly polarized light*. To be submitted.

Patent applications

1. S. Gröger, A. S. Pazgalev, G. Bison, and A. Weis. *Optically-pumped magnetometer*, Europäische Patentanmeldung, Nr. 05 405 486.1 (August 19, 2005).

Conferences

1. S. Gröger, R. Wynands, and A. Weis, *Development and performance of a laser driven cesium magnetometer with fT sensitivity*, Spring Meeting of the German Physical Society (DPG), Hannover, March 2003.
2. S. Gröger, G. Bison, A. S. Pazgalev, and A. Weis, *A laser-pumped magnetometer for the planned PSI-n-EDM experiment*, Annual Meeting of the Swiss Physical Society (SPG/SSP), Neuchâtel, March 2004.
3. S. Gröger, A.S. Pazgalev, and A. Weis, *Performance and comparison of optically-pumped cesium magnetometers with fT sensitivity*, Spring Meeting of the German Physical Society (DPG), Munich, March 2004.
4. S. Groeger, G. Bison, and A. Weis, *Design and performance of laser-pumped Cs-magnetometers for the planned UCN edm experiment at PSI*, Conference on Precision Measurements with Slow Neutrons (PMSN), National Institute of Standards and Technology, Gaithersburg MD, U.S.A., April 2004.
5. S. Groeger, G. Bison, P. E. Knowles, R. Wynands, and A. Weis, *Laser-pumped cesium magnetometers for high resolution medical and fundamental research*, European Magnetic Sensors and Actuators Conference (EMSA), Cardiff, Wales, July 2004.
6. S. Groeger, G. Bison, P. E. Knowles, A. S. Pazgalev, and A. Weis, *Cesium magnetometers for a neutron-EDM experiment*, 35th Winter Colloquium on The Physics of Quantum electronics (PQE), Snowbird UT, U.S.A., January 2005.
7. S. Groeger, G. Bison, and A. Weis, *An improved laser pumped cesium magnetometer using hyperfine repumping*, Conference on Lasers and Electro-Optics/Europe – European Quantum Electronics Conference (CLEO/Europe – EQEC 2005), Munich, June 2005.
8. P. E. Knowles, G. Bison, S. Groeger, A. S. Pazgalev, M. Rebetez, and A. Weis, *An array of laser-pumped cesium magnetometers for magnetic field control in a nEDM experiment*, 17th International Conference on Laser Spectroscopy (ICOLS), Cairngorms National Park, Scotland, June 2005.
9. G. Bison, S. Groeger, A. S. Pazgalev, and A. Weis, *Optical magnetometry using a DFB laser at the Cs D_1 transition*, 17th International Conference on Laser Spectroscopy (ICOLS), Cairngorms National Park, Scotland, June 2005.
10. P. Knowles, G. Bison, S. Groeger, A.S. Pazgalev, M. Rebetez, and A. Weis, *Magnetic Field Control for a Neutron EDM Experiment*, Annual Meeting of the Swiss Physical Society (SPG/SSP), Bern, July 2005.

Talks

1. S. Gröger, G. Bison, and A. Weis, *A laser-pumped optical magnetometer for a new n-EDM experiment*, Scientific workshop - Observatoire Cantonal de Neuchâtel, June 28, 2003.
2. S. Gröger, G. Bison, and A. Weis, *A laser-pumped magnetometer for the PSI-n-EDM experiment*, University of Fribourg - Department Day, December 12, 2003.
3. S. Gröger, *Magnetfeldmessung mit höchster Präzision - Cäsiumatome als Magnetfeldsensoren für die Grundlagenforschung und Medizin*, Vortrag im Rahmen einer Informationsreihe für die gymnasiale Oberstufe, Franz-Marc-Gymnasium Markt Schwaben, January 28, 2005.
4. S. Groeger, P.E. Knowles, and A. Weis, *Cesium magnetometers for the nEDM experiment*, Technical Review Meeting - PSI, February 9, 2005.

Ich versichere, dass ich diese Arbeit selbstständig und ohne unerlaubte Hilfe verfasst und keine anderen als die angegebenen Quellen und Hilfsmittel benutzt sowie Zitate kenntlich gemacht habe.

Freiburg, 7. Juli 2005

A handwritten signature in black ink, reading "Stephan Gröger". The signature is written in a cursive style with a large initial 'S' and a long, sweeping underline.

Stephan Gröger